UNIVERSITAT POLITÈCNICA DE CATALUNYA
BARCELONATECH
Departament d'Enginyeria Electrònica

Wireless Power Transfer: Fueling the dots

Dissertation presented in partial fulfillment
of the requierements for the degree of

PhD in Electronic Engineering

Defended by
Elisenda Bou-Balust

Thesis Advisor: Dr. Eduard Alarcon-Cot

June 2017

Electronic Engineering Department

Abstract

Resonant Inductive Coupling Wireless Power Transfer (RIC-WPT) has been proven to provide very high power transfer efficiencies (above 80%) for moderate distances, and is hence foreseen as a key technology to enable wireless power transfer to a myriad of different devices and related applications. Due to the multidisciplinary nature of the WPT underlying principles, several approaches have been provided to analyze RIC-WPT systems from different perspectives (encompassing Electromagnetic fields, Circuit models and Optics), but they have failed to provide a unified model to understand and ultimately to design the behaviour of such systems. This thesis is therefore aimed to, first, provide a multi-modal RIC-WPT complete model oriented to the design and in turn optimisation of RIC-WPT systems and, secondly, to explore and characterize the fundamental challenges precluding the widespread deployment of RIC-WPT and thereby accordingly to yield a set of design guidelines to overcome them. Finally, and due to the fact that multi-node RIC-WPT systems are key to the adoption of this technology, this thesis models, characterizes and analyzes Multiple-Input Multiple-Output RIC WPT Systems, making special emphasis on their scalability.

A la meva mare, que m'ha ensenyat a viure.
A la meva familia, i als que ho són també sense ser-ho.

Acknowledgments

A la meva mare, que és meravella. A la meva familia, que sempre ha estat ajudant i cuidant: a l'Aureli i al Joan Anton, que han estat al costat quan més els necessitava. Només nosaltres sabrem el que ens ha costat arribar fins aqui, i el que ens ha passat pel camí.
I al pare, la Bego i l'Edgar, per tantes estones bones junts. També voldria donar les grácies als meus companys de doctorat -Sergi i Mario- per totes els moments bonissims, els temps-de-cafè i per acompanyar-me en aquest trajecte. Al meu director de tèsis, a l'Eduard, per estar al costat tot aquest temps i haver-me ensenyat tantes coses. I finalment, als meus amics -Irene, Jorge, JC- que m'han recolzat, m'han ajudat i sempre m'han arrancat un somriure quan més ho necessitava.

Gràcies a tots.

"¿Sabe francés
restar,
multiplicar?
Declina maravillosamente!
¡Que decline!
Pero oiga,
¿acaso usted podría cantar a dúo,
con los edificios?
¿Usted acaso comprende
el idioma de los tranvías?"
V.Mayakovsky

Contents

Chapter 1

Introduction

Contents

This chapter exposes the thesis focus and describes the challenges underlying resonant inductive wireless power transfer. The proposed research is described in terms of innovation and its applicability to different environments.

1.1 Overview

Recent research in wireless power transfer (WPT) using resonant inductive coupling has demonstrated very promising efficiencies (above 80%) [1] at large distances compared to the antenna dimensions (more than three times the transmitter/receiver diameters). Due to the number of applications that could benefit from such performance, namely from electric vehicles to sensor networks, commercial electronic devices, health equipment, biomedical implants, fractionated spacecraft and a long etcetera, the development and optimization of this technology is of great interest. Since resonant inductive coupling (RIC) is still a very novel technology interplaying various physical domains and disciplines, different models should be proposed to analyze and predict the behavior of these systems and to increase the overall efficiencies and transmission ranges.

Because the identification and optimization of key elements, power management circuits and WPT system integration is still missing in current RIC WPT implementations, the aim of this thesis is to model and circuit co-design these systems

obtaining a complete characterization, scalability and optimization methods for this technology. At the same time, new solutions to improve the efficiency of the system and its applicability will be explored, namely: frequency control/adaptation systems, impedance matching systems, relaying policies and ways to circumvent the various challenges precluding practical and robust WPT systems deployment..

In the following sections, the state of the art of resonant inductive coupling wireless power transfer will be explored as well as the problems, objectives and challenges of this thesis.

1.2 Wireless Power Transfer

1.2.1 Radiative and non-Radiative behavior of EM fields

Electromagnetic Wireless Power Transfer consists on the transmission of electric energy through electromagnetic (EM) fields. Because certain behavior characteristics dominate these fields at one distance from the transmitter antenna while completely different ones dominate at another, it is necessary to define some boundary regions to categorize these changes. These boundary regions will allow us to analyze the characteristics of the transmission as a function of distance from the transmitter antenna.

The behavioral changes in the electromagnetic fields are predicted by Maxwell's equations, which define two different behaviors for each of the two terms of electric and magnetic fields (radiative and non-radiative). Maxwell's equations state that the electric fields produced by changes in charge distribution are different from those produced by a change in magnetic field. Similarly, the behavior of magnetic fields produced by changes in electric currents is different from the ones produced by a change in electric fields. In particular, currents and charge distributions directly produce a magnetic field (magnetic dipole type and electric dipole type respectively) that vanishes very steeply with distance, which differs from the fields produced by a change in electric or magnetic fields.

For these reasons, in the spatial region very close to currents and charge distributions, this is, the region very close to the antenna, the electromagnetic field is dominated by electric and magnetic components produced directly by currents and changes in charge distributions. The region were these effects dominate is called the electromagnetic near-field region. On the other hand, at distances far from currents and changes in charge distributions (far from the antenna), the EM field becomes dominated by the electric and magnetic fields indirectly produced by the change in the other type of field, and thus effects of the charges and currents at the EM source are negligible. This part of the EM field -predominantly radiative- constitutes the far field region and it is the familiar type of electromagnetic radiation occurring in "free space".

The difference between these regions can be easily illustrated by solving Maxwell's equations for an infinitesimal dipole (a small radiating wire in the z direction where the axial current along it is uniform):

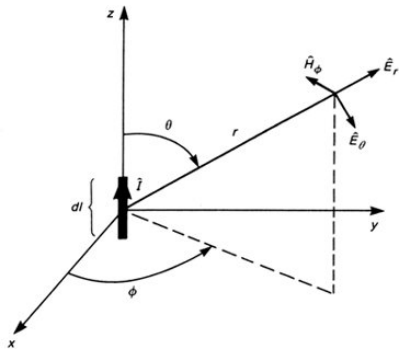

Figure 1.1: Infinitesimal Dipole [2]

The infinitesimal dipole could either be fed with an electric current source creating a vector potential A or a magnetic current source (in the case of magnetic dipoles), creating a vector potential F. In this section we will use both electric and magnetic dipoles to illustrate the differences between the electric and magnetic fields created in each case.

The vector potential A created by an electric current source (J) and the vector potential F created by a magnetic current source (M) are found by:

$$A = \frac{\mu}{4\pi} \iiint_V J \frac{e^{j\frac{2\pi r}{\lambda}}}{r} dv' \tag{1.1}$$

In the case of an electrical infinitesimal dipole, the vector potential A created by an electric current I_e along the z axis [2] is given by:

$$A = a_z \frac{\mu_0 I_e dl e^{-j\frac{2\pi}{\lambda}r}}{4\pi r} \tag{1.2}$$

Similarly, in the infinitesimal dipole, the vector potential F created by a magnetic current I_m along the z axis is:

$$F = f_z \frac{\varepsilon_0 I_m dl e^{-j\frac{2\pi}{\lambda}r}}{4\pi r} \tag{1.3}$$

being a_z and f_z the fields of a small current element, dl the longitude of the infinitesimal dipole, I_e and I_m the electric and magnetic currents of an electrical and magnetic dipole respectively, and r the distance to it. The next step is to find the magnetic field (H) and electric field (E) using the curl of A and F for the

electric and magnetic dipoles, respectively. In order to do this easily, we should first transform A and F to spherical components:

$$\begin{aligned} A_r &= A_z\cos\theta = \tfrac{\mu_0 Idl}{4\pi}(\tfrac{e^{-j\frac{2\pi}{\lambda}r}}{r})\cos(\theta); & F_r &= F_z\cos\theta = \tfrac{\varepsilon_0 Idl}{4\pi}(\tfrac{e^{-j\frac{2\pi}{\lambda}r}}{r})\cos(\theta) \\ A_\theta &= -A_z\sin\theta = \tfrac{\mu_0 Idl}{4\pi}(\tfrac{e^{-j\frac{2\pi}{\lambda}r}}{r})\sin\theta; & F_\theta &= -F_z\sin\theta = \tfrac{\varepsilon_0 Idl}{4\pi}(\tfrac{e^{-j\frac{2\pi}{\lambda}r}}{r})\sin\theta \\ A_\phi &= 0; & F_\phi &= 0 \end{aligned} \tag{1.4}$$

Once the vector potential is known, the radiated fields of the infinitesimal dipole can be found by differentiating the magnetic vector potentials:

$$\begin{aligned} H &= \frac{1}{\mu_0}\nabla\times A = a_\phi\frac{1}{\mu_0 r}[\frac{\partial(rA_\theta)}{\partial r} - \frac{\partial A_r}{\partial\theta}] \\ E &= \frac{1}{\varepsilon_0}\nabla\times F = f_\phi\frac{1}{\mu_0 r}[\frac{\partial(rF_\theta)}{\partial r} - \frac{\partial F_r}{\partial\theta}] \end{aligned} \tag{1.5}$$

And substituting the spherical components of the vector potentials (1.4) into the magnetic and electric fields (1.5) we find:

$$\begin{aligned} H_{e,r} &= H_{e,\theta} = 0 \\ H_{e,\phi} &= \frac{Idl\pi\sin\theta}{\lambda^2}\left[j\frac{\lambda}{2\pi r} + \left(\frac{\lambda}{2\pi r}\right)^2\right]e^{-j\frac{2\pi r}{\lambda}} \\ E_{m,r} &= E_{m,\theta} = 0 \\ E_{m,\phi} &= \frac{Idl\pi\sin\theta}{\lambda^2}\left[j\frac{\lambda}{2\pi r} + \left(\frac{\lambda}{2\pi r}\right)^2\right]e^{-j\frac{2\pi r}{\lambda}} \end{aligned} \tag{1.6}$$

Where $H_{e,r}$ and $H_{e,\phi}$ are the magnetic fields created by the electric current (electrical infinitesimal dipole) and $E_{m,r}$ and $E_{m,\phi}$ are the electric fields created by a magnetic current (magnetic infinitesimal dipole).

Once the magnetic fields of the electrical dipole and the electric fields of the magnetic dipole are known, it is possible to find the electric fields of the electrical dipole and the magnetic fields of the magnetic dipole as:

$$\begin{aligned} E_e &= \frac{1}{j\omega\varepsilon_0}\left[a_r\frac{1}{r\sin\theta}\frac{\partial}{\partial\theta}(H_{e,\phi}\sin\theta) - a_\theta\frac{1}{r}\frac{\partial}{\partial r}(rH_{e,\phi})\right] \\ H_m &= -\frac{1}{j\omega\mu_0}\left[f_r\frac{1}{r\sin\theta}\frac{\partial}{\partial\theta}(E_{m,\phi}\sin\theta) - f_\theta\frac{1}{r}\frac{\partial}{\partial r}(rE_{m,\phi})\right] \end{aligned} \tag{1.7}$$

Considering that the length of the current element is much less than a wavelength (infinitesimal dipole), the electric and magnetic field equations of an electric infinitesimal dipole are:

$$
\begin{aligned}
E_{e,\theta} &= \frac{jZ_0 I_e dl\pi}{\lambda^2}\sin\theta\left[-\left(\frac{\lambda}{2\pi r}\right)^3 - j\left(\frac{\lambda}{2\pi r}\right)^2 + \left(\frac{\lambda}{2\pi r}\right)\right]e^{-j\frac{2\pi r}{\lambda}} \\
E_{e,r} &= \frac{2\pi Z_0 I_e dl}{\lambda^2}\cos\theta\left[-j\left(\frac{\lambda}{2\pi r}\right)^3 + \left(\frac{\lambda}{2\pi r}\right)^2\right]e^{-j\frac{2\pi r}{\lambda}} \\
E_{e,\phi} &= 0 \\
H_{m,\theta} &= -\frac{jI_m dl\pi}{\lambda^2 Z_0}\sin\theta\left[-\left(\frac{\lambda}{2\pi r}\right)^3 - j\left(\frac{\lambda}{2\pi r}\right)^2 + \left(\frac{\lambda}{2\pi r}\right)\right]e^{-j\frac{2\pi r}{\lambda}} \\
H_{m,r} &= -\frac{2I_m dl\pi}{\lambda^2 Z_0}\cos\theta\left[-j\left(\frac{\lambda}{2\pi r}\right)^3 + \left(\frac{\lambda}{2\pi r}\right)^2\right]e^{-j\frac{2\pi r}{\lambda}} \\
H_{m,\phi} &= 0
\end{aligned}
\tag{1.8}
$$

where $Z_0 = 120\pi$ is the free space impedance. It is important to note that while the field components of the infinitesimal electrical dipole are predominantly electric, the field components of the magnetic dipole are predominantly magnetic which will make the magnetic dipole more suitable for near-field wireless power transfer as we will explain later.

Analyzing equations (1.6) and (1.8) we can differentiate three terms:

- Terms proportional to $1/r$. This is called the radiation term and represents the flow of energy away from the wire.
- Terms proportional to $1/r^2$. This is called the induction term and represents the energy stored in the field during one quarter of a cycle and then returned to the antenna in the next.
- Terms proportional to $1/r^3$. This is called the quasi stationary term, or the electrostatic field term, and results from the accumulation of charge at the ends of the element.

Notice that all the terms $\lambda^2/2\pi r$ will be equal to one at the distance $r = \lambda/2\pi$. This distance, where all the contributions from the radiation, induction and the electrostatic term are of the same magnitude, is the boundary between the non-radiative and radiative fields. However, because of the different terms behavior with distance, this separation is not sharp and a mid-range zone (where both radiative and non-radiative fields coexist) has to be defined.

- If $r << \lambda/2\pi$ then the electrostatic and induction field dominate, defining the non-radiative (reactive) near-field zone.
- If $\lambda/2\pi < r < \lambda$ both the induction and radiation term coexist. This is called the mid-range or radiating near field (Fresnel) zone.
- If $r >> \lambda/2\pi$ then the radiation term will dominate, defining the radiative far field (Fraunhofer) zone.

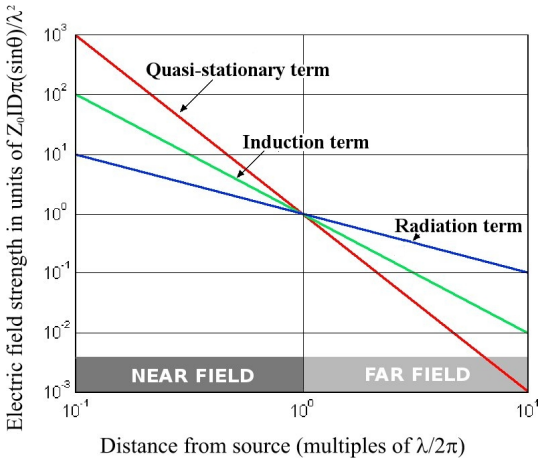

Figure 1.2: Reactive and Radiative terms of electric fields of an Infinitesimal Dipole.

When considering wireless energy transfer, the near field is characterized by only transferring energy efficiently when both the transmitter and receiver are in close proximity. However, because of the near-field proximity to the source, it has a powerful effect on it, causing an increase in the transmitter's load whenever energy is withdrawn from the EM field by a receiver. On the other hand, if the emitted energy isn't withdrawn, it doesn't propagate freely out into space but oscillates back and forth returning its energy to the transmitter and therefore making these systems very efficient. Examples of this type of interaction are magnetic induction in an electrical transformer.

In the mid-range field zone, not only there is an electromagnetic wave being radiated but there is also the reactive component to the electromagnetic field, which makes the radiated power density very hard to predict. Oppositely, the radiative zone of the near field region does not contain reactive field components from the source antenna (back-coupling of the fields becomes out of phase) which makes energy in the radiative near-field to be all radiant energy.

By contrast, the EM far-field is self-sustained in the sense that it requires the same amount of power to transmit the energy to the receiver whether it

is immediately withdrawn or not (the field doesn't go back and forth), this is, the energy on both transmitter and receiver is completely independent. This is because the far field is predominantly radiative making it less dependent on distance (the field decreases as r^{-1} in contrast with r^{-2} and r^{-3} of the reactive field).

Another way to interpret this behavior is that the far field that composes electromagnetic radiation is the part of the electromagnetic field that has traveled sufficient distance from the source so as to become completely disconnected from any feedback to the charges and currents that were originally responsible for it (reactive field). Therefore, the field in this region generates itself only as a result of changing fields.

Also, it is important to note that the fields generated in the near field can be either predominantly magnetic or predominantly electric. Because in the far field the electromagnetic field is only generated as a result of changing magnetic and electric fields, both terms coexist and are very similar (both proportional to $1/r^2$).

In an electric dipole, the near field is predominantly electric ($1/r^3$ term) but in the far field, both electric and magnetic fields vary as $1/r^2$. This is why an electric dipole produces very high electric fields in the near field. In contrast, the magnetic dipole generates a predominantly magnetic field (proportional to $1/r^3$) in the reactive zone which makes magnetic dipoles and other elements that generate high magnetic fields in the near-range very suitable for wireless inductive power transfer.

Because magnetic currents are physically unrealizable it is of interest to find an element that generates a predominantly magnetic field in the reactive zone while being fed with an electric current. One of the elements that has this property is the current loop. In a current loop, although the fields are generated by an electric current, the generated EM field in the near-range zone is predominantly magnetic. The field equations of a sinusoidally excited infinitesimal current loop can be easily found knowing that a small electric loop of radius a and constant electric current I_e is equivalent to a magnetic dipole of magnetic moment $I_m l$ provided that [2]:

$$I_m l = jS\frac{2\pi Z_0 I_e}{\lambda} \tag{1.9}$$

where $S = \pi a^2$ (area of the loop).

The field equations of such current loop thus become:

$$
\begin{aligned}
E_r &= E_\theta = H_\phi = 0 \\
E_\phi &= \frac{jS2\pi^2 Z_0 I_e}{\lambda^3}\sin\theta\left[j\frac{\lambda}{2\pi r}+\left(\frac{\lambda}{2\pi r}\right)^2\right]e^{-j\frac{2\pi r}{\lambda}} \\
H_\theta &= -\frac{S2\pi^2 I_e}{\lambda^3}\sin\theta\left[-\left(\frac{\lambda}{2\pi r}\right)^3-j\left(\frac{\lambda}{2\pi r}\right)^2+\left(\frac{\lambda}{2\pi r}\right)\right]e^{-j\frac{2\pi r}{\lambda}} \\
H_r &= -\frac{jS4\pi^2 I_e}{\lambda^3}\sin\theta\left[-\left(\frac{\lambda}{2\pi r}\right)^3-j\left(\frac{\lambda}{2\pi r}\right)^2+\left(\frac{\lambda}{2\pi r}\right)\right]e^{-j\frac{2\pi r}{\lambda}}
\end{aligned}
\tag{1.10}
$$

Because of these properties, current loops and similar elements (coils, solenoids) are widely used to wirelessly transfer energy through magnetic inductance in the reactive range.

1.2.2 Wireless power transfer using EMR and EMI fields

First theoretically predicted by Maxwell in 1873 and later confirmed by Hertz, wireless power transmission has been illustrated and strongly advocated for in the last century. Although wireless electromagnetic power transfer is achievable in both near and far field, the difference in the behavior of the EM fields explained above requires the development of particular solutions for each particular region.

If the transmitter and receiver are located within the near field, where the reactive component is dominant (whether the source type is predominantly magnetic or electric), the energy is more efficiently exchanged by the use of electromagnetic induction (EMI). In contrast, when the distance between the transmitter and the receiver is such that the system is considered to be in the far field, the radiative component of the EM field dominates and the energy must be transferred by the use of electromagnetic radiation (EMR).

1.2.3 Radiative WPT

The idea of using electromagnetic waves to transmit power has been a subject of research since the development of high-power non-coherent microwave emitters (magnetrons) in World War II and the development of a special antenna with an integrated rectifier (called a rectenna) which converted radiated power back to electricity [3].

The first microwave power transmission demonstration was performed by William C. Brown in 1964 by wireless feeding a miniature helicopter with a combination of an antenna and a rectifier device that would convert microwave

power into electricity, allowing the helicopter to fly [4].

Since then, several experiments have been performed which very well proved and characterized Microwave Power Transmission demonstrating good efficiencies with high directional antennas [5]. In addition, some experiments in the tens of kilowatts range were carried out at Goldstone in 1975 and more recently at Grand Bassin on Reunion Island [6].

Many applications have been proposed for the use of Microwave Power Transfer in aerospace since it was successfully studied and proved in two rocket experiments (MINIX 1983 [7] and ISY-METS in 1993 [8]) and three demonstrations (MILAX 1992, Kansai-demo 1994 and ETHER 1995) carried out by Kobe University. Microwave Power Transfer has been suggested for space elevator applications and beamed microwave sailing, amongst many others [9]. Nowadays, Microwave Power Transmission is currently being a study of research for its applications into a Solar Power Satellite [10, 11] where solar energy is collected in orbit and then converted into microwave energy in order to beam it to a receiver on the ground, such as in the Lunar Wireless Power Transfer [12] and Space Solar Power Systems [13].

Although EMR power transfer has been successfully demonstrated and verified in both mid-range field [14] and far field [2, 15, 16], the requirement of an uninterrupted line of sight within the transmitter and receiver antennas and the pointing requirements of this type of wireless power transmission have constrained these systems to a very specific type of applications.

1.2.4 Non-Radiative WPT

The transmission of wireless power transfer using electromagnetic induction was first demonstrated in the early 20th century by Nikola Tesla. Tesla used electromagnetic induction (EMI) to illuminate incandescent lamps in 1894 [17] and in 1897 he patented a device called the high-voltage resonance transformer or “Tesla Coil”, which was capable of producing very high voltages at high frequency through the transfer of electrical energy from a primary coil to a secondary coil. The principle of operation of this system was magnetic inductive coupling between a pair of resonant coils, known as Resonant Inductive Coupling (RIC). However, typical embodiments involved undesirably large electric fields and thus were thought to be impractical [18]. Tesla’s field of research was stopped and non radiative wireless power transfer was eventually abandoned.

In the 1960s the concept of WPT by electromagnetic induction (EMI) at a lower frequency (kHz) for the powering of artificial hearts was re-introduced [19] jointly with the advancement in high-efficiency switched sources [20]. Since then, inductive coupling has been commonly used in implantable devices [21, 22]. These coupled inductors, such as typical transformers, required a very short distance

between transmitter and receiver (typically in the centimeters range) and usually a magnetic core to confine fields. While the early systems used non-resonant links, later systems [23], [24], [25] implemented resonant transmitter coils thus creating a resonant inductive coupled (RIC) link, similar to Tesla Coils. In such a link each coil is capacitively loaded forming a tuned LC tank resonating at a common frequency, which allows to transmit significant power over a larger range (about 50% of the coil diameter). Inductively coupled resonant and non-resonant links have been used since then in medical and consumer applications. However, the inductive links were limited to the near range (less than the coil diameters) and experimented an exponential decay of efficiency over distance.

In 2007, EMI links were extended to larger ranges (several times the diameter of the antennas) stretching the behavior of RIC links using strong coupling [26]. This effect, explained by coupled mode theory, was demonstrated by lighting a bulb at 2m with a 40% efficiency [27] and attracted a lot of attention in wireless power transfer because of the non-radiative behavior of this method (which makes it safe for humans) and the efficiencies obtained at distances of several meters. This experiment demonstrated how magnetic near field can transfer power through certain materials and around metallic obstacles (even when the direct line of sight was blocked).

Resonant inductive coupling (RIC) in the strong-coupling regime has revived the interest in wireless power transfer and lots of applications are being developed to use these systems in consumer electronics [28, 29], electric vehicles battery charging [30, 31], biomedical implants [32], underwater power transfer [33] and robotics power supply [34], amongst others.

1.3 Previous State of the art on Resonant Inductive Coupling

The difference between RIC systems and conventional transformers is that in a resonant system, both the transmitter (primary) and receiver (secondary) coils can be strongly or loosely coupled (which means that they can share all or only a part of their respective fields) but, as the transmission occurs over a number of field cycles, provided that losses are low, the achievable efficiencies can still be very high. Therefore, loosely coupled but high efficient transmission can be achieved if the transmitter and receiver coils have high Q-factors [35]. Also, as the nature of the electromagnetic field is not radiative but inductive, no direct line of sight is needed.

Because of the potential number of applications that resonant inductive coupling has and the relatively wide range of distances at which RIC systems can transfer power to (from centimeters to tens of meters), RIC is foreseen as a key enabling technology for wireless power transfer in the following years. Although RIC can

theoretically transfer power to tens of meters, there hasn't been any demonstration of this type of wireless power transfer for ranges above 2m. For this to happen, it is necessary to perform a scalable qualitative analysis of the system and to find new ways to increase the transmission and system efficiencies which will allow to increase the distance range. Equally important to optimizing the system's efficiency for the application of RIC is the maximum amount of power that can be sent to the receiving coil using this system. In order to increase the power range of a given configuration, it is necessary to model the effects of a high coupling (high power transfer) with low losses (high Q values) and to system co-design to derive the optimal conditions at which the given figure of merit is maximum.

1.4 Problem Satetement and Objectives

1.4.1 Current Progress on Wireless Power Transfer

As progress unfolds in the field of mid-range wireless power transfer based upon resonant magnetic mid-range coupling -Resonant Inductive Coupling Wireless Energy Transfer (RIC-WPT) [26]-, the scientific community is addressing a collection of challenges at various design levels. Leveraging them would enable myriad applications that would benefit from the availability of wireless remote powering, namely: from consumer electronics to biomedical implants [32], electric vehicle battery charging, underwater power transfer, robotics power supply and fractionated satellites [36], amongst others. However, applications are currently mostly limited to point-to-point links due to the associated complexity of cross-coupling behavior in Single Input - Multiple Output (SIMO) scenarios and therefore do not exploit all the capabilities that RIC-WPT can offer. Furthermore, RIC is envisioned as a key enabling technology for Wireless Sensor Networks, Internet of Things and other naturally SIMO scenarios [37].
This section revises the current State of Art on resonant magnetic wireless power transfer emphasizing the current deficiencies so as to put in context the contributions of this thesis. Aspects related to recent progress in WPT encompass the analysis and design of point-to-point SISO WPT links, from new circuit models to provide a unified design-oriented understanding [38, 39] to load matching techniques to maximize point-to-point coupling efficiency for varying conditions [40, 41]. Point to point systems have also been addressed covering the electronic front-end efficiency optimization [42, 43, 44], as well as their system-wide co-design and optimization [45]. Driven by miniaturized applications, asymmetrical WPT links have been studied to provide design guidelines [46] and optimized operating frequency to minimize losses [47], and even multi-frequency multi-band operation [48]. In point-to-point WPT links, the existence of additional elements or objects altering the link, be it exploring the effect of nearby bodies [49] (or conversely characterizing the impact of RIC upon human exposure [50], or metallic interfering objects [51, 52] has hitherto been studied). In particular, previous research has identified their beneficial effects as relay/repeater elements [50, 53, 54, 55, 56, 57] whereby properly tuned resonant

metallic objects can extend the distance range for which achieving a moderately high efficiency WPT link is feasible. However, the relaying effect and its repercussion upon cross-coupling behaviors and overall system performance in multiple receiver scenarios -in which the benefit of multipath-relay would be very significant- has not yet been analyzed in depth. Regarding multi-node systems, with the advent of new advances that enable more robust WPT links and new applications with multiple receiver scenarios, works for the SIMO WPT scenario include the original investigation in terms of the physical fields [58], power converter perspective [59] and system deployment [60], subsequently on impedance matching techniques extended to the SIMO case both from RF techniques [61] and from a circuit-centric model standpoint [62], analytical description of cross-coupling effects [54] and more recently load-tuned efficiency-optimized charging control for multiple receivers [63] and selective multiple receiver powering [64]. More recently, a system-level analytical description of cross-coupling effects [54] in multiple receiver scenarios has been reported.

Notwithstanding the notable progress of this research field, it is still unclear how a system-wide deployment of a WPT system capable of remotely supplying multiple receiver ends will perform in terms of destructive de-tuning interfering effect or with beneficial constructive range-enhancing effect for the multiple receiver scenarios. To address this crucial question towards the applicability of resonant inductive coupling to a network of devices, this thesis studies the effects of multiple devices acting as relays -potentially increasing the performance of the system through a multi-path relaying effect- or as interfering objects detrimental to the overall system performance.

Accordingly, pursuing the deployment of RIC-WPT technology in multiple receiver applications with inevitable inter-coupling effects, it is necessary to revisit the current models of RIC-WPT systems from the SIMO perspective and to find new performance metrics and analytical procedures to optimize the behavior of such systems and design their parameters in turn predicting their interfering or relaying nature.

1.4.2 Objectives

The aim of this thesis is therefore to first, provide the grounds for analyzing RIC-WPT deployments through a Design-Oriented Unified RIC Model and secondly, to characterize and provide guidelines to overcome the fundamental challenges precluding the development of RIC WPT. A system-codesign methodology is proposed towards optimizing such deployments based on the analytical models presented and the challenges discussed during the thesis. Finally, the scalability of RIC-WPT deployments is analyzed for multiple-input multiple-output applications.

1.4.2.1 Design-Oriented Unified RIC Model

Some analysis of RIC systems in the strong coupling regime have been carried out, but they were based on coupled mode theory [26, 27, 65] failing to provide a practical method to explain how the optimal design parameters of the system could be found (frequency, distances between coils, coil diameters) or how the loose or strong coupling affects the overall efficiency. Being RIC a very multidisciplinary field of research, different approaches have been performed from the antenna point of view [66] [67] and the circuit point of view [68, 69, 38] but there is no model that links them.

It is important to revisit RIC from antenna concepts which can predict very well where optimal distances between transmitter and receiver antennas are and where efficiency can be maximized. Because a coil can be seen as an special type of an antenna, the interaction between a coil and the electromagnetic field can be analyzed as such. To do this, we propose to model this interaction from the electromagnetic and antenna point of view and to use impedance matching techniques to increase the system's efficiency and coupling to the receiving load. In this context this thesis has developed a new model that solves the differences between the existent methods: physical model (coupled mode theory)/circuit model (lump and reflected load theory) and incorporates antenna concepts such as S-matrix and impedance matching techniques to analyze the optimal distances at which maximum efficiency or maximum power transfer occur. This design-oriented model will merge the different existing RIC-WPT models obtaining a unified and scalable model that will allow us estimate the behavior of miniaturized (for active energy harvesting and sensor networks) and non-miniaturized (consumer and in-space applications) RIC systems.

1.4.2.2 Fundamental Challenges I, II and III: Port Impedance Matching, Distance and Frequency Effects, Interfering Objects and Relays

The second section of this thesis analyzes the fundamental challenges that are preventing the widespread deployment of Resonant Inductive Coupling Wireless Power Transfer. Due to the resonant nature of RIC-WPT, these systems are very sensitive to changes on the system load, distance, frequency as well as interfering objects. Thus, this section is aimed to analyze the fundamental challenges of RIC-WPT and provide design guidelines to prevent or circumevent these effects, namely: a) the port impedance matching (through impedance adaptation systems), b) the distance/frequency effects (evaluation of losses and maximization of efficiency) and c) the effects of interfering objects and their potential usage as relaying objects.

Previous studies predicted an increase in power transfer efficiency using impedance matching techniques [68] [70] but failed to show how these techniques interact with the system's efficiency or other known models (circuit based or CMT based). Therefore, it is necessary to model, design and evaluate the interaction of these techniques in the power transfer efficiencies and maximum power transferred

to the load.

1.4.2.3 System Integration & System Co-design

It is furthermore necessary to identify key elements (magnetic coils, power management circuits, and WPT system integration) that are still missing in complete WPT system implementations. Resonant inductive coupling transmission has always been analyzed only taking into account the transmission efficiency itself, but also important to this is the efficiency of the power links and system integration. To increase the overall system's efficiency, it is therefore necessary to identify the key elements that will affect the system from the power circuits point of view, which hasn't been addressed before, and to include these elements into the system co-design process.

A wireless resonant inductive power transfer link can be divided into the power source, the power converters (DC/AC), the link itself and the rectifier power converters (AC/DC). All these parameters should be taken into account when analyzing a wireless power transfer link, so the overall efficiency can be described by:

$$\eta = \eta_{ps} \times \eta_{dc-ac} \times \eta_{link} \times \eta_{ac-dc} \tag{1.11}$$

Therefore, in order to maximize the overall efficiency η the efficiency of the power source η_{ps} as well as the efficiency of the power converter circuits (η_{dc-ac} and η_{ac-dc}) should be taken into account.

1.4.2.4 Scalability

Finally and towards the widespreading of RIC-WPT applications, it is necessary to explore Multiple-Input Multiple-Output WPT deployments. Since the first multi-node deployment was envisioned in [58] there has been a lot of research on point-to-point scenarios while the multi-node scenario has been unexplored. Moreover, new applications of RIC-WPT are in need of new system metrics that capture the behavior of such deployments. The last part of this thesis is therefore devoted to provide a set of metrics that capture the behavior of multi-node RIC-WPT deployments and to analyze the scalability of those systems when the number of nodes is increased.

1.5 Methodology

This thesis is based on the multi-domain closed analytical formulation provided in the first chapter, which unifies the current theories and State of Art on RIC-WPT. The validity of this RIC-WPT model is demonstrated by benchmarking the analytical results with the ones obtained from two different multi-domain tools: first, a Finite Element Field Simulator (FEKO) and secondly a Circuit Simulator (SPICE).

All subsequent chapters are then built on top of the provided analytical formulation and the results obtained are benchmarked with the same tools accordingly. Finally, since some of the work performed on this thesis has been part of the NASA RINGS (Resonant Inductive Near Field Generation System) project, part of the results are verified through an experimental setup consisting on a WPT-RIC system built on top of NASA-MIT SPHERES Satellites, which have been tested on the International Space Station.

Chapter 2

The Theory Behind RIC-WPT: Analytical Models

Contents

2.1 Introduction

Resonant Inductive Coupling Wireless Power Transfer combines aspects of very different fields of research (physical theory of resonators, antenna theory, circuit theory) creating an heterogeneous subject of study. Because of this, very different approaches have been proposed in the literature to predict the behaviour of these systems. Moreover, the metrics used to evaluate the behavior of the power transfer link have not been defined homogeneusly amongst different theories, which has complicated the procedure to understand, analyze and optimize them based on the literature.

In this chapter, two of the leading Resonant Inductive Coupling theories have been revisited (Couped Mode Theory and Reflected Load Theory) and compared to a Circuit-Based approach proposed by the authors (System-Centric Circuit Theory)

in sections 2.2.1,2.2.2 and 2.2.3 respectively. Moreover, the two more relevant metrics in RIC WPT: Power Transfer Efficiency and Power Transferred to the Load have been described and compared for the three analytical approaches, providing the first baseline to be able to understand and to predict the analysis of RIC links with a unified analytical model.
Due to the interest of Multi-Node Wireless Power Transfer to enable the next-generation of wireless energy application, the authors have also proposed an analytical Matrix-Centric formulation of Multi-Node RIC WPT Links, which has been expressed for both the Coupled Mode Theory and Circuit Theory for illustration purposes.
Finally, the last section of this chapter (2.4) has been devoted to provide a critical comparison of the analytical model provided in this chapter with the results obtained through a Finite Element Field Solver (FEKO) and a Circuit-Simulation Software (SPICe).

2.2 Single-Node Wireless Power Transfer

Some analysis of RIC systems in the strong coupling regime have been carried out, but they were based on coupled mode theory [26, 27, 65] failing to provide a practical method to explain how the optimal parameter dimensioning (frequency, distances between coils, coil diameters) of the system could be designed or how the loose or strong coupling affects the overall efficiency. Being RIC a very multidisciplinary field of research, different approaches have been performed from the antenna point of view [66, 67], and the circuit point of view [68, 69, 38, 71]. In this section, the analytical equivalence of these methods is demonstrated together with a new circuit system unified model.

2.2.1 Coupled Mode Theory

Resonant Inductive Coupling was presented using Coupled Mode Theory Form [26] [27]. This model, which is based on the physical theory behind resonators, provides a framework to analyze a wireless power transfer system in strong coupling regime as a first order differential equation. Although it is an approximate method, it does predict very accurately the steady-state response of a Resonant Inductive Coupling link.

In this case, the two coils forming a WPT system with low losses are approximated by two resonators where their time-domain field amplitudes can be described as [38]:

$$\begin{aligned} \dot{a}_1 &= -(j\omega_1 + \Gamma_1)a_1(t) + jK_{12}a_2(t) + F_S(t) \\ \dot{a}_2 &= -(j\omega_2 + \Gamma_2 + \Gamma_L)a_2(t) + jK_{12}a_1(t) \end{aligned} \tag{2.1}$$

where $a_\pm$ is the mode amplitude:

$$a(t)_\pm = \sqrt{\frac{C}{2}}v(t) \pm j\sqrt{\frac{L}{2}}i(t) \tag{2.2}$$

$\omega_{1,2}$ are the eigenfrequencies (frequencies at which the coils resonate), $\Gamma_{1,2}$ are the rates of intrinsic decay due to the coils losses (absorption and radiative), $F_S(t)$ is the excitation applied to the first coil and K_{12} is the coupling rate between both resonant objects:

$$\Gamma_{1,2} = \frac{R_{1,2}}{2L_{1,2}}; \quad K_{12} = \frac{\sqrt{\omega_1\omega_2}k_{12}}{2} = \frac{j\sqrt{\omega_1\omega_2}M_{12}}{2\sqrt{L_1L_2}} \tag{2.3}$$

where ω is the resonant frequency of the system ($\omega_1 = \omega_2 = \omega$), and k_{12} is the mutual coupling between the coils.

In steady state, being $F_S(t)$ a sinusoidal function described as $F_S(t) = A_s e^{-j\omega t}$, the field amplitudes in first and secondary coils are $a_1(t) = A_1 e^{-j\omega t}$ and $a_2(t) = A_2 e^{-j\omega t}$. It can be shown that the amplitudes A_1 and A_2 verify:

$$\frac{A_2}{A_1} = \frac{jK_{12}}{\Gamma_2 + \Gamma_L} \tag{2.4}$$

and therefore the power at the first coil, second coil and load is, respectively:

$$P_1 = 2\Gamma_1|A_1|^2; \quad P_2 = 2\Gamma_2|A_2|^2; \quad P_L = 2\Gamma_L|A_2|^2 \tag{2.5}$$

Finally, the efficiency can be described as the ratio between the power delivered to the load P_L and the total power delivered to the system:

$$\eta_{CMT} = \frac{P_L}{P_T} = \frac{\Gamma_L|A_2|^2}{|A_1|^2\Gamma_1 + |A_2|^2(\Gamma_2 + \Gamma_L)} = \frac{\Gamma_L K_{12}^2}{\Gamma_1(\Gamma_2 + \Gamma_L)^2 + (\Gamma_2 + \Gamma_L)K_{12}^2} \tag{2.6}$$

2.2.2 Reflected Load Theory

Reflected Load Theory has been widely used by electrical engineers to analyze transformers and it is now also used to predict RIC behaviour in the near-field [72][38]. Reflected Load Theory states that the amount of current that flows through the primary coil is affected by the load present in the secondary coil. This load does not appear to the primary coil with the same actual value of the load, but instead as a function of the load value and the mutual impedance between primary and secondary coils.

In reflected load theory, the inductive link is described using the mutual coupling between coils $k_{12} = \frac{M_{12}}{L_1L_2}$ and their quality factors (Q_1, Q_2):

$$Q_{s,x} = \frac{\omega L_x}{R_x}; \quad Q_{p,x} = \frac{R_x}{\omega L_x} \tag{2.7}$$

where $Q_{s,x}$ and $Q_{p,x}$ represent the quality factors of an element placed in series and in parallel respectively.

At resonance frequency, the secondary coil is reflected onto the primary and the value that this coil sees is represented by R_{ref}[38]:

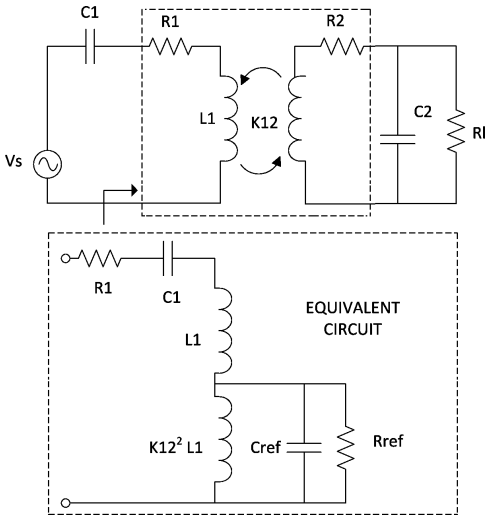

Figure 2.1: Reflected Load Theory Schematic [38]

$$R_{ref} = k_{12}^2 \frac{L_1}{L_2} = k_{12}^2 \omega L_1 Q_{2L} \tag{2.8}$$

where k_{12} is the coupling between the coils and Q_{2L} is the loaded quality factor of the load $Q_{2L} = Q_2 Q_L/(Q_2 + Q_L)$.

Because at resonance the impedance of the two coils is purely resistive, the power provided by the source V_s is divided between R_1 and R_{ref} (which also divides between R_2 and R_L). This leads to the definition of the WPT RIC efficiency for the Reflected Load Theory model:

$$\eta_{RLT} = \frac{R_{ref}}{R_2 + R_{ref}} \frac{Q_2^2 R_2}{Q_2^2 R_2 + R_L} = \frac{k_{12}^2 Q_1 Q_{2L}}{1 + k_{12}^2 Q_1 Q_{2L}} \frac{Q_{2L}}{Q_L} \tag{2.9}$$

2.2.3 System-Centric Circuit Theory

The resonant inductive coupling between two electromagnetic resonators can also be described by lumped element circuit theory using a coupled RLC representation system. In this circuit, the capacitances and inductances model the resonant nature of the loops while the resistors model the radiative and ohmic losses.

In Resonant Inductive Coupling, the effect of the first coil to the second (mutual inductance) can be represented by a compensation source Z_{2M} on such first coil. Similarly, the effect of the second coil to the first one (back EMF) can be represented also by a compensation source Z_{1M}.

$$Z_{2M} = \frac{\omega M_{12} V_{ad}}{Z_1} = \frac{\omega M_{12} V_{ad}}{R_1 + j\omega L_1 + \frac{1}{j\omega C_1}} \tag{2.10}$$

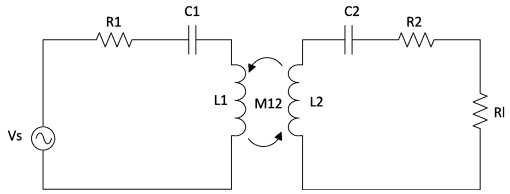

Figure 2.2: Lumped Circuit Theory Schematic

The power at the first coil, second coil and load is:

$$\begin{aligned} P_1 &= \frac{V_{ad}^2}{Z_1} \\ P_2 &= I_2^2 Z_2 = \left(\frac{Z_{2M}}{Z_2 + Z_L}\right)^2 Z_2 = \left(\frac{\omega M_{12} V_{ad}}{Z_1(Z_2 + Z_L)}\right)^2 Z_2 \\ P_L &= I_2^2 Z_L = \left(\frac{Z_{2M}}{Z_2 + Z_L}\right)^2 Z_L = \left(\frac{\omega M_{12} V_{ad}}{Z_1(Z_2 + Z_L)}\right)^2 Z_L \end{aligned} \tag{2.11}$$

where M_{12} is the mutual inductance between coils.

Defining the efficiency as the ratio between the power dissipated in the load (P_L) and the total power ($P_1 + P_2 + P_L$):

$$\eta_{RLC} = \frac{(\omega M_{12})^2 Z_L}{Z_1(Z_2 + Z_L)^2 + (\omega M_{12})^2 (Z_2 + Z_L)} \tag{2.12}$$

The Lumped Circuit system can also be analyzed expressing each subsystem's power transfer functions as gains. Figure 2.3 shows the interrelations between them:

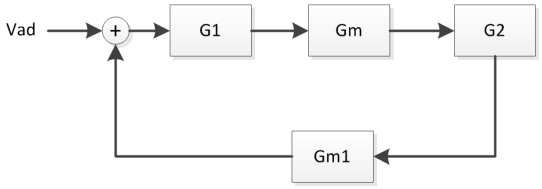

Figure 2.3: Lumped Circuit Theory - Block diagram

Using this model, the current that flows at first and second coils can be written as:

$$I_1 = (V_{ad} + I_2 G_m) G_1; \quad I_2 = (I_1 G_m G_2) \tag{2.13}$$

where G_m is the transfer function from intensity in coil 1 to voltage in coil 2 ($G_m = \omega M_{12}$), G_1 is the transfer function from Voltage to current in first coil and G_2 is the equivalent at second coil:

$$G_1 = \frac{s}{s^2 L_1 + s R_1 + 1/C_1}; \quad G_2 = \frac{s}{s^2 L_2 + s(R_2 + R_L) + 1/C_2} \tag{2.14}$$

where s is the complex frequency $s = j\omega$.

The efficiency of the system can be found by dividing the power transferred to the load by the total power available (power on the source coil plus power dissipated on R_2 and R_L).

$$\eta_{RLC,2} = \frac{I_2^2 R_L}{I_1^2 R_1 + I_2^2 (R_2 + R_L)} = \frac{R_L G_m^2}{R_1 (R_2 + R_L)^2 + G_m^2 (R_2 + R_L)} \tag{2.15}$$

Finally, knowing that the gain functions G_1, G_2 are the inverse of the impedances in coils 1 and 2:

$$G_1 = \frac{1}{Z_1}; \quad G_2 = \frac{1}{Z_2} \tag{2.16}$$

the efficiency can be found equivalent to the one obtained in equation 2.12:

$$\begin{aligned} \eta_{RLC} &= \frac{(\omega M_{12})^2 Z_L}{Z_1 (Z_2 + Z_L)^2 + (\omega M_{12})^2 (Z_2 + Z_L)} \\ &= \frac{G_m^2 Z_L}{\frac{1}{G_1 G_2^2} + G_m^2 \frac{1}{G2}} = \eta_{RLC,2} \end{aligned} \tag{2.17}$$

2.2.4 Analytical Demonstration of Equivalence Between Methods

The Power Transfer Efficiency of Coupled Mode Theory (2.24) can be found equivalent to the efficiency of Reflected Load Theory (2.9) using the relationships between the Q and the Γ factors:

$$K_{12} = \frac{\omega k_{12}}{2}; \quad Q_{s,x} = \frac{\omega L_x}{R_x} = \frac{\omega}{2\Gamma_{s,x}}; \quad Q_{p,x} = \frac{R_x}{\omega L_x} = \frac{\omega}{2\Gamma_{p,x}} \tag{2.18}$$

Substituting these parameters on the power transfer efficiency formulas presented above:

$$\begin{aligned} \eta_{CMT} &= \frac{\Gamma_L K_{12}^2}{\Gamma_1 (\Gamma_2 + \Gamma_L)^2 + (\Gamma_2 + \Gamma_L) K_{12}^2} \\ &= \frac{k_{12}^2}{\frac{Q_L}{Q_1} \left(\frac{Q_2 + Q_L}{Q_2 Q_L} \right)^2 + k_{12}^2 \frac{Q_2 + Q_L}{Q_2}} = \eta_{RLT} \end{aligned} \tag{2.19}$$

Similarly, it can be demonstrated that the efficiencies obtained using Lumped Circuit Theory are also equivalent to the ones obtained by Coupled Mode Theory and Reflected Load Theory by using the relationship between the Q and M_{12} parameters:

$$\begin{aligned} \eta_{RLC} &= \frac{(\omega M_{12})^2 Z_L}{Z_1 (Z_2 + Z_L)^2 + (\omega M_{12})^2 (Z_2 + Z_L)} \\ &= \frac{k_{12}^2 Z_L}{\frac{\omega L_2}{Q_1} \left(\frac{Q_2 + Q_L}{Q_2 Q_L} \right)^2 + \omega k_{12}^2 L_2 \frac{Q_2 + Q_L}{Q_2 Q_L}} = \eta_{RLT} \end{aligned} \tag{2.20}$$

2.3 Multi-Node Wireless Power Transfer

Current challenges behind the deployment and applicability of this technology have driven the necessity for new models that analyze the behavior of RIC links in Multiple Input- Multiple Output scenarios (MIMO). In this section we 1) demonstrate how circuit techniques can be used to analyze RIC-WPT MIMO systems and how they are interrelated with antenna theory and coupled mode theory, 2) derive two point-to-point performance metrics: maximum power transferred to the load (PTL) and maximum power transfer efficiency (PTE) as well as two system-wide performance metrics (net power transferred to the loads and net power transfer efficiency).

2.3.1 Coupled Mode Theory

Extending the two-coil model shown in 2.1 for a MIMO scenario as the one displayed in 2.4 means solving the set of equations for every node with the corresponding cross-couplings between them. In this scenario, it can be demonstrated that the amplitudes verify:

$$\begin{pmatrix} A_1\Gamma_1 \\ A_2\Gamma_2 \\ .. \\ A_n\Gamma_n \end{pmatrix} = \begin{pmatrix} 0 & jK_{12} & .. & jK_{1n} \\ jK_{21} & 0 & .. & jK_{2n} \\ .. & .. & .. & .. \\ jK_{n1} & jK_{n2} & .. & 0 \end{pmatrix} \begin{pmatrix} A_1 \\ A_2 \\ .. \\ A_n \end{pmatrix} + \begin{pmatrix} F_1 \\ F_2 \\ .. \\ F_n \end{pmatrix} \tag{2.21}$$

where F_i are the excitations applied at each node, $K_{i,j}$ is the cross-coupling between them and Γ_i is the rate of intrinsic decay of a given node. Once this is known, the power at each coil is:

$$P_i = 2\Gamma_i |A_i|^2 \tag{2.22}$$

and the power transferred to a load in a coil R is:

$$P_R = 2\Gamma_L |A_R|^2 \tag{2.23}$$

Finally, the efficiency can be described as the ratio between the power delivered to the load and the total power delivered to the system:

$$\eta_{pp,CMT,MIMO} = \frac{P_L}{P_T} = \frac{\Gamma_L |A_R|^2}{\Gamma_L |A_R|^2 + \sum_i \Gamma_i |A_i|^2} \tag{2.24}$$

2.3.2 System Analysis from Circuit Theory

The behavior of a Multi-Node RIC Wireless Power Transfer link can also be derived from the Single-Node expressions in section 2.2.3. If instead of a Single-Node RIC WPT Link a Multi-Node Network (as in figure 2.4) is to be analyzed, the set of equations that define the behavior of the system is:

$$\begin{pmatrix} I_1 \\ I_2 \\ .. \\ I_n \end{pmatrix} = \begin{pmatrix} 0 & G_{21}G_1 & .. & G_{n1}G_1 \\ G_{12}G_2 & 0 & .. & G_{n2}G_2 \\ .. & .. & .. & .. \\ G_{1n}G_n & G_{2n}G_n & .. & 0 \end{pmatrix} \begin{pmatrix} I_1 \\ I_2 \\ .. \\ I_n \end{pmatrix} + \begin{pmatrix} V_1G_1 \\ V_2G_2 \\ .. \\ V_nG_n \end{pmatrix} \tag{2.25}$$

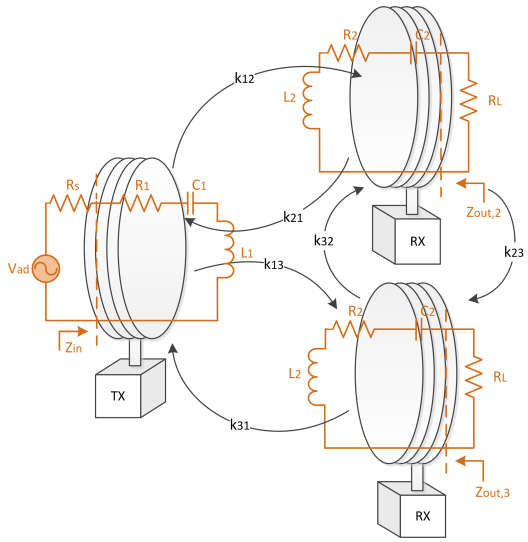

Figure 2.4: Circuit Diagram of a 3-Coil SIMO RIC-WPT link

where G_1, G_2, .., G_n are the gains of the coils ($G_i = 1/Z_i$), G_{ij} is the coupling between them ($G_{ij} = \omega M_{ij}$) and V_i is the input voltage applied at each coil.
The power at the each coil is then:

$$P_i = |I_i|^2 Z_i; \quad P_L = |I_j|^2 Z_L \tag{2.26}$$

where M_{12} is the mutual inductance between coils, $Z_i = R_i + j\omega L_i + 1/j\omega C_i$ is the total impedance of the coil and Z_L is the load impedance. The efficiency is defined as the ratio between the power dissipated in the load (P_L) and the total power ($\sum_i P_i$):

$$\eta_{RLC,MIMO} = \frac{|I_j|^2 Z_L}{|I_j|^2 Z_L + \sum_i |I_i|^2 Z_i} \tag{2.27}$$

2.4 Multi-Domain Cross-Model Validation

The performance of a RIC-WPT link depends upon the characteristics of the link nodes (technology, geometry) and the relationship between them (distance, alignment between antennas), which can be described analytically as a step prior to the link design and deployment. An analytical study of link components and the complete structure of the network are required in order to a) characterize its behavior, so as to predict its response and an eventual deterioration of results if a change in operation conditions occurs; and b) provide guidelines for an optimal design which maximizes the desired parameters (for instance, Power Transfer Efficiency as a key feature in the case of RIC-WPT).

State of the art of RIC-WPT link characterization includes models of both antenna impedance (loop antenna in the case of this work [73]) and RIC-WPT link

(asymmetric, multipoint networks in the most general case [2]). While existing models are applied to static operation conditions (no change in coupling factors or load), new applications of RIC-WPT emphasize the necessity to explore these links for more demanding scenarios: a change in operation conditions (a sudden change in distance or alignment between antennas) and the presence of interfering objects, which will detune the link and deteriorate its performance.

In order to perform an analytical study of those situations, a revision of existing models is required to ensure that the analytical description matches actual behavior of both antennas and the complete RIC-WPT link under these more challenging conditions. So as to ensure that correspondence, this section presents a critical comparison between analytical and circuit-based models for the case of an asymmetric, Single-Input-Multiple-Output (SIMO), RIC-WPT link composed of loop antennas.

2.4.1 Overview

The verification of the analytical models consists of 1) validation of the antenna impedance model, which is the basic component of the RIC-WPT link; and 2) verification of the system model for the whole RIC-WPT link. This validation is performed by comparing time and frequency domain responses corresponding to analytical and circuit-based models as depicted at figure 2.5.

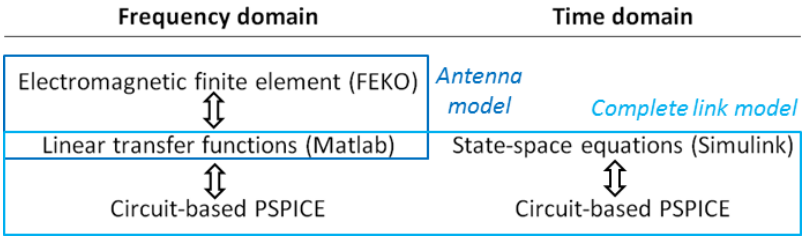

Figure 2.5: A critical comparison of antenna and link models.

Regarding the loop antenna model, the study in [40] is revisited and the impedance expression is verified by comparing an analytical expression (explored with Matlab) to the response of a finite element field solver (FEKO). Concerning the RIC-WPT link analysis in [40], expressions in the frequency domain (linear transfer functions explored in Matlab) are verified with the circuit-based PSPICE model. Regarding time domain, a state-space equations model is presented and implemented with Simulink and its results are corroborated with the circuit-based, time domain PSPICE model.

2.4.2 Critical comparison of loop antenna impedance models

The analytical expression for a loop antenna impedance [40, 73] is revisited in this section so as to compare its response with a finite element field solver (FEKO) and thus confirm its validity. Two expressions for loop antenna impedance are presented

in this section. They are both a simplification of coil impedance for frequencies close to resonant frequency. The first is the model which provides the first resonance of the loop antenna, and it includes frequency-dependent capacitive and resistive losses; the second is a series equivalent for its impedance at frequencies close to resonance. The series model detailed in this section aims to restrict the resistive losses to a constant value, which is required for the simulator software (Simulink, PSPICE) used in the following sections.

2.4.2.1 First-resonance Model of Antenna Impedance

The impedance of a loop antenna can be modeled by an inductive component L, a capacitor C and some resistive losses R [73], as depicted in figure 2.6. Using this

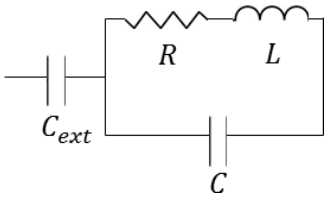

Figure 2.6: First-resonance model of loop antenna impedance

simplified model, the impedance of the coil can be expressed as:

$$Z_{coil} = \frac{1}{j\omega C_{ext}} + \left((j\omega L) + R(\omega) \right) || \frac{1}{j\omega C} \right) \tag{2.28}$$

where C stands for the internal parasitic capacitance, C_{ext} is an external capacitor added to adapt the resonant frequency of the coil and $R(w)$ are the losses of the loop antenna. Revisiting [74], resistive losses of an electrically small ($a << \lambda$) circular loop antenna (chosen for its low radiation resistance [39]) are considered.

These losses depend upon its constituent materials (σ, δ) and geometry (a, b, c) and can be divided into Radiative Losses (R_r), Ohmic Losses (R_o) and Dielectric Losses (R_d) [2]:

$$R = R_r + R_o + R_d \tag{2.29}$$

The radiation losses of a circular N-turn loop antenna with loop radius a can be expressed as:

$$R_r = 20\pi^2 N^2 (\frac{2\pi a}{\lambda})^4 \tag{2.30}$$

where N is the number of turns of the loop antenna, a is its radius and λ is the operation wavelength.

The ohmic resistance, which is in general much larger than the radiation resistance, depends upon the proximity effect (if the spacing between the turns in the loop antenna is small) and the skin effect. The total ohmic resistance for an N-turn circular loop antenna with loop radius a, wire radius b and loop separation $2c$ is given by:

$$R_o = \frac{Na}{b} R_s \sqrt{\frac{R_p}{Ro} + 1} \tag{2.31}$$

where $R_s\sqrt{\omega\mu_o/2\sigma}$ is the surface impedance of the conductor and R_p is the ohmic resistance per unit length due to proximity effects. Finally, if a dielectric loop antenna is considered, the dielectric losses are given by:

$$R_d = \frac{\tan(\delta)}{\omega C} = \omega L \tan\delta \simeq \omega 4\mu_o a N^2 \tan\delta \tag{2.32}$$

where $\tan\delta$ is the loss tangent of the coil and L has been approximated to $L = 4\mu_o a N^2$.

Once the losses have been found, these can be expressed as a set of constants with a given frequency dependance:

$$R = R_r + R_o + R_d = C_r\omega^4 + C_o\sqrt{\omega} + C_d\omega \tag{2.33}$$

where:

$$\begin{aligned} C_r &= \frac{20\pi^2 N^2 a^4}{c_o^4} \\ C_o &\simeq \frac{Na}{b}\sqrt{\frac{\mu_o}{2\sigma}} \\ C_d &\simeq 4\mu_o a N^2 \tan\delta \end{aligned} \tag{2.34}$$

2.4.2.2 Series Model of Antenna Impedance

The impedance expression of a resonator can be simplified to an RLC series equivalent (Fig. 2.7) with constant resistive losses in a narrow band around the resonant frequency ($\omega \simeq \omega_o$) when the quality factor of the resonator is very high: $Q = \omega_o\frac{L_s}{R_s} \simeq \frac{R(\omega_o)}{\omega_o L}$, which gives the following expression for $Q >> 1$ and $\omega \simeq \omega_o$:

$$Z_{coil}(\omega) \simeq R_s + j\omega L_s + \frac{1}{j\omega C_s} \tag{2.35}$$

where $R_s \simeq R(\omega_o)Q^2$, $L_s \simeq L$ and $C_s \simeq C||C_{ext}$.

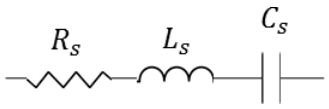

Figure 2.7: RLC series equivalent for impedance loop antenna

2.4.2.3 Results

The presented expressions for analytical loop antenna impedance (both the first-resonance version and the series model) are swept with Matlab and obtained results are compared to those provided by FEKO. Fig. 2.8. shows real and imaginary components of loop antenna impedance (normalized to their maximum: 4.6387MΩ for the real component and 2.3207MΩ for the imaginary component) with respect

to frequency normalized to resonant frequency of the coil (8.5MHz). The simplified expression of losses in (2.33) for a dielectric-less coil ($R_d = 0$) is represented, superimposing impedance measured with FEKO, first-resonance model impedance in (2.28), and series version of coil impedance in (2.35). C_o and C_r parameters in first-resonance model have been obtained with an iterative fitting performed with Matlab, which aimed to match FEKO response to analytical expression in (2.28).

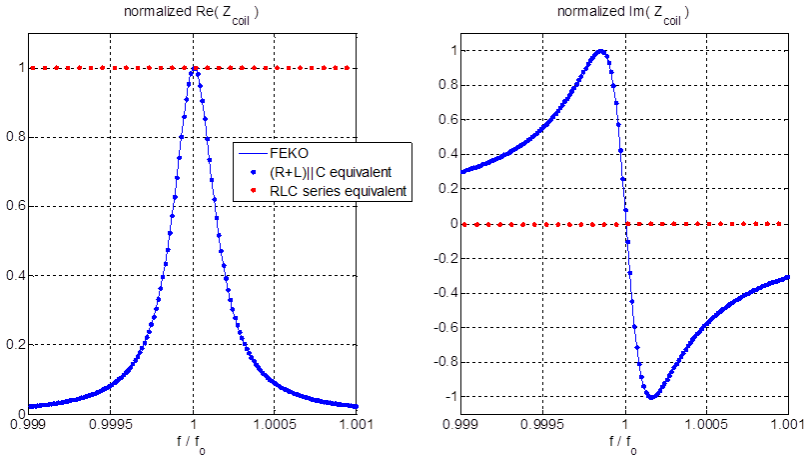

Figure 2.8: Loop antenna impedance verification

In figure 2.8 it can be seen that while the analytical first-resonance model matches the FEKO-obtained impedance (both Re(z) and Im(z)), the simplified series model is only valid at the resonant frequency.

2.4.3 Critical Comparison of RIC-WPT link models

This section introduces the critical comparison of models used to describe a RIC-WPT link (linear transfer functions, state-space equations), whose results will be compared to the circuit-based PSPICE model in order to verify the correspondence between the analytical model and the response of the system.

Comparison is performed in terms of a SIMO (Single Input Multiple Output) link in which a transmitter coil is coupled to two receivers (one being the receiver coil and the second an interference). Antennas are modelled in terms of the aforementioned narrow-band equivalent of coil impedance and their coupling is expressed in terms of the mutual inductances.

A general overview of this link is depicted in Fig. 2.9, where $f_{1,2,i}$ stand for transmitter, receiver and interfering coil resonant frequencies respectively and f_{ad} is the frequency of operation. Antenna impedances are represented as $Z_{1,2,i}$, and there is a load connected to receiver coil named $R_{load,2}$ to represent the circuit which will harvest the transferred power. There is also a load connected to the interfering coil, $R_{load,i}$, to illustrate that any receiver could be seen as an interference from

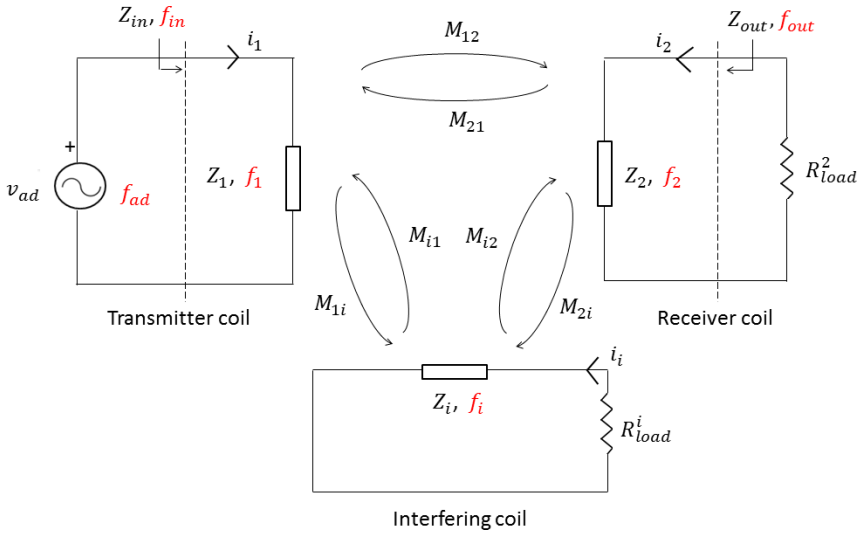

Figure 2.9: RIC-WPT SIMO link

the point of view of the rest of receivers. Coupling effects between link components are expressed in terms of mutual inductances M_{12}, M_{21} (between transmitter and receiver coils), M_{1i}, M_{i1} (between transmitter and interfering coils) and M_{2i}, M_{i2} (between receiver and interfering coils)[52].

2.4.3.1 Linear Transfer Function Model (frequency domain)

Using the frequency domain analysis from previous sections which relates phasor currents, mutually induced voltages and impedances, we can describe the link behavior as in Fig. 2.9. Equation system in 2.36 represents this interrelationship: V_{ad} is the voltage source; $I_{1,2,i}$ stand for currents in transmitter, receiver and interfering coils respectively; G_n are the coil addmitances and $G_{n,m}$ is the cross-admittance for voltage induced in coil m due to the current in coil n.

$$\begin{pmatrix} I_1 \\ I_2 \\ I_i \end{pmatrix} = \begin{pmatrix} 0 & G_1G_{21} & G_1G_{i1} \\ G_2G_{12} & 0 & -G_2G_{i2} \\ G_iG_{1i} & -G_iG_{2i} & 0 \end{pmatrix} \begin{pmatrix} I_1 \\ I_2 \\ I_i \end{pmatrix} + \begin{pmatrix} V_{ad}G_1 \\ 0 \\ 0 \end{pmatrix} \tag{2.36}$$

where

$$\begin{aligned} G_{nm} &= \frac{V_{nm}}{I_n} j\omega M_{nm} \\ M_{nm} &= k_{nm}\sqrt{L_nL_m} \\ G_n &= \frac{1}{Z_n} \\ Z_1 &= R_1 + j\omega L_1 + \frac{1}{j\omega C_1} \\ Z_{2,i} &= R_{2,i} + R_L^{2,i} + j\omega L_{2,i} + \frac{1}{j\omega C_{2,i}} \end{aligned} \tag{2.37}$$

and $n, m = 1, 2, i$.

The former equation system can be translated to the block diagram shown in figure 2.10, from which analytical expressions to characterize the link in terms of currents at the coils can be obtained[75]:

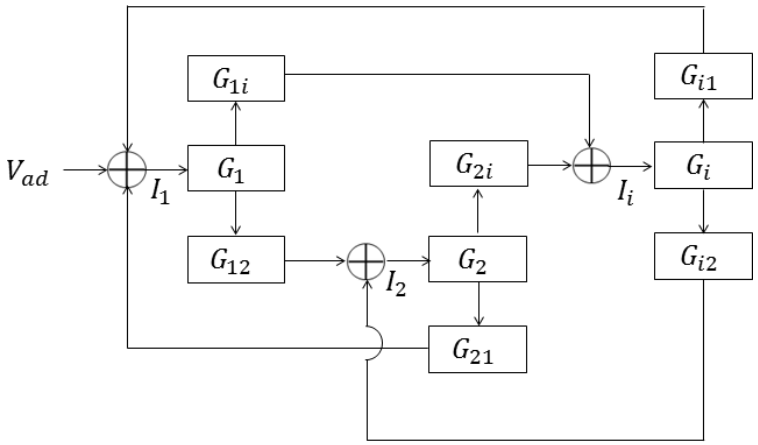

Figure 2.10: Block diagram of a RIC-WPT

$$
\begin{aligned}
I_1 &= V_{ad}\frac{G1}{1+A+B} \\
A &= G_1 G_{i1}\frac{(G_i G_{1i} + G_i G_2 G_{12} G_{2i})}{1 + G_i G_2 G_{2i} G_{i2}} \\
B &= G_1 G_{21}\frac{(G_2 G_{12} + G_i G_2 G_{1i} G_{i2})}{1 + G_i G_2 G_{2i} G_{i2}} \\
I_2 &= I_1\frac{G_2 G_{12} + G_i G_2 G_{i1} G_{i2}}{1 + G_i G_2 G_{2i} G_{i2}} \\
I_i &= I_1\frac{G_i G_{1i} + G_i G_2 G_{12} G_{2i}}{1 + G_i G_2 G_{2i} G_{i2}}
\end{aligned}
\tag{2.38}
$$

2.4.3.2 State Space Equations Model (time domain)

Time domain analysis of a RIC-WPT link can be performed in terms of state-space equations which enables the study of the transient response, sudden changes in operation conditions and simulation of switching dynamics (which wil be useful if an adaptive energy management control structure is to be implemented with switching power converters [76]). The state-space equations model considers capacitor, inductor and resistor voltages and coil currents as shown in figure 2.11, where v_{ad} stands for time-domain voltage source and v_{nm} is the induced voltage in coil m due to the current in coil n (CCVS controlled by the current in the coil that is coupled). The

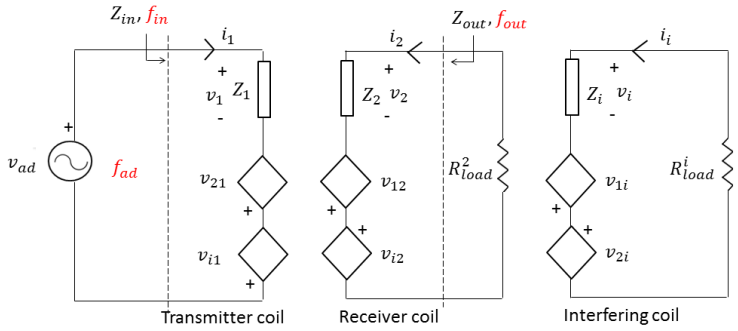

Figure 2.11: State-space equations model of a RIC-WPT link

set of equations that describe the state-space equations model is:

$$\begin{aligned}
v_{L_1} &= v_{ad} + v_{21} + v_{i1} - v_{c_1} - v_{R_1} \\
v_{L_2} &= v_{12} - v_{i2} - v_{c_2} - v_{R_2} - v_{R^2_{load}} \\
v_{L_i} &= v_{1i} - v2i - v_{c_i} - v_{R_i} - v_{R^i_{load}} \\
i_n &= \frac{1}{L_n} \int v_{L_n}(t)dt \\
v_{R_n} &= i_n R_n \\
v_{C_n} &= \frac{1}{C_n} \int i_n(t)dt \\
v_{nm} &= M_{nm} \frac{di_n}{dt} = \frac{M_{nm}}{L_n} v_{L_n}
\end{aligned} \tag{2.39}$$

where $n, m = 1, 2, i$.

2.4.4 Circuit-based PSPICE model

The Circuit-based PSPICE model described in this section is used to compare and validate the two previously described models: the block diagram model (used to obtain the analytical expression of the system as well as for frequency domain verification) and the state-space equation model (applied to time-domain tests). The circuit diagram (shown in figure 2.12) is a direct representation of a RIC-WPT link in which the coupling coefficients ($k_{nm}, n, m = 1, 2, i$) are implemented by means of the "k-linear" component (SPICE Analog Library). Resistive losses in this model refer to the constant resistor value of the series impedance simplification in (7).

2.4.4.1 Results

Using the verified antenna impedance models in section 2.4.2 (in particular, the series impedance simplification), the WPT link model has been built and simulated with the corresponding tools: state space equations model is implemented

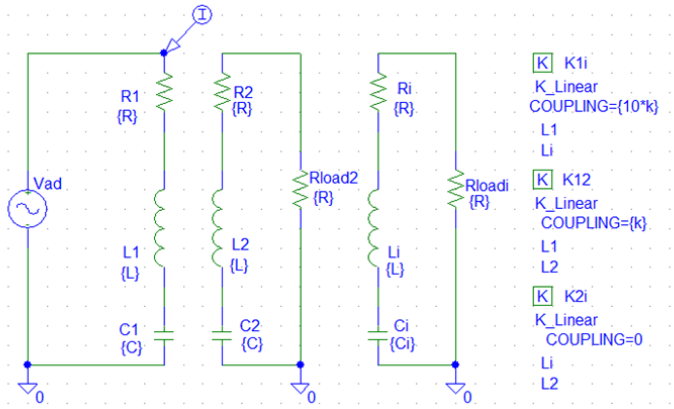

Figure 2.12: PSPICE model of a RIC-WPT SIMO link

with Simulink and run in time domain; circuit-based model is simulated with PSPICE, both in time and frequency domains; and a frequency sweep is performed with the linear transfer function model with Matlab. This section presents the results for the WPT models verification both in the frequency and time domains.

This analytical characterization of a link can be later complemented with the introduction of a correction circuit (for instance an Automatic Impedance Matching network [76, 37] to enhance performance once the link has been deployed. The goal of this circuit is to maintain power transfer even in the presence of interfering objects, this is, to make the non-idealities transparent for the transmitter front-end. With this application in mind, transmitter power and shape of transmitter current will be used to illustrate deterioration in performance due to the presence of an interfering coil.

Figure 2.13 shows the transmitted power (frequency domain) for different coupling scenarios, comparing the linear transfer function model implemented with Matlab and the circuit-based PSPICE model.

Figure 2.14 shows the current at the transmitter and provides a comparison between the state-space equations model implemented with Simulink and the circuit-based PSPICE model. It can be seen that both analytical models (linear transfer function and state-space equations) accurately match the results from the RIC-WPT link behavior modeles with circuit-based PSPICE.

2.5 Conclusions

Recent progress in RIC-WPT technology has opened the door to new multi-node designs and configurations, which require a better understanding and modeling of the frequency and time-domain response of these systems. For this purpose, this chapter has presented a review of the current time-domain and frequency-domain RIC-WPT models (applied to multi-node scenarios) and provides a critical comparison of their

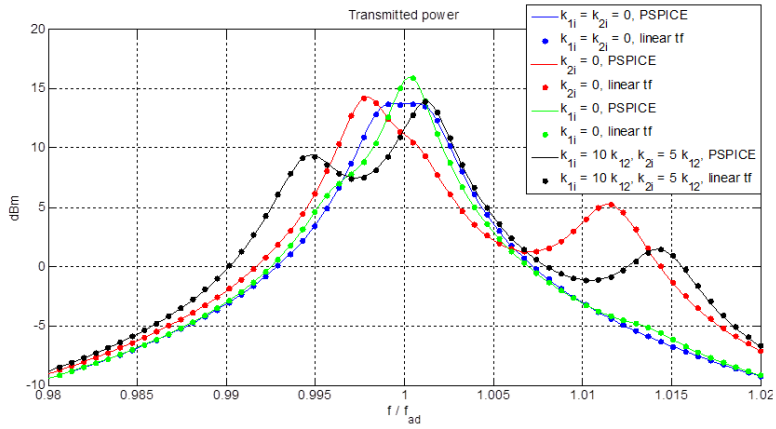

Figure 2.13: Frequency domain results for RIC-WPT link model verification

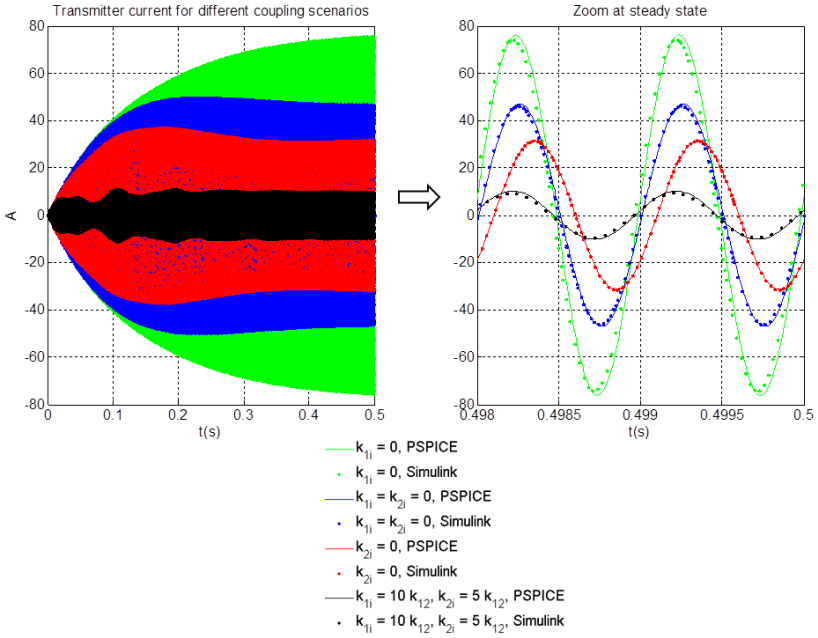

Figure 2.14: Time domain results for RIC-WPT link model verification

behavior by benchmarking the results to the ones obtained with both a finite element field solver (FEKO) and a circuit based software (PSPICE). The model analysis and verification has been divided in two steps: the antenna impedance model (obtained analytically and verified with FEKO) and the multi-node model (both in the time and frequency domains, which has been validated using PSPICE). The results obtained in both steps have confirmed a very close match between FEKO/PSPICE and the derived models, thus validating its usage for link behavior prediction, system

design and the application of correction schemes.

Chapter 3

Fundamental Challenges I: Port Impedance Matching

Contents

3.1 Introduction

As seen in chapter 2, the efficiency of a RIC-WPT system as well as the achievable power transferred to the load is greatly affected by the transmitter (source) and receiver loads. In this chapter, the effects of an impedance mismatch between source and load are studied and an nanalytical formulation is derived to maximize power transfer efficiency and power transferred to the load upon certain operating conditions. In this chapter we will provide an analytical formulation of optimal load (when source or transmitter load is fixed) to achieve maximum power transfer or maximum efficiency. Later, a bi-conjugate matching system is analyzed (where both source and load impedances can be adapted) in order to maximize power transferred to the load and efficiency together with a closed formulation of the maximum efficiency achievable under these conditions.

3.2 Optimal Load: Output Impedance Matching

In RIC systems, there is an optimal load that maximizes the power transfer efficiency for each distance between transmitter and receiver. Also, there is an optimal

load which maximizes power transferred to the load. Different techniques to maximize efficiency can be found in the literature, namely: analytical maximization of efficiency (derivating the efficiency expression with respect to Z_L), impedance matching techniques and variation of distance between transmitter and receiver. In this section, we will review two optimal load contidions to maximize either power transfer efficiency or power transferred to the load.

3.2.1 Maximization of Power Transfer Efficiency

Once the power transfer efficiency is found, we can differentiate the efficiency expression obtained in the previous chapter (4.4) using Circuit Theory with respect to the load impedance R_L to obtain the optimal load:

$$R_{L,RLC} = \sqrt{R_2^2 + \frac{R_2}{R_1}(\omega M_{12})^2} \tag{3.1}$$

The same procedure could be done in Coupled Mode Theory for Γ_L, obtaining:

$$\Gamma_{L,CMT} = \sqrt{\Gamma_2^2 + \frac{\Gamma_2}{\Gamma_1}K_{12}^2} \tag{3.2}$$

Once again, by using the previously derived relationships in 2.18) in equations (3.1) and (3.2) we can demonstrate that both are equivalent:

$$R_{L,CMT} = 2L_2\sqrt{\left(\frac{R_2}{2L_2}\right)^2 + \frac{R_2 L_1}{R_1 L2}\frac{\omega^2 M_{12}^2}{L_1 L_2}} = R_{L,RLC} \tag{3.3}$$

3.2.2 Maximization of Power Transferred to the load

To maximize the power transferred to the load, it is necessary to perform an impedance match between source and load. To do this, we must first find the output impedance seen by the load. From the circuit model in 3.1:

$$Z_{out} = j\omega L_2 - \frac{j}{\omega C_2} + R_2 + \frac{(\omega M_{12})^2}{j\omega L_1 - \frac{j}{\omega C_1} + R_1} \tag{3.4}$$

Once Z_{out} is known, the load should be conjugately matched to the output resistance: $Z_{out} = Z_L^*$.

$$Z_{L,RLC} = \left(\frac{j}{\omega C_2} - j\omega L_2\right) + \sqrt{R_2^2 + (\omega M_{12})^2\frac{R_2}{R_1}} \tag{3.5}$$

At resonance, $Z_L = Z_{out}*$ becomes purely real:

$$R_L = \sqrt{R_2^2 + (\omega M_{12})^2\frac{R_2}{R_1}} = R_{L,CMT} = R_{L,RLC} \tag{3.6}$$

3.3 Optimal Load and Source: Bi-Conjugate Matching

3.3.1 Maximization of Power Transfer and Efficiency

The efficiency has been defined differently in the literature: while some of the studies calculated the efficiency as the ratio of the currents in the source and device coils (which doesn't take into account the coupling between source and load) [26][27] other studies reported the efficiency as the ratio between the power available from the source to the power dissipated in the load [77]. To take into account the impedance of the source, it is necessary to re-write the efficiency and quantify the power reflected at the source. Using circuit theory, we can recalculate the efficiency as the ratio between the power dissipated on the load and the power delivered to the source coil extracted from the power source:

$$\eta = \frac{R_L(\omega M_{12})^2}{(\omega M_{12})^2(R_2+R_L)+R_1(R_2+R_L)^2}\left[1-\left|\frac{Z_{in}-Z_s}{Z_{in}+Z_s}\right|^2\right] \tag{3.7}$$

To maximize power transfer efficiency, we can now use conjugate matching at the source to find the optimal Z_s value and adapt Z_L to the optimal load found in 3.3.

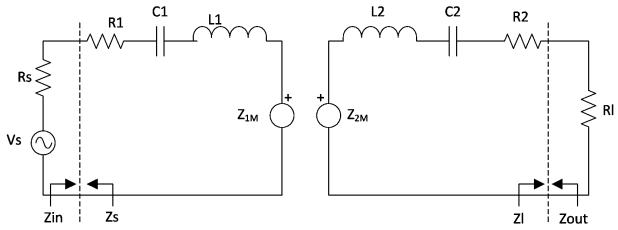

Figure 3.1: RIC System from Circuit Theory with Source and Load Impedances

The resulting value is equivalent to conjugately matching source and load to Z_{in} and Z_{out} respectively [77].

$$\begin{aligned}
Z_{in}(d) &= Z_1 + \frac{(\omega M_{12}(d))^2}{Z_2+Z_L} \\
Z_{out}(d) &= Z_2 + \frac{(\omega M_{12}(d))^2}{Z_1+Z_s} \\
Z_L(d) &= \left(\frac{j}{\omega C_2} - j\omega L_2\right) + \sqrt{R_2^2 + (\omega M_{12}(d))^2\frac{R_2}{R_1}} \\
Z_S(d) &= \left(\frac{j}{\omega C_1} - j\omega L_1\right) + \frac{R_1}{R_2}\sqrt{R_2^2 + (\omega M_{12}(d))^2\frac{R_2}{R_1}}
\end{aligned} \tag{3.8}$$

If the resonators are equal ($C_1 = C_2 = C$ and $L_1 = L_2 = L$) and the system is operating at resonance $\omega = \omega_0 = 1/\sqrt{LC}$, source and load impedances can be simplified to:

$$R_S = \frac{R_1}{R_2}\sqrt{R_2^2 + (\omega M_{12})^2\frac{R_2}{R_1}}; R_L = \sqrt{R_2^2 + (\omega M_{12})^2\frac{R_2}{R_1}} \tag{3.9}$$

The same procedure could be performed using Coupled Mode Theory by defining the efficiency between the delivered power to the load P_L and the power available from the source $F_S(t)$. This will take into account the impedance at the source and load and will allow us to compute the behavior of the back electromagnetic field that the second coil generates in the first one, yielding:

$$\eta_{CMT} = \frac{P_L}{P_S} = \frac{\Gamma_L \Gamma_S |A_2|^2}{|A_s|^2} \tag{3.10}$$

where $P_S = 2|A_s|^2/\Gamma_S$, and it can be shown from (2.1) that for an initial $F_S(t) = A_s e^{-j\omega t}$:

$$\begin{aligned} A_1(\Gamma_1 + \Gamma_s) &= jK_{12}A_2 + A_s \\ \frac{A_1}{A_s} &= \frac{\Gamma_2 + \Gamma_L}{(\Gamma_S + \Gamma_1)(\Gamma_2 + \Gamma_L) + K_{12}^2} \\ \frac{A_2}{A_s} &= \frac{jK_{12}(\Gamma_2 + \Gamma_L)}{(\Gamma_S + \Gamma_1)(\Gamma_2 + \Gamma_L) + K_{12}^2} \end{aligned} \tag{3.11}$$

Once the relation between A_2 and A_S is known, the efficiency is expressed as:

$$\eta_{CMT} = \frac{\Gamma_L K_{12}^2 \Gamma_S}{[(\Gamma_S + \Gamma_1)(\Gamma_2 + \Gamma_L) + K_{12}^2]^2} \tag{3.12}$$

To maximize the power transfer efficiency we could derive η_{CMT} over Γ_S and Γ_L, finding, respectively:

$$\begin{aligned} \Gamma_{L,o} &= \sqrt{\Gamma_2^2 + \frac{\Gamma_2}{\Gamma_1} K_{12}^2} \\ \Gamma_{S,o} &= \sqrt{\Gamma_1^2 + \frac{\Gamma_1}{\Gamma_2} K_{12}^2} \end{aligned} \tag{3.13}$$

which provide the same optimal values for $\Gamma_{L,o}$ and $\Gamma_{S,o}$ that were obtained by conjugately matching source and load impedances in lumped circuit theory thereby demonstrating the equivalence between these two methods. Looking at the results from Optimal Load and Optimal Bi-Conjugate mathcing, it is possible to see that the only difference between maximum efficiency and maximum power is the choice of source impedance, where on the former is ideally zero and the latter a bi-conjugate match. Interestingly, the optimal load for both, (3.1) and (3.8) is equivalent when $R_S = 0$, thus the load for optimal power transfer is also the one for the maximum efficiency (the case of zero real source impedance).

3.3.2 Distance Effects on Bi-Conjugately Matched Systems

It can be seen in equation 3.8 that Z_{in} and Z_{out} vary when the distance between the two coils is modified (which modifies M_{12}). To compensate this effect, it will be necessary to apply a different impedance in source and load for each value of distance (separation between drive and load coils). Therefore, because a variation in distance modifies load and source impedances, there are two options to maximize the power transfer efficiency:

- If the system has fixed source and load impedances, it is necessary to modify the distance between transmitter and receiver.
- If the system has a variable distance, we should compensate this by adapting the impedances in source and load.

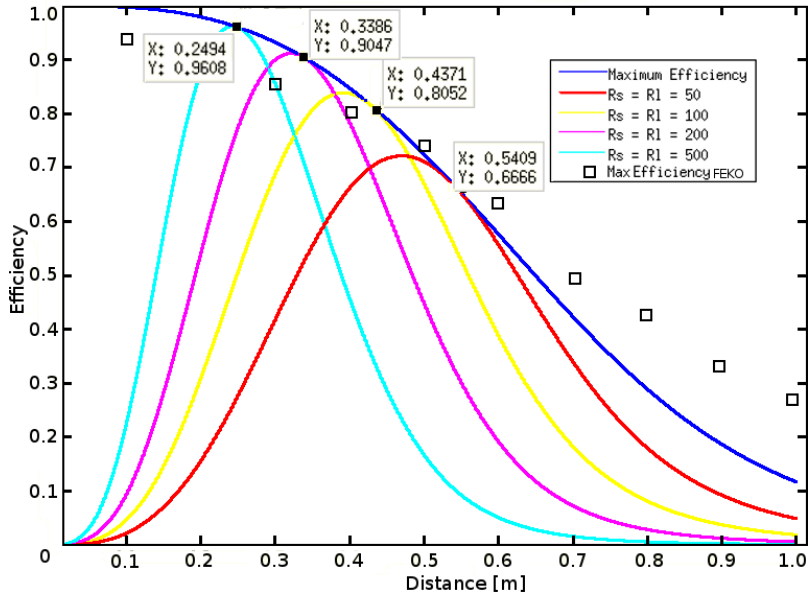

Figure 3.2: Efficiency of static impedances over distance and dynamic variation of impedance (maximum achievable efficiency).

In figure 3.2 the efficiency of the system for different values of $R_S = R_L$ has been superimposed upon the maximum theoretical efficiency achievable (obtained under variable distance adaptive impedance matching conditions) and the maximum efficiency obtained with the Finite Element Field Solver FEKO. These results were obtained from a two-coil copper-made RIC link with coil radius $a = 0.5m$, wire radius $b = 5mm$ and $R_1 = R_2 = 10\Omega$. It can be seen that the static curves are equal to the maximum efficiency limit when the distance within the coils forces the input and output impedance of the system to be the same as the source and load resistors, this is, when an impedance match occurs. It can be observed that given a value for the source and load resistors ($Z_S = Z_L = R_S = R_L$) there is an optimal distance at which the input and output impedances are perfectly matched ($R_L = R_S = R_{in} = R_{out}$). To obtain this distance it is necessary to find the mutual inductance between coils. In the quasi-static limit and at large distances ($D >> a$), a coil behaves as an electrically small antenna and the magnetic flux density at the second coil as a result of the first has the form of a dipole [1]:

$$B = \frac{\mu_0 NiA}{4\pi D^3}\sqrt{1+3\sin^2\theta} \simeq \frac{\mu_0}{2}\frac{Nia^2}{D^3} \tag{3.14}$$

where coaxial orientation of the coils has been assumed. Then the mutual inductance is found from the flux through the N linkages of the second coil as:

$$M_{12} = N\frac{\partial \Psi}{\partial i} \simeq \frac{\pi}{2} N^2 \mu_0 \frac{a^4}{D^3} \tag{3.15}$$

Once the mutual inductance is known, we can find the optimal distance between two coils with $R_1 = R_2 = R$ and operating at resonance conditions:

$$D = \left(\frac{\omega \pi N^2 \mu_0 a^4}{2\sqrt{R_S^2 - R^2}} \right)^{\frac{1}{3}} \tag{3.16}$$

We can observe a slight difference between the maximum theoretical efficiency and the efficiency obtained with FEKO in 3.2, which is caused by the approximations used to theoretically calculate B and M_{12}.

3.3.3 Maximum Power Transfer Efficiency on Bi-Conjugately Matched Systems

Conjugately matching impedances in source and load gives us the maximum achievable power transfer efficiency, which can be expressed solely in terms of mutual inductance, frequency and coil losses:

$$\eta_{max} = \frac{\omega^2 M_{12}^2 R_{L,o}}{R_1 (R_2 + R_{L,o})^2 + \omega^2 M_{12}^2 (R_2 + R_{L,o})} \tag{3.17}$$

Provided that the resonators are equal ($R_1 = R_2 = R$) then:

$$\eta_{max} = \frac{\sqrt{1 + \left(\frac{\omega M}{R}\right)^2} - 1}{\sqrt{1 + \left(\frac{\omega M}{R}\right)^2} + 1} = \frac{\sqrt{1 + S^2} - 1}{\sqrt{1 + S^2} + 1} \tag{3.18}$$

demonstrating that if impedance matching conditions are fulfilled, the efficiency of the system only depends on the equivalent resistance of the coils (radiative and ohmic losses), the mutual impedance between them and the frequency of operation. It can be observed that, to maximize efficiency, the relational factor:

$$S = \frac{\omega M}{R} \tag{3.19}$$

which is equivalent to the Coupled mode Theory K/Γ, has to be maximized. To accomplish this, it is necessary to 1) Increase the resonant frequency of the system while 2) Minimize the Coils losses and 3) Maximize the mutual inductance between coils.

3.4 Conclusions

In this chapter we have provided design guidelines to achieve maximum power transfer efficiency in terms of source and load impedances and distance between coils. The optimal values for source and load coils have been found for circuit and coupled mode theories showing complete accordance. It has been demonstrated that these values (obtained by setting the efficiency derivatives with respect to load and source equal to zero) are equivalent to applying impedance matching techniques (conjugately matching the load to the output resistance of the system and the source to the input resistance of the system). The effects of a variation of distance between coils have been analyzed and, finally, a simplified formula of maximum power transfer efficiency obtained from the previous results has been given, enumerating the required steps for its maximization.

Chapter 4

Fundamental Challenges II: Distance/Frequency Effects

Contents

4.1 Introduction

Resonant Inductive Coupling Wireless Power Transfer is a key technology to provide an efficient and harmless wireless energy channel to consumer electronics, biomedical implants and wireless sensor networks. For the practical deployability of this technology two obstacles must be overcome: effects of distance variation between transmitter and receiver (caused by a non-static transmitter/receiver) and effects of frequency drifts (system not working under resonance conditions due to a component mismatch or drifts caused by interferences). In this chapter we provide a theoretical analysis of these effects and perform a design-space exploration which allows the quantification of distance variation and frequency mismatch effects upon power transferred to the load, power transfer efficiency and transient time.

Resonant Inductive Coupling (RIC) Wireless Power Transfer could provide the means for wireless charging in consumer electronic devices, electric vehicles, robotics, wireless sensor networks, biomedical implants and fractionated spacecraft amongst others. A RIC system differs from a common inductive wireless power transfer device in the fact that the source operates at the resonant frequency of the system [26]. If the system operates off-resonance (source operates at a different frequency from resonance, or transmitter and receiver do not resonate at the same frequency) the efficiency and transmission range is significantly decreased. Also, because of this high Q resonance, RIC systems are very sensitive to distance variations, which also cause a significant decrease on the power transferred as well as the efficiency of the system.

Although wireless power transfer using resonant inductive coupling has demonstrated very high efficiencies for distance-fixed and frequency-fixed applications, there is no study that explores the practical feasibility of a wireless power transfer link under different conditions: frequency shifts due to the presence of interferent objects and impedance mismatchs due to a varying distance between transmitter and receiver.
For the practical deployability of resonant inductive coupling wireless power transfer systems in consumer electronics, it is necessary to perform a design-space exploration to assess the validity of this technology under these conditions and to be able to predict and minimize its effects.
In this chapter, we propose to analyze, through a complete design space exploration, the effects of frequency deviations and distance variations on a RIC Wireless Power Transfer System in terms of power available at the source, power transferred to the load, power transfer efficiency and power reflected back to the transmitter. Finally, transient times for a pulsed-WPT link are also analyzed taking into account these parameters.

4.2 System Description for Mismatch Analysis

Resonant inductive coupling between two electromagnetic resonators can be described by Lumped circuit theory using a coupled RLC representation system [38, 74]. In this circuit, shown in figure 4.1, the capacitances and inductances model the resonant nature of the loops while the resistors model the radiative and ohmic losses. Finally, M_{12} is the mutual inductance between transmitter and receiver, which models the fraction of EM field that is transferred between them.

In Resonant Inductive Coupling, the effect of the first coil to the second (mutual inductance M_{12}) can be represented by a compensation source Z_{2M} on the coil. Similarly, the effect of the second coil to the first one (back EMF) can be represented by a compensation source Z_{1M}. To obtain the power values at source, receiver and load, it is necessary to calculate the value of the compensation source at the receiver

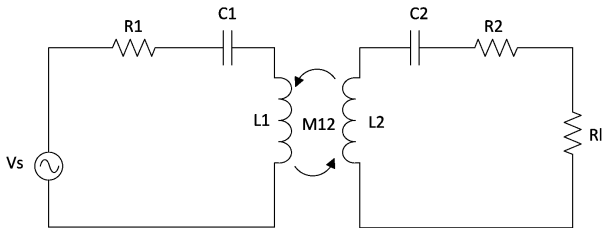

Figure 4.1: RIC System from Circuit Theory

(Z_{2M}):

$$Z_{2M} = \frac{\omega_{in} M_{12} V_{ad}}{Z_1} = \frac{\omega_{in} M_{12} V_{ad}}{R_1 + j\omega L_1 + \frac{1}{j\omega C_1}} \tag{4.1}$$

Where ω_{in} is the frequency at which the system is fed, V_{ad} is the input voltage from the source, Z_1 is the transmitter impedance in free-space and M_{12} is the mutual inductance between coils:

$$M_{12}(d) = k\sqrt{L_1 L_2} \tag{4.2}$$

Once this is known, the power at the first coil, second coil and load can be found using basic circuit theory:

$$\begin{aligned} P_1 &= \frac{V_{ad}^2}{Z_1} \\ P_2 &= I_2^2 Z_2 = \left(\frac{Z_{2M}}{Z_2 + Z_L}\right)^2 Z_2 = \left(\frac{\omega_{in} M_{12} V_{ad}}{Z_1 (Z_2 + Z_L)}\right)^2 Z_2 \\ P_L &= I_2^2 Z_L = \left(\frac{Z_{2M}}{Z_2 + Z_L}\right)^2 Z_L = \left(\frac{\omega_{in} M_{12} V_{ad}}{Z_1 (Z_2 + Z_L)}\right)^2 Z_L \end{aligned} \tag{4.3}$$

where $Z_1(\omega_{in}, \omega_{o1})$, $Z_2(\omega_{in}, \omega_{o2})$ and Z_L are transmitter coil, receiver coil and load impedances respectively.

Defining the efficiency as the ratio between the power dissipated at the load (P_L) and the total power $(P_1 + P_2 + P_L)$:

$$\begin{aligned} &\eta_{RLC}(d, \omega_{in}, \omega_{o1}, \omega_{o2}) = \\ &\frac{(\omega_{in} M_{12})^2 Z_L}{Z_1 (Z_2 + Z_L)^2 + (\omega_{in} M_{12})^2 (Z_2 + Z_L)} \end{aligned} \tag{4.4}$$

Where $M_{12}(d)$ is the mutual inductance, $Z_1(\omega_{in}, \omega_{o1})$ and $Z_2(\omega_{in}, \omega_{o2})$ are the transmitter and receiver impedances:

$$\begin{aligned} Z_1(\omega_{in}, \omega_{o1}) &= R_1 + j(\Delta\omega)\left[L_1 + \frac{1}{\omega_{o1}\omega_{in} C_1}\right] \\ Z_2(\omega_{in}, \omega_{o2}) &= R_2 + j(\Delta\omega)\left[L_2 + \frac{1}{\omega_{o2}\omega_{in} C_2}\right] \end{aligned} \tag{4.5}$$

Where $\Delta\omega$ is the difference between the input frequency ω_{in} and the resonant frequency of the coil $\omega_{o1,o2}$: $\Delta\omega = \omega_{in} - \omega_{o1,o2}$.

At resonance, source and load impedances are real, since the resonant frequency of a coil is defined as: $\omega_{oi} = 1/\sqrt{L_i C_i}$. Therefore, if the system frequency ω_{in} is the same as the resonant frequency of source coil ω_{o1} and resonant frequency of receiver coil ω_{o2} ($\omega_{in} = \omega_{o1} = \omega_{o2}$), equation 4.4 can be simplified to:

$$\eta_{RLC}(\omega_{in}, d) = \frac{(\omega_{in} M_{12})^2 R_L}{R_1(R_2 + R_L)^2 + (\omega_{in} M_{12})^2 (R_2 + R_L)} \tag{4.6}$$

and power transferred to the load is:

$$P_L(\omega_{in}, d) = \left(\frac{\omega_{in} M_{12} V_{ad}}{R_1(R_2 + R_L)} \right)^2 R_L \tag{4.7}$$

4.2.1 Maximizing Power Transferred to the Load

Maximizing the power transferred to the load means performing an impedance match between load and source coils, this is, Z_L should match the complex conjugate of the impedance the load sees (Z_{out}):

$$Z_{L,PT} = \left[j\omega L_2 - \frac{j}{\omega C_2} + R_2 + \frac{(\omega M_{12})^2}{j\omega L_1 - \frac{j}{\omega C_1} + R_1} \right]^* \tag{4.8}$$

Therefore, if the load is equal to 4.8 the power available at the receiver coil is maximized for a given distance and frequency.

4.2.2 Maximizing Efficiency

There are two equivalent methods to maximize power transfer efficiency in a RIC link: to vary the distance between transmitter and receiver until a maximum is obtained (load impedance matches the adaptation condition for maximum efficiency at a given distance) or to modify the load value to force the system work at maximum efficiency for a given distance. In this chapter, the load impedance is optimized to maximize power transfer efficiency for a given distance value. To do this, one can differentiate equation 4.4 with respect to Z_L at resonance. Obtaining:

$$R_{L,Eff} = \sqrt{R_1^2 + (\omega M_{12})^2 \frac{R_2}{R_1}} \tag{4.9}$$

Therefore, if the load resistance is equal to 4.9, the power transfer efficiency would be maximized for a given combination of frequency ($\omega_{in}, \omega_{o1}, \omega_{o2}$) and distance ($d$).

4.3 Transient Analysis

Once the circuit model of the wireless power transfer system is known, as shown in previous sections, the transient state 4th degree differential equation at the receiver

can be found by:

$$(s^2L_1C_1 + sC_1R_1 + 1)(s^2L_2C_2 + sC_2R_2 + 1 + Z_L) + s\omega^2k^2L_1L_2 = 0 \quad (4.10)$$

which, if $L_1 = L_2; C_1 = C_2; R_1 = R_2$ can be simplified to:

$$(s^2LC + sCR + 1)(Z_L + s^2LC + sCR + 1) + sk^2L = 0 \quad (4.11)$$

Which shows that the damping of the transient response depends upon the distance between transmitter and receiver, which will affect the coupling factor between transmitter and receiver ($k(d)$) and the impedance at the load (Z_L).

4.4 Methodology

The effects of distance and frequency upon power transferred to the load and power transfer efficiency are characterized using a design space exploration, where the design variables and values to explore have been normalized to the diameter of the transmitter and receiver coils where possible. To evaluate the effects of distance and frequency upon the optimal maximum efficiency or maximum power transfer impedance match conditions, two dimensions are explored: the nominal distance between transmitter and receiver (normalized to the diameter of the coils) -indicated with d_n- and the distance for which the load has been optimized (also normalized to the coil's diameter), indicated with d_L.

In this chapter, the coupling $k(d)$ and impedance $Z_1(\omega_{in}, \omega_{o1}) = Z_2(\omega_{in}, \omega_{o2})$ parameters are extracted from a Finite Element Field Solver (FEKO). The impedance and coupling are then used to find the optimal loads for maximum power transfer and maximum power transfer efficiency. Finally, all these design variables are added to a Circuit Simulation Software (SPICE) from which the steady-state and transient-state results are obtained for different nominal distance, load adaptation and frequency conditions to study the behavior of these systems and its sensitivity.

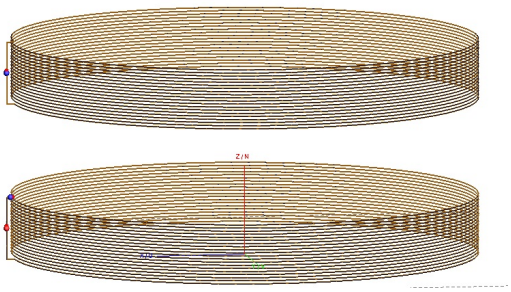

Figure 4.2: FEKO System Diagram. 2 Coils.

To benchmark the results of the exploration in this chapter, a nominal RIC model has been designed. For simplicity, transmitter and receiver antennas have

been chosen equal. Both receiver and transmitter coils were made of 0.01cm copper wire with 20 turns of 30cm diameter, illustrated in 4.2. The impedance and coupling parameters of a RIC system designed with the conditions previously described have been obtained with FEKO.

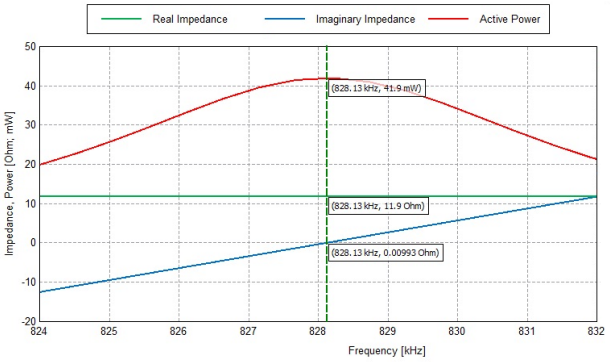

Figure 4.3: Impedance of transmitter/receiver in free-space obtained by FEKO

Figure 4.4 shows the impedance of a single coil in free-space ($Z_1 = Z_2$) from FEKO Finite Element Field Simulation, obtaining an inductance $L = 0.233mH$, a DC-resistance of $R = 11.9\Omega$ and a capacitance of $C = 0.158nF$. Therefore, the natural resonant frequency of both transmitter and receiver coils is: $f_{o1} = f_{o2} = 828.13kHz$. For simplicity, no additional capacitance to modify the resonant frequency has been added to the coils. Once the parameters of the coils are known, these can be added to SPICE, as shown in 4.4.

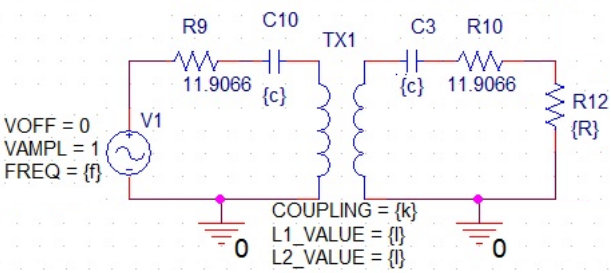

Figure 4.4: Spice Model

4.5 Distance Effects

On a Resonant Inductive Coupling Link, distance variations affect the overall efficiency as well as the power transferred to the load. Because the mutual coupling between the two coils (k) and thereby the Mutual Inductance (M_{12}) depends upon

the distance between transmitter and receiver, when distance between transmitter and receiver increases, the coupling factor between them decreases, thereby changing the output impedance that the load sees. In this section we will analyze the feasability of a Resonant Inductive Coupling Wireless Power Transfer System with variable distance. Given a fixed load, the Source Power, Load Power and Power Transfer Efficiency have been explored for different distances on a perfectly matched system for Maximum Power Transferred to the Load and on a perfectly matched system for Maximum Power Transfer Efficiency.

To evaluate the effects of distance, the coupling factor has been obtained for a distance relative to the diameter of transmitter/receiver antennas and added to the Spice model. The relationship between coupling and distance for the previously defined coils is shown in 4.5, where it can be seen that the coupling between coils decrease as the distance increases, but it is still present (less than 2.5%) at a distance of 17 times the diameter of the antennas.

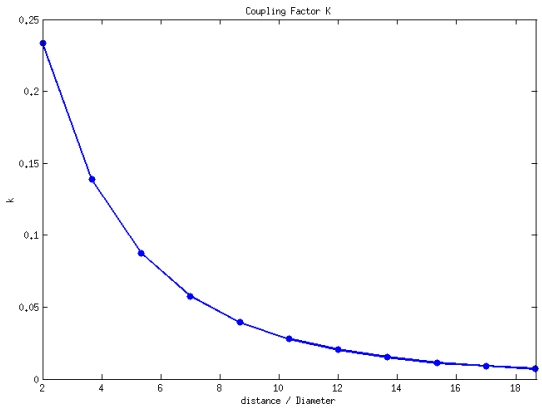

Figure 4.5: Coupling Factor dependance on distance between coils for 2 Coils of 20 turn- 30cm diameter. Obtained by FEKO.

In this section, we fisrt decouple the distance effects from the frequency mismatch effects by analyzing a perfecly frequency-matched RIC system ($f_{in} = f_{o1} = f_{o2}$). Therefore,power transferred to the load and efficiency do not depend on $\Delta\omega$, as shown in 4.6 and 4.7.

4.5.1 Maximizing Power Transferred to the Load

In this section we compare how distance variation affects a system that has been optimized for Maximum Power Transferred to the Load. The resonant frequency of the system f_o is the same as the resonant frequency of transmitter (f_1) and receiver (f_2) coils.

4.5.1.1 Source Power

Figure 4.5.1.1 shows the power available at the transmitter coil for an input voltage of: $v(t) = \sin(2\pi f_o t)$ as a function of the nominal distance factor between transmitter and receiver $d_n = d/D$ and the load adaptation factor d_a, which represents the distance factor at which the load has been optimized for.

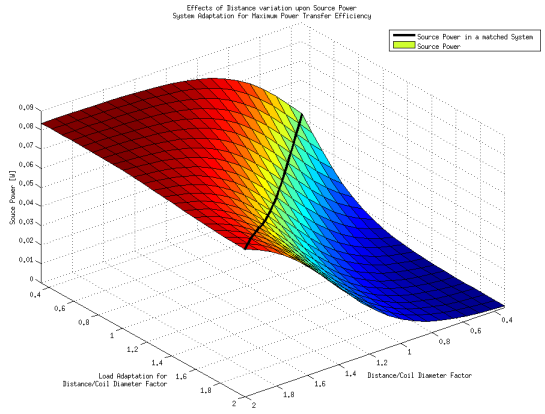

Figure 4.6: SPICE Simulation. Source Power of a system adapted for Maximum Power Transfer at resonance ($f_{in} = f_{o1} = f_{o2}$).

Figure 4.5.1.1 shows that for values very near the antenna (nominal distance d_n between transmitter and receiver smaller than half the diameter of the coils) the source power at resonance is very low. This is because the receiver coil is interferring with the first coil thereby modifying the source impedance. However, this effect is alleviated if the adaptation distance d_a is nearer the nominal distance d_n. At higher distances, the interferring effects of the second coil are negligible and the power available from the source is increased.
It can be seen that applying optimal matching conditions for maximum power transfer (black line) does not entail maximum power at the source coil.

4.5.1.2 Load Power

Figure 4.5.1.2 shows the power dissipated through the receiver coil at Z_L. Maximum power is available at the load when the load impedance matches equation 4.8 for a given Distance/Diameter factor, this is, when the adaptation distance is equal to the nominal distance (black line).

In this figure, it is possible to observe that increasing or decreasing load resistance from the optimal found in equation 4.8 (d_a higher or lower than d_n) always lowers the power received at the load for that distance, thereby showing a complete agreement between the theoretical impedance adaptation formulas given in this chapter and circuit simulations. Finally, it is important to note that the effect of a distance variation from the adaptation distance is more important when the coils are close

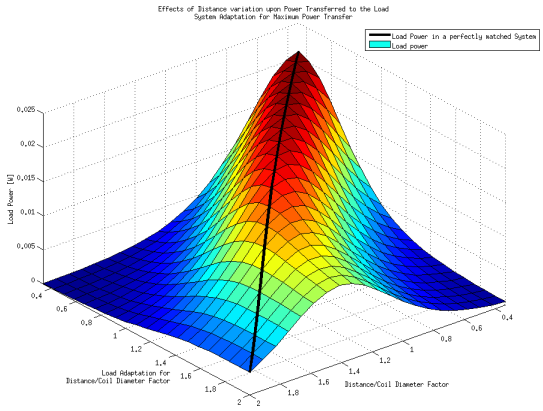

Figure 4.7: SPICE Simulation. Load Power of a system adapted for Maximum Power Transfer at resonance ($f_{in} = f_{o1} = f_{o2}$).

(since the efficiency is greater) and lower for distant coils (higher nominal distance factors).

4.5.1.3 Efficiency

Once Source and Load Power are known, we can calculate the efficiency for a RIC-system optimized for maximum power transfer as P_L/P_{in}. It is shown in figure 4.5.1.3, the efficiency of such a system for different nominal distance and adaptation distance factors. This figure shows that the efficiency is not maximum at the adaptation condition $d_n = d_a$ (black line). This is caused because matching the load to maximum power at the receiver does not entail maximum efficiency. Load adaptation for maximum power transfer can still achieve a high power transfer efficiency (between 50%-60%) for distances smaller than the diameter of the antennas but decreases very steeply for larger distances.

Uunder maximum power transfer conditions, the efficiency for distances above 1.5 times the diameter of the antenna is very low (less than 10%). However, the power transferred to the load can still be remarkable.

4.5.1.4 Transient Analysis

To perform RIC system analysis under transient conditions, a switch was added to SPICE model and the behavior of the power transferred to the load until it reached a steady-state was studied.

Figure 4.5.1.4 shows the transient state time-domain characteristic of the power transferred to the load under three different adaptation conditions: A) Adaptation distance higher than nominal distance (overcoupled system), B) Adaptation distance equal to nominal distance (critically adapted system) and C) Adaptation distance lower than nominal distance (undercoupled system).

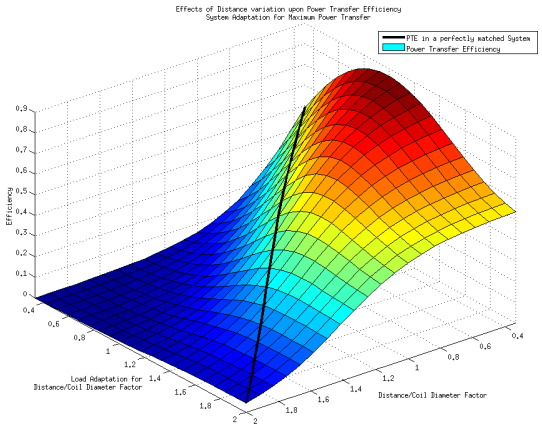

Figure 4.8: SPICE Simulation. Power Transfer Efficiency of a system adapted for Maximum Power Transfer at resonance ($f_{in} = f_{o1} = f_{o2}$).

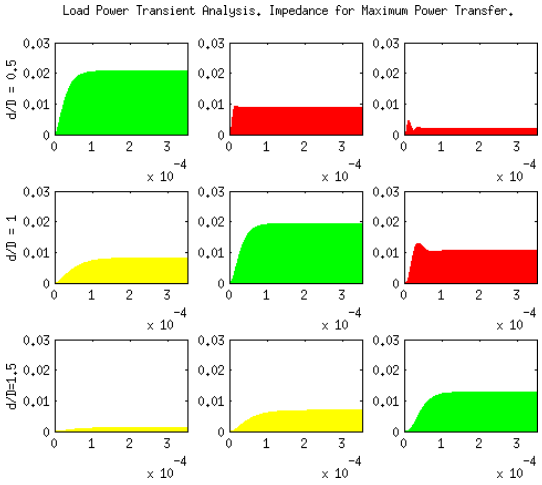

Figure 4.9: SPICE Simulation.Transient Analysis of Power Transferred to the Load under Maximum Power Transfer conditions.

To illustrate this, 4.5.1.4 shows the transient state for three different nominal distance factors $d_n = 0.5, 1, 1.5$ and three adaptation distance conditions $d_a = 0.5, 1, 1.5$. We can observe overcoupled system behaviour (load adapted for distances larger than the nominal one $d_a > d_n$ shown in red), critically coupled system behavior (load adapted for the nominal distance $d_n = d_a$, shown in green) and undercoupled system behavior (load adapted for distances lower than the nominal $d_a < d_n$).It can be seen that overcoupled (red) systems take less time to reach the steady-state but show some underdamping (larger, as the de-coupling between d_a and d_n increases). This is caused by the fact that an over-adapted system will show a frequency splited response (two peaks) as shown in figure 4.10.

Undercoupled systems do have overdamping because the frequency response ex-

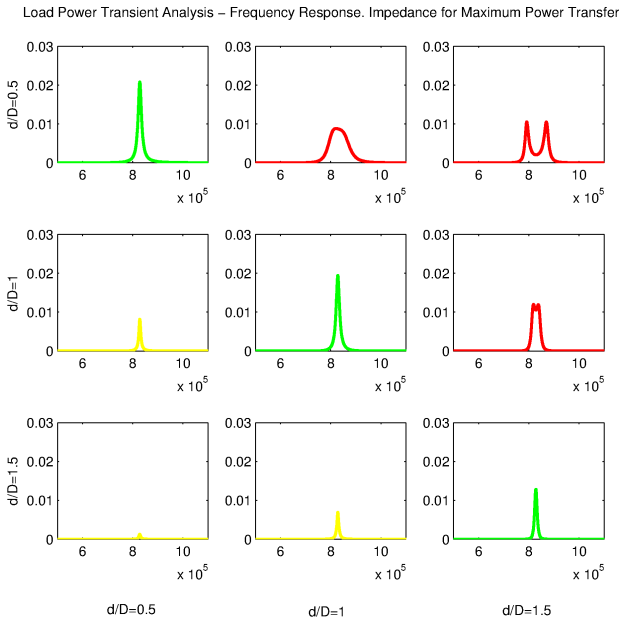

Figure 4.10: Frequency Response of an undercoupled, critically coupled and overcoupled system. Values: $d_a = 0.5d_n$, $d_a = d_n$, $d_a = 1.5d_n$ and $d_a = 2d_n$.

hibits still only one peak as shown in figure 4.10 but, since the efficiency is lower, take more time to reach the steady-state condition. Finally, critically coupled system, take less to reach the steady-state without incurring in underdamping. It is important to note that the critically damped point (point at which $\zeta = 1$) does not meet the critically coupled point for any distance between transmitter and receiver.

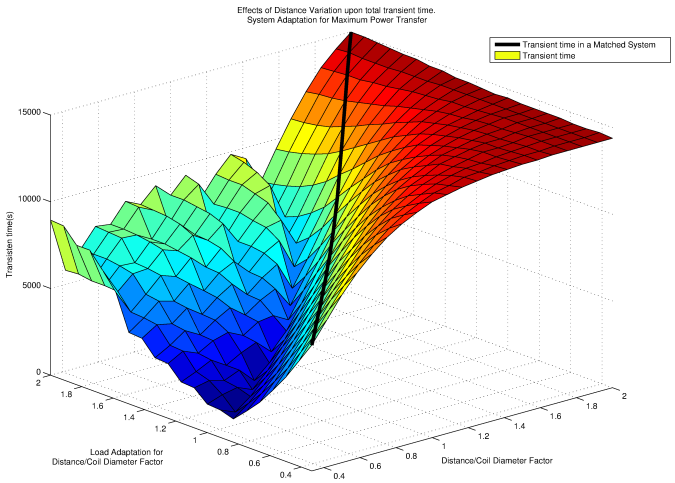

Figure 4.11: Transient times for a complete design space exploration d_a and d_n

Figure 4.5.2.4 shows the complete d_a and d_n space design exploration of transient

times in load. To calculate them, the steady-state value of power has been obtained and the transient time is the number of seconds since the switching of the source until a deviation of less than 5% of the steady-state value is obtained. As before, black line divides the figure between two parts: left of the black line is the design space which is overcoupled ($d_a > d_n$) while right is the undercoupled regime ($d_a < d_n$). We can observe here the same behavior that we explained in figure 4.10, where undercoupled systems have higher transient times (which increase when the difference between $d_n - d_a$ increases). On the other hand, overcoupled systems show also an increase in transient times which is proportional to the overcoupling ($d_a - d_n$). This is due to a higher frequency splitting (caused by increased overcoupling), which is correlated to higher transient times. Finally, it is important to note that, in systems optimized for maximum power transfer to the load, the critical damping point's line (shown in figure 4.5.2.4 as the curve created by the points with lower transient times) always corresponds to the overcoupled design space. This means that, in order to be critically damped, the system must operate in small overcoupling.

4.5.2 Maximum Efficiency

In this section we compare how a distance variation affects a resonant inductive coupling system that has been optimized for Maximum Power Transfer Efficiency between Source and Load. It is important to note that, in this section, when we refer to the distance adaptation d_a it is for maximum power transfer efficiency, which is different from the distance adaptation for maximum power transfer shown in previous section.

4.5.2.1 Source Power

Figure 4.5.2.1 shows the power available at the source coil. For a system optimized to maximize its power transfer efficiency, the power source at the critical adaptation point decreases steeply with distance. This is because in order to still achieve an efficient transmission, the power available from the source must be very small due to the interferences between transmitter and receiver coil impedance explained before.

Similarly to the system optimized for maximum power transfer, the maximum power available at the source is not related to the optimal adaptation factor $d_n = d_a$.

4.5.2.2 Load Power

In a system optimized for maximum efficiency, the power transferred to the load in an optimally matched system (nominal distance equal to nominal adaptation factor) is not maximum.

Figure 4.5.2.2 shows that for high nominal distance factors (above 1.5 times the diameter of the transmitter/receiver coils) the power transferred to the load is very low. Similarly, for very small nominal distance factors (less than 0.5 times the diameter of the transsmitter/receiver antennas) the power that is transferred to the load is also decreased.

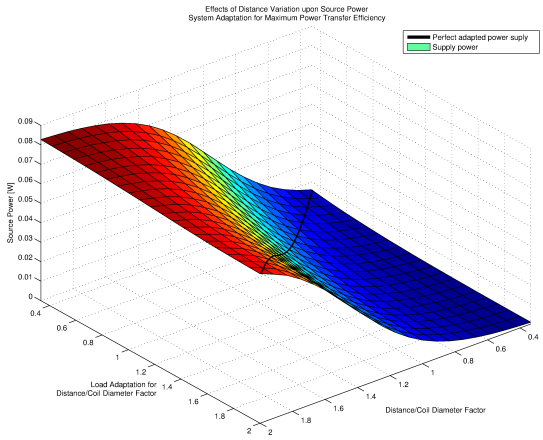

Figure 4.12: SPICE Simulation. Source Power of a system adapted for Maximum Efficiency at resonance ($f_{in} = f_{o1} = f_{o2}$).

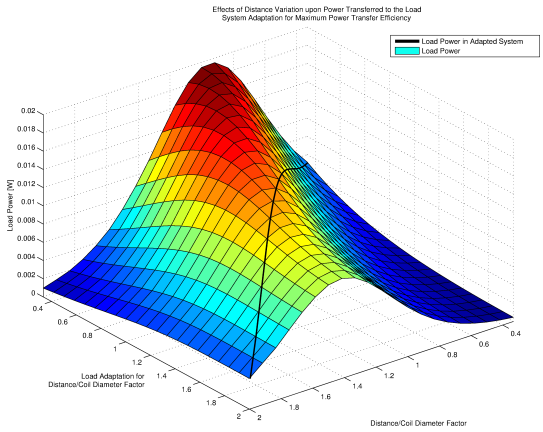

Figure 4.13: SPICE Simulation. Load Power of a system adapted for Maximum Efficiency at resonance ($f_{in} = f_{o1} = f_{o2}$).

4.5.2.3 Efficiency

Power Transfer Efficiency between source and load is shown for a RIC system with maximum efficiency adaptation in figure 4.5.2.3. It can be seen that under optimal adaptation conditions ($d_n = d_a$) the efficiency is maximum for that nominal distance d_n.

4.5.2.4 Transient Analysis

Similarly to previous section, system analysis under transient conditions is performed but for a Maximum Efficiency System. Figure 4.5.2.4 shows the transient state time-domain characteristic of the power transferred to the load under three dif-

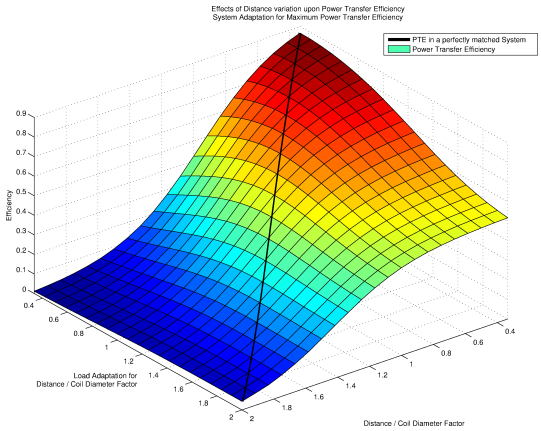

Figure 4.14: SPICE Simulation. Efficiency of a system adapted for Maximum Efficiency at resonance ($f_{in} = f_{o1} = f_{o2}$).

ferent adaptation conditions: A) Adaptation distance higher than nominal distance (overcoupled system), B) Adaptation distance equal to nominal distance (critically adapted system) and C) Adaptation distance lower than nominal distance (undercoupled system).

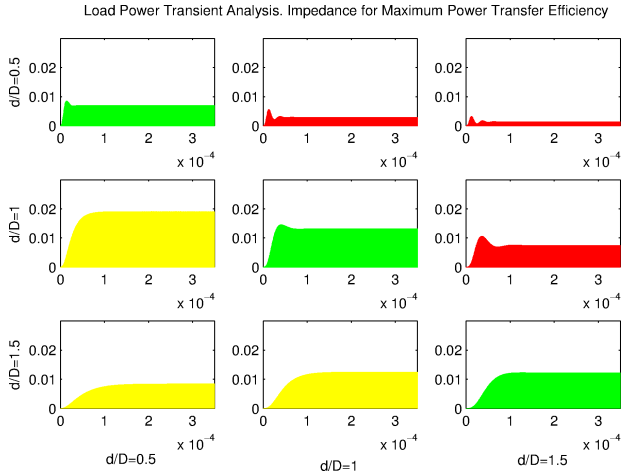

Figure 4.15: SPICE Simulation. Transient Analysis of Power Transferred to the Load under Maximum Efficiency Conditions

To illustrate this, 4.5.2.4 shows the transient state for three different nominal distance factors $d_n = 0.5, 1, 1.5$ and three adaptation distance conditions $d_a = 0.5, 1, 1.5$. The three diagrams in yellow correspond to the transient response when system is underadapted ($d_a < d_n$), this is $Z_L < Z_{L,o}$, green correspond to a critically adapted system for maximum efficiency $d_a = d_n$, and red corresponds to over-adapted systems ($d_a > d_n$). It is important to note that, in this case, both

the critically adapted and over-adapted states show underdamping in the transient response, meaning that in order to avoid underdamping the system must operate in under-adaptation states. This agrees with the results shown in 4.5.2.4 where the frequency response of the same is shown. Shown in red, the conditions at which the system presents two frequency peaks (overcoupled systems showing underdamping). In green, the states that are nearer the critically damping points (this is, there is only one peak of frequency and the response is high) and in yellow the overdamped points (only one peak but the response is small, which means that it will take more time to reach the steady-state condition).

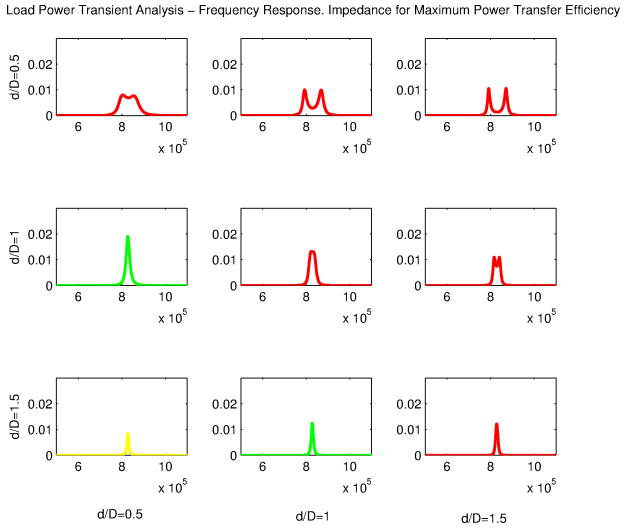

Figure 4.16: Frequency Response of an undercoupled, cricitally coupled and over-coupled system. Values: $d_a = 0.5d_n$, $d_a = d_n$, $d_a = 1.5d_n$ and $d_a = 2d_n$.

Finally, it is important to note that, when the system is underdamped, the bandwidth between the two frequency peaks ($\Delta f = f_2 - f_1$) increases. Therefore, when a system is overcoupled, the more overcoupled it is, the more frequency splitting will be obtained and the more time it will take for the system to reach a steady-state condition.

The behavior explained above is illustrated in figure 4.5.2.4, where the transient times have been measured as the number of seconds since the switching of the source until a deviation of less than 5% of the steady-state value is obtained.

In this figure, the critically adaptation condition for maximum power transfer efficiency is shown (black line) and the transient times obtained for the full design-space exploration are shown. It can be seen that, in this case, the critically damped curve (curve made of the points with lower transient times for each nominal distance and adaptation factor) corresponds to an under-adapted system for small distances (right of the black line) and over-adapted system for large distance factors (left of the black line). This means that there is a point at which the system is critically damped and critically coupled for maximum power transfer efficiency at the same

time. This point corresponds to a distance factor of 2 times the diameter of the antennas. It can be seen that in an over-adapted system, as the frequency splitting

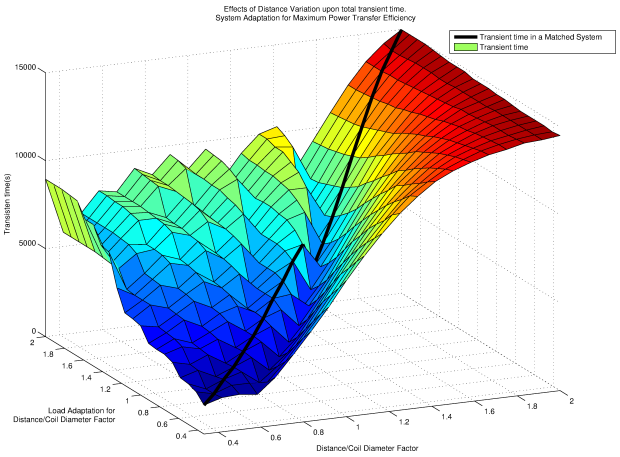

Figure 4.17: Transient times showing complete design space exploration d_a and d_n

seen in 4.5.2.4 increases, the transient times increase too. Finally, it is important to note that in an over-damped system (right of the critically damped curve) the transient times increase proportionally to the the distance factor between transmitter and receiver. For very over-damped systems (distance factors higher than 2) the adaptation factor stops intervening on the transient time.

4.6 Frequency Mismatch Effects

Frequency mismatch effects can either occur at the transmitter side ($f_{in} = f_{o2} \neq f_{o1}$), at the receiver side ($f_{in} = f_{o1} \neq f_{o2}$) or at both ($f_{in} \neq f_{o1} = f_{o2}$). On the next sections the effects of mismatch effects at both the transmitter and receiver sides are explored analyzing its effect upon Source Power, Power received at load, Power Transfer Efficiency and Transient State delays. The distance between transmitter and receiver is normalized with respect to the Coil Diameter (distance / diameter) and the actual resonant frequency deviation (f'_{ox}) is normalized with respect to the optimal resonant frequency ($f_{ox} = f_o$): f'_{ox}/f_{ox}).

4.6.1 Transmitter Resonant Frequency Deviation

This section explores the behavior of the wireless resonant inductive coupled link when the transmitter resonant frequency deviates from the optimal conditions $f'_{o1} \neq f_{o1}$, considering f_{o1} the frequency at which both the input source and the receiver operate $f_{o1} = f_{o2} = f_{in}$. Figure 4.6.1 shows the power available from the source for a a normalized transmitter resonant frequency deviation f'_{o1}/f_{o1}. It can be seen that the available source power is very sensitive to transmitter frequency deviations from the resonant frequency $f_{o1} \neq f_o = f_{o2}$ due to the high Q factor of

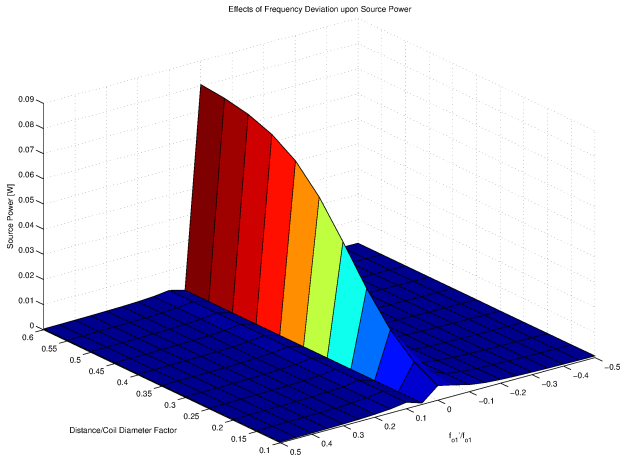

Figure 4.18: Source Power Available after a transmitter resonant frequency deviation

the transmitter, meaning that a very small variation of less than 5% could cause the power available from the source to decrease drastically. Figure 4.6.1 shows the power received at load with respect to the transmitter resonant frequency deviation. Since the power received at load is dependant upon the power available from the source, the same behavior is shown when the transmitter resonant frequency deviates from the optimal condition $\Delta f/f_{o1} = 0$.

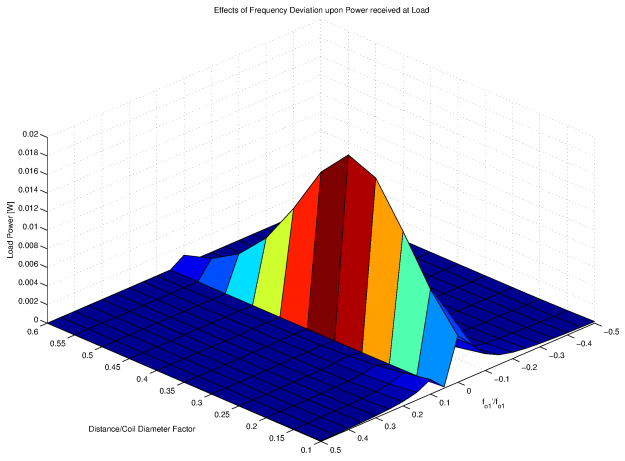

Figure 4.19: Load Power Available after a transmitter resonant frequency deviation

Finally, 4.6.1 shows the resulting power transfer efficiency in the same situation.

It can be seen that the power transfer efficiency is not as affected by the transmitter resonant frequency deviation as the power received by the load. This is inherent to equation 4.4 where it can be seen that the power transfer efficiency depends upon the transmitter resonant frequency deviation, which is included in $Z_1(\omega_{in}, \omega_{o1})$.

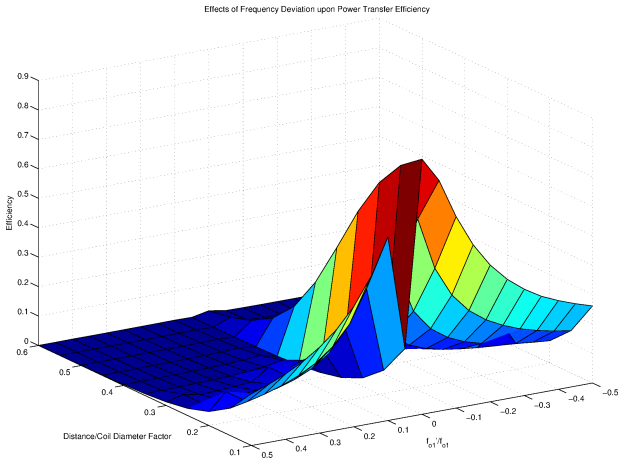

Figure 4.20: Power Transfer Efficiency after a transmitter resonant frequency deviation

4.6.2 Receiver Resonant Frequency Deviation

In this section, the source power, load power and power transfer efficiency for a RIC link with a receiver resonant frequency deviation ($f'_{o2} \neq f_{o2}$) is shown , being f_{o2} the optimal resonant frequency of the receiver ($f_{o2} = f_{o1} = f_o$). The source power available after a receiver frequency deviation is shown in Figure 4.6.2. It can be seen that a variation on the receiver resonant frequency only affects the available source power in the sense that the reflected impedance back from secondary coil is modified by this frequency deviation.

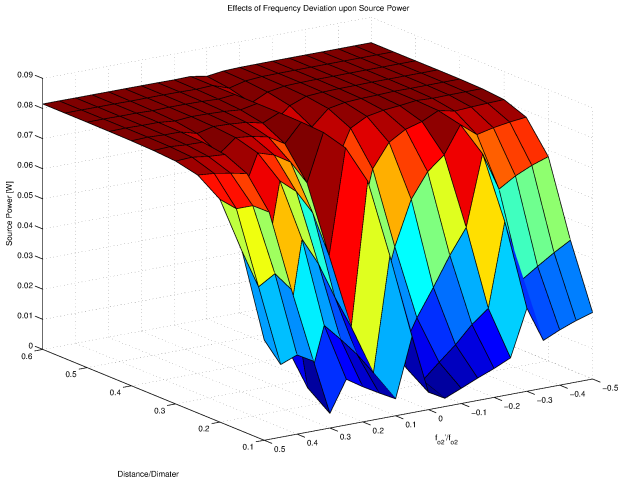

Figure 4.21: Source Power Available after a receiver resonant frequency deviation

Figure 4.6.2 shows the power received at load with respect to the receiver resonant frequency deviation. In this case, the power transfer efficiency is strongly

affected by the receiver resonant frequency, thereby modifying the received power at load.

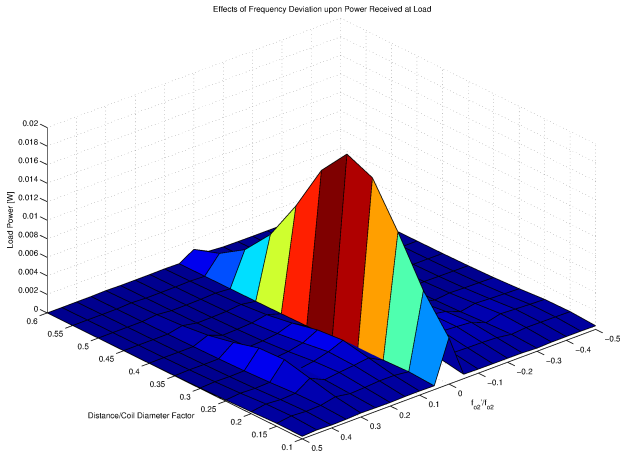

Figure 4.22: Load Power Available after a receiver resonant frequency deviation

Figure 4.6.2 shows the behavior of Power Transfer Efficiency for receiver frequency deviation f'_{o2}. Inspecting equation 4.4 it can be observed that the efficiency is proportional to $Z_2(\omega_{in}, \omega_{o2})$.

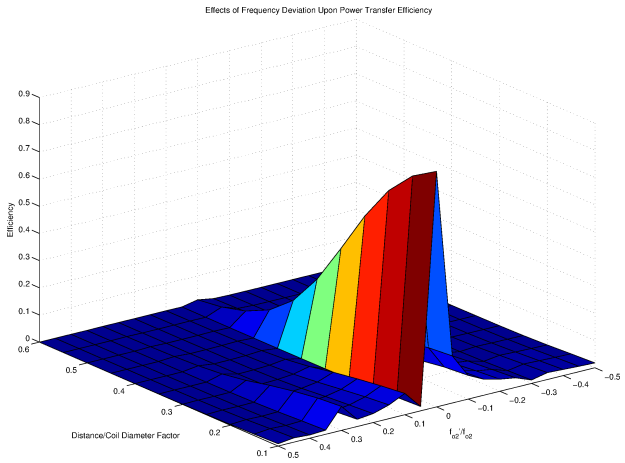

Figure 4.23: Power Transfer Efficiency after a receiver resonant frequency deviation

4.6.3 Input Power Frequency Deviation

In this section, a system with both transmitter and receiver working at a given resonant frequency ($f_{o1} = f_{o2} = f_o$) is powered by a source at a different frequency ($f_{in} \neq f_o$). The effects of this frequency deviation $\Delta f_{in} = (f_{in} - f_o)/f_o$ are shown below. Figure 4.6.3 shows the frequency response of the power available from the

source upon different distance factors. It can be seen that for distances very close to the transmitter, the frequency response is splitted in two resonant frequencies, due to an overcoupling in the receiver.

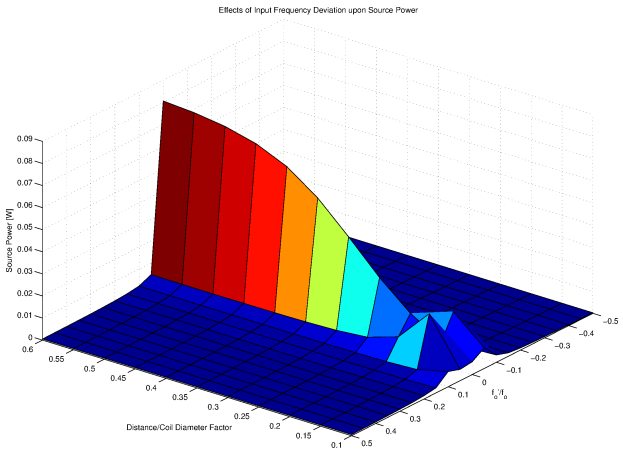

Figure 4.24: Source Power Available after an input frequency deviation

Figure 4.6.3 shows the available power at the receiver when the source power frequency does not match the resonant frequency of the system (resonant transmitter and receiver frequency). In this figure, the behavior of the power received at the load over different distances is shown for the three different conditions conidered in previous sections: overcoupling (distances close to the transmitter, two peaks and maximum not at $\Delta f_{in} = 0$), critical coupling (maximum power transferred to the load, one peak at $f_{in} = f_o$) and undercoupling (one peak at $f_{in} = f_o$ but power transferred to the load is not maximized).

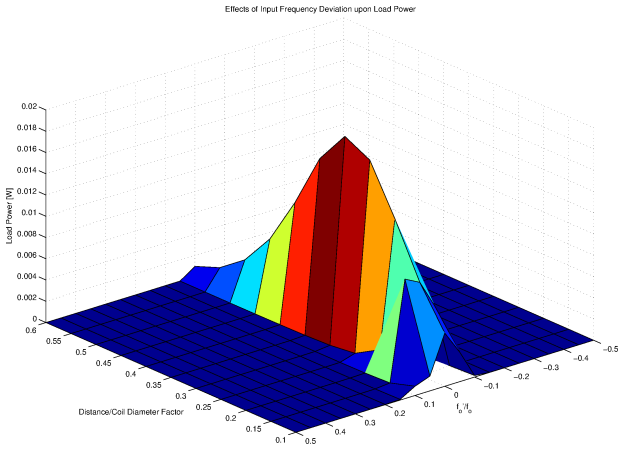

Figure 4.25: Load Power Available after a receiver resonant frequency deviation

Finally, figure 4.6.3 shows the efficiency curve obtained by dividing the power

received at load by the power available from the source. In this figure, the effects of the input frequency deviation are shown demonstrating that, although the power transferred to the load is maximized at a given distance, the power transfer efficiency is not. In any case, the maximum power transfer efficiency is always obtained at a 0 frequency deviation ($f_{in} = f_o$).

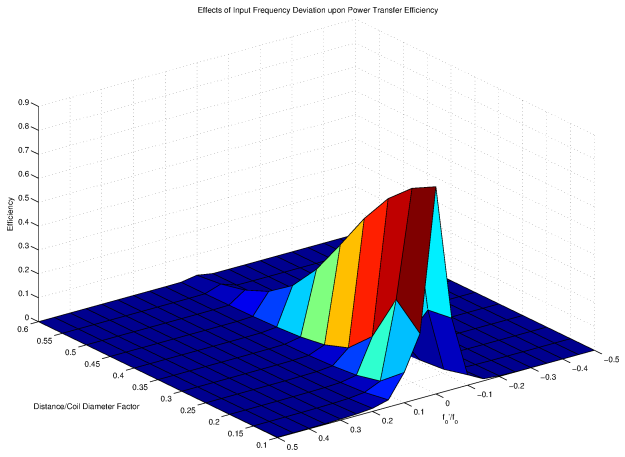

Figure 4.26: Power Transfer Efficiency after a receiver resonant frequency deviation

4.6.4 Transmitter and Receiver Frequency Deviation

Finally, the effects of a frequency deviation in both the transmitter ($\Delta f_1/f_o \neq 0$) and the receiver ($\Delta f_2/f_o \neq 0$) are shown for a set of six different distances (normalized to the diameter of the antennas). No impedance adaptation has been performed neither to counteract the distance effects nor the frequency-deviation effects.

Figure 4.6.4 shows the effects of a transmitter and receiver frequency deviation upon the transferred source power. It can be seen that a transmitter frequency deviation affects very significatively the available power at the source. On the other hand, a receiver frequency deviation only affects the source power available if transmitter and receiver are in close proximity (the reflected impedance of the receiver modifies the transmitter behavior). If transmitter and receiver are at a distance higher than 1.5 diameter of the antennas, the effect of a receiver frequency mismatch becomes negligible. This is due to a low coupling between transmitter and receiver at these distances. Finally, it is important to note that the available source power at the transmitter is low when the proximity between transmitter and receiver is high. This is caused by the overcoupling between both coils in close proximity, which was analyzed in 4.5.1.1. If the frequency at either the transmitter or the receiver deviates from resonance, the coupling between coils is decreased, which reduces the overcoupling effect.

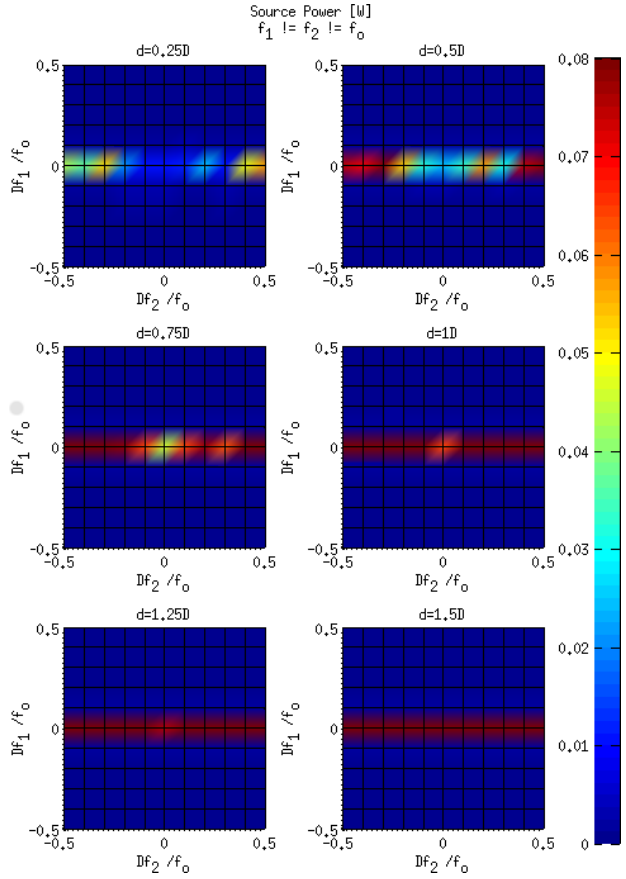

Figure 4.27: Source Power Available after a transmitter and receiver resonant frequency deviation

Figure 4.6.4 illustrates the power received by the second coil when both transmitter and receiver have a different resonant frequency than the operating frequency. Unlike the power source, the load power is greatly affected by both the transmitter and the receiver frequency deviations. In this case, more power is received depending on a) the source power available (which is strongly affected by Δf_1) and b) the efficiency of the transmission (which is affected by Δf_2 when coupling between both coils is high). Therefore, the effects of a deviation of the transmitter and receiver frequencies are visible in this figure.

Finally, figure 4.6.4 shows the power transfer efficiency. In this case, the effects of Δf_2 and Δf_1 are very noticeable for high power transfer efficiencies (near-range between transmitter and receiver). It is important to note that while Source Power is more affected by a transmitter frequency deviation, the power transfer efficiency is more affected by a receiver frequency deviation. This is due to the fact that, while the source can be transmitting a low power level due to a mismatch between input frequency and transmitter frequency, the receiver can still receive the magnetic field if the coils are in close proximity. This is due to an overcoupling between transmitter

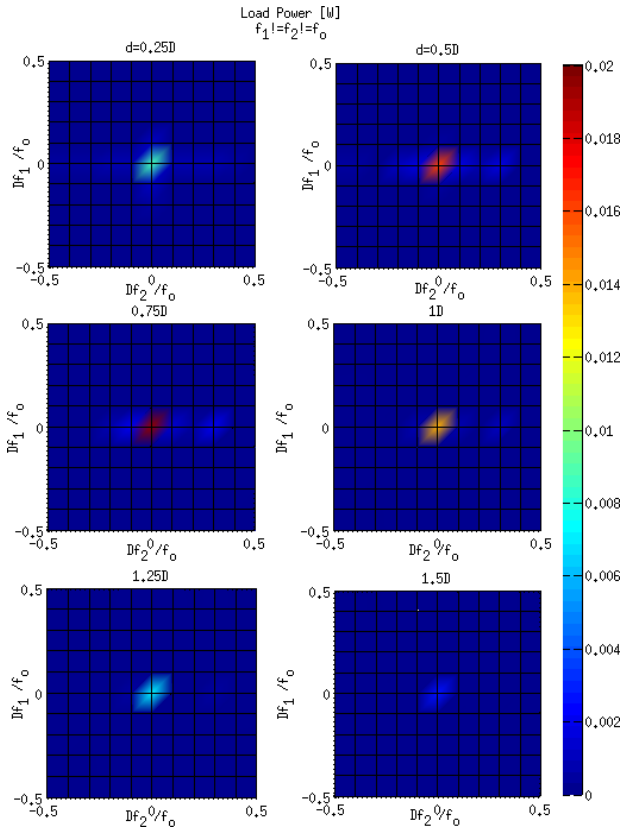

Figure 4.28: Load Power Available after a transmitter and receiver resonant frequency deviation

and receiver that can result in a higher bandwidth. When the distance between transmitter and receiver is higher than 1.5 times the diameter of the antennas, power transfer is only achieved at the resonant frequency condition $f_1 = f_2 = f_o$.

4.7 Conclusions

In this chapter, the effects of distance and frequency variations upon a resonant inductive coupling wireless power transfer system have been studied. A complete design-space exploration has been developed to characterize the effects of variable distances between transmitter and receiver, normalized to the antenna diameters and resonant frequency respectively. Guidelines to adapt the impedance of transmitter and receiver antennas in order to maximize power transfer efficiency or power received at load have been proposed and its effect to the transient behavior has been studied.

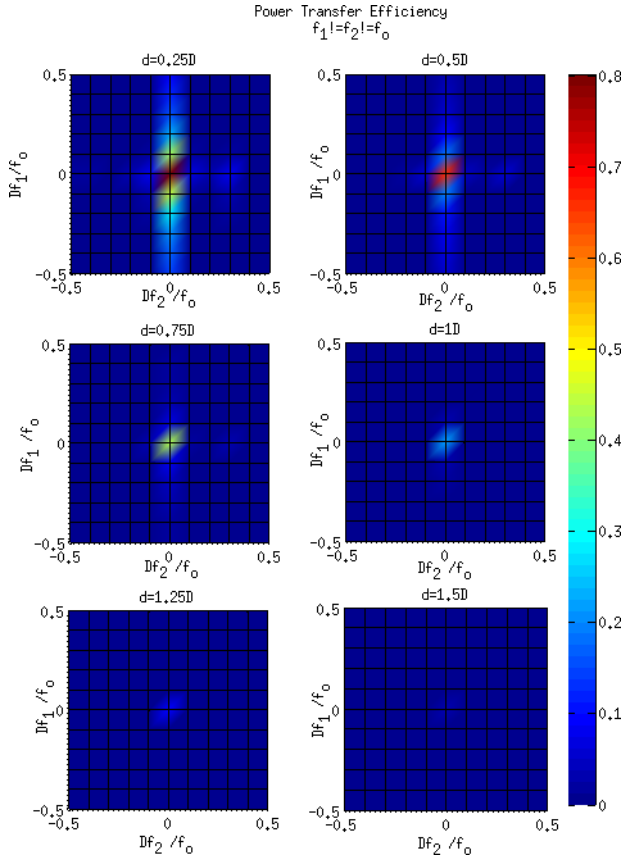

Figure 4.29: Power Transfer Efficiency after a transmitter and receiver resonant frequency deviation

Chapter 5

Fundamental Challenges III: Interfering Objects & Relaying Effects

Contents

5.1 Introduction

Resonant Inductive Coupling Wireless Power Transfer (RIC-WPT) is foreseen as a key technology to wirelessly charge the next generation of consumer electronics, biomedical implants, electronic vehicles and the internet of things. These WPT scenarios coincide on the fact that all of them are deployments where foreign objects (internal to the system or external) are very common. In this chapter we analyze the effects of Interfering Objects (sec. 5.2) first from the EM perspective [40], by proposing a complete behavioral model and characterization of its detrimental effects. Secondly, we'll analyze the potential benefits of Relaying Effects (sec. 5.3) that could be obtained by leveraging the cross-coupling effect of internal or foreign interfering objects on MIMO scenarios [78, 56].

5.2 Interfering Objects on RIC-WPT

This section is devoted to propose a circuit-based analytical model that predicts the behavior of a RIC-WPT link in the presence of foreign objects, together with a design-space exploration (both analytical and EM-based) of its effects.

A RIC system differs from a common inductive WPT device in the fact that the source operates at the resonant frequency of the coupled resonator [26] thereby allowing an extended range. Because of this resonance, RIC systems are very sensitive to distance variations and to conductive foreign objects. While the effects of distance variation between transmitter and receiver and the relationship between them and impedance matching techniques have already been addressed in chapters 3 and 4, the effects of foreign objects are considered the second fundamental challenge of RIC-WPT.

5.2.1 Analytical Model of Interfering Objects

5.2.1.1 Problem Statement

When exploring the effects of an interference, the first element to address is how to model the foreign object, which needs to be modeled from both its electric and magnetic behavior.

All conductive materials have, beyond the natural DC resistance, a frequency-dependant electrical impedance model in the frequency band of interest, as a result of the AC skin effect [79], which is the tendency for high-frequency alternating currents and magnetic flux to penetrate into the surface of a conductor to a limited depth. The penetrating depth depends on the frequency and the properties of the conductivity and permeability of the material and models the impedance of the object caused by the skin effect [80]. Therefore, with regards to the electric behavior of the foreign object, any conductive material can be replaced by an equivalent impedance circuit with the same frequency-response characteristic. The impedance-frequency characteristic of the foreign object is determined by the object geometry, size and material.

Regarding the magnetic behavior, the coupling factor, which models the amount of the field that is effectively transferred between the foreign object and the transmitter and receiver coils (k_{i1},k_{i2}) and between transmitter/receiver coils and the foreign object (k_{1i}, k_{2i}) respectively (see fig. 5.1) should be included too. These coupling factors together with the impedance response of the foreign object (its resonant frequency and resistance) will define how much the foreign object affects the RIC-WPT link.

In this chapter, the foreign object has been simplified and replaced by an equivalent RLC circuit, which models the electrical behavior of the natural resonance of the component. The equivalent RLC circuit used has therefore a given resistance

(depending on the conductivity of the material), an inductance (which depends on the geometry and structure of the object) and a capacitance (to force the first resonance). The effects of this circuit upon the resonant inductive wireless link will depend on its magnetic coupling to the different entities of the link: transmitter (k_{i1}, k_{1i}) and receiver (k_{i2}, k_{2i}).

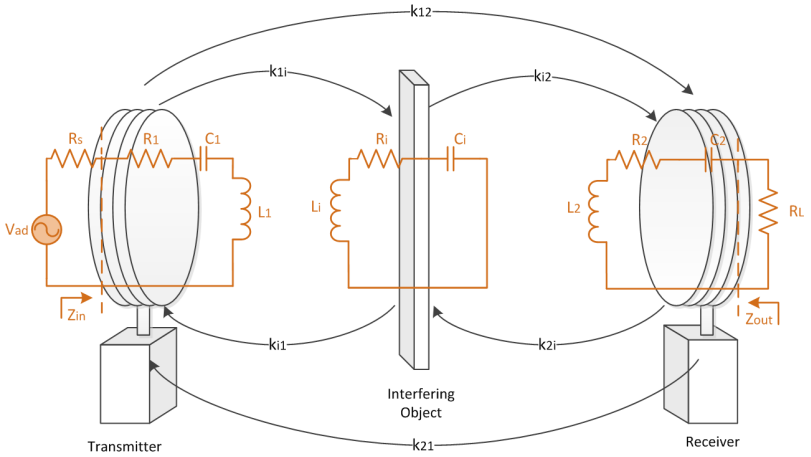

Figure 5.1: Circuit Diagram of the RIC System incorporating a foreign object.

In Figure 5.1 the resulting circuit diagram of a RIC system consisting of a transmitter resonator (R_1, L_1, C_1), a receiver resonator (R_2, L_2, C_2) and the foreign object (L_i, R_i and C_i) is shown. The transmitter is coupled to the receiver and foreign object by k_{12} and k_{1i} respectively. Similarly, the transmitter is coupled to the transmitter and the foreign object by k_{21} and k_{2i}. Finally, the interference is coupled to the transmitter and receiver resonators through k_{i1}, k_{i2}. L_i, R_i and C_i correspond to the foreign object inductance, resistance and capacitance, which altogether constitute the simplified RLC model of the foreign object.

Despite this simplified model at resonance is of general purpose for a wide range of geometries, in this chapter, a square metallic plane will be used to illustrate the effects of a foreign object in the vicinity of the RIC-WPT link. The impedance/frequency response of this object with a variable size ($0.01m^2$, $0.03m^2$, $0.09m^2$ and $0.16m^2$) obtained by a Finite Element Field Solver (FEKO) is shown in Figure 5.2, where it can be seen that both the natural resonant frequency and the impedance around resonance depend upon the size of the foreign object and that multiple resonances are exhibited.

5.2.1.2 Model

The block diagram of the wireless power transfer system including the foreign object described in figure 5.1 is shown in figure 5.3, defining the interrelationships between the input source (V_{ad}), the transmitter (1), the receiver (2) and the foreign object (i). V_A and V_B represent the contributions to V_1 from the foreign object and the receiver

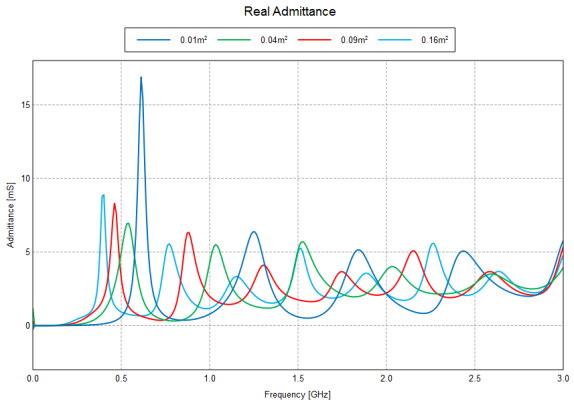

Figure 5.2: Frequency Response of a variable size metallic plane obtained by FEKO.

respectively. G_1,G_2 and G_i are the transfer functions of transmitter, receiver and

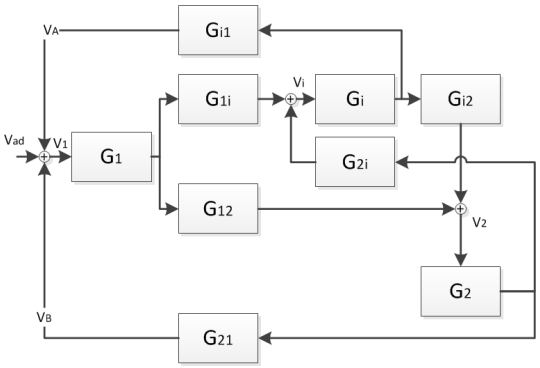

Figure 5.3: Simplified Model Diagram of the Interfering Object coupled to Transmitter and Receiver

foreign object respectively:

$$G_{1,2,i} = \frac{I_{1,2,i}}{V_{1,2,i}} = \frac{j\omega C_{1,2,i}}{1 + j\omega C_{1,2,i} R_{1,2,i} - \omega^2 L_{1,2,i} C_{1,2,i}} \tag{5.1}$$

where ω is the frequency at which the system operates, ω_1, ω_2 and ω_i are the resonant frequencies of transmitter, receiver and foreign object respectively, defined as the frequencies at which the impedance is real. G_{1i},G_{i1},G_{2i},G_{i2} are defined as the transfer functions from the transmitter/receiver to foreign object and from the foreign object to transmitter/receiver, governing the distribution of power that reaches the transmitter and receiver from the foreign object and the other way around. Finally, G_{12},G_{21} represent the power coupled directly from transmitter to receiver and

from receiver to transmitter respectively.

$$\begin{aligned} G_{1i} &= (\omega k_{1i}\sqrt{L_1 L_i})^2; \quad G_{2i} = (\omega k_{2i}\sqrt{L_2 L_i})^2 \\ G_{i1} &= (\omega k_{i1}\sqrt{L_i L_1})^2; \quad G_{i2} = (\omega k_{i2}\sqrt{L_i L_2})^2 \\ G_{12} &= (\omega k_{12}\sqrt{L_1 L_2})^2; \quad G_{21} = (\omega k_{21}\sqrt{L_2 L_1})^2 \end{aligned} \tag{5.2}$$

The equations for the voltage at the transmitter, current at the receiver and current at the foreign object can be derived from figure 5.3:

$$\begin{aligned} V_1 &= V_{ad} + I_i G_{i1} + I_2 G_{21} \\ I_1 &= V_1 G_1 \\ I_i &= (I_1 G_{1i} + I_2 G_{2i}) G_i \\ I_2 &= (I_1 G_{12} + I_i G_{i2}) G_2 \end{aligned} \tag{5.3}$$

Solving this system of equations yields the output current at the receiver:

$$I_2 = I_1 \frac{G_2 G_{12} + G_i G_2 G_{1i} G_{i2}}{1 + G_i G_2 G_{2i} G_{i2}} \tag{5.4}$$

the current at the foreign object:

$$I_i = I_1 \frac{G_i G_{1i} + G_i G_2 G_{12} G_{2i}}{1 + G_i G_2 G_{2i} G_{i2}} \tag{5.5}$$

and finally, the source current I_1:

$$\begin{aligned} I_1 &= V_{ad} \frac{G_1}{1 + G_1 G_{i1} C_1 + G_1 G_{21} C_2} \\ C_1 &= \frac{G_i G_{1i} + G_i G_2 G_{12} G_{2i}}{1 + G_i G_2 G_{2i} G_{i2}} \\ C_2 &= \frac{G_2 G_{12} + G_i G_2 G_{1i} G_{i2}}{1 + G_i G_2 G_{2i} G_{i2}} \end{aligned} \tag{5.6}$$

as well as the input impedance, defined as $Z_{in} = V_{ad}/I_1$:

$$\begin{aligned} Z_{in} = \frac{1}{G_1} &+ G_{1i}\left(\frac{G_i G_{1i} + G_i G_2 G_{12} G_{2i}}{1 + G_i G_2 G_{2i} G_{i2}}\right) \\ &+ G_{21}\left(\frac{G_2 G_{12} + G_i G - 2 G_{1i} G_{i2}}{1 + G_i G_2 G_{2i} G_{i2}}\right) \end{aligned} \tag{5.7}$$

The power dissipated in the first coil (transmitter), the power dissipated in the second coil (receiver), the power transferred to the load and the power lost due to coupling to the interferring object are defined as:

$$\begin{aligned} P_1 &= \frac{|I_1|^2}{2} R_1; \qquad P_2 = \frac{|I_2|^2}{2} R_2 \\ P_L &= \frac{|I_2|^2}{2} R_L; \qquad P_i = \frac{|I_i|^2}{2} R_i \end{aligned} \tag{5.8}$$

where R_1, R_2, R_L and R_i are the real part of Z_1, Z_2, Z_L and Z_i respectively.
Once the power dissipated and transferred are known, the efficiency, defined as the power transferred to the load divided by the total power of the system, is found as

$$\eta = \frac{P_L}{P_1 + P_2 + P_L + P_i} \tag{5.9}$$

5.2.1.3 Particular Case 1: Interfering Object only coupled to Transmitter

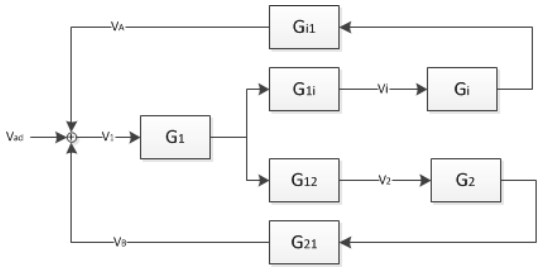

Figure 5.4: Simplified Model Diagram - Interfering object coupled to Transmitter

The model described above represents a generic system where all the coils are coupled among them. However, depending on the position of the foreign object, the coil can be modelled to be either coupled only to the transmitter or to the receiver. In this section we will analyze a particular, simplified but representative system where the foreign object is coupled only to the transmitter coil ($k_{1i} \neq 0$, $k_{i1} \neq 0$, $k_{i2} = k_{2i} = 0$). In this case, $G_{i2} = G_{2i} = 0$ and the equations defined in 5.3 can be simplified to:

$$\begin{aligned} V_1 &= V_{ad} + I_i G_{i1} + I_2 G_{21}; \qquad I_1 = V_1 G_1 \\ I_i &= (I_1 G_{1i}) G_i; \qquad I_2 = (I_1 G_{12}) G_2 \end{aligned} \tag{5.10}$$

Solving the system of equations, the current flowing through the transmitter coil I_1 can be obtained as:

$$I_1 = \frac{V_{ad} G_1}{1 + G_1 G_i G_{1i} G_{i1} + G_1 G_2 G_{21} G_{12}} \tag{5.11}$$

And the input impedance of the system is given by:

$$\begin{aligned} Z_{in} = \frac{1}{G_1} + G_i G_{1i} G_{i1} + G_2 G_{12} G_{21} = \\ Z_1 + \frac{(\omega M_{1i})^2}{Z_i} + \frac{(\omega M_{12})^2}{Z_2} \end{aligned} \tag{5.12}$$

where Z_1, Z_i and Z_2 are the impedances of the transmitter coil, interference and receiver coil respectively. M_{1i} is the mutual inductance between transmitter and interference $M_{1i} = k_{1i}\sqrt{L_1 L_i}$ and M_{12} is the mutual inductance between

transmitter and receiver coils $M_{12} = k_{12}\sqrt{L_1 L_2}$.

From equation 5.12 it can be observed that the input impedance of a foreign object coupled only to the transmitter is the same as the impedance of a system without the foreign object but adding an $(\omega M_{1i})^2/Z_i$ factor. Therefore, this simplified model can be analyzed as a system without any interference but with a modified input impedance caused by the presence of the foreign object. Using this result, the current circulating through the first coil, second coil and interference can be re-written as:

$$\begin{aligned} I_1 &= \frac{V_{ad}}{Z_{in}} = \frac{V_{ad}}{Z_1 + \frac{(\omega M_{1i})^2}{Z_i} + \frac{(\omega M_{12})^2}{Z_2 + R_L}} \\ I_2 &= I_1 \frac{\omega M_{12}}{Z_2 + R_L}; \qquad I_i = I_1 \frac{\omega M_{1i}}{Z_i} \end{aligned} \tag{5.13}$$

This is relevant since the fact that only the input impedance is modified implies that the source coil will have a different frequency response due to the foreign object, but not the receiver coil. Therefore, if the foreign object deviates the transmitter from resonance, the receiver will not be deviated from resonance and the effect of the foreign object will be more significant. Finally, taking into account the new current expressions, the power transfer efficiency defined as P_L/P_{in} can be simplified to:

$$\eta = \frac{(\omega M_{12})^2 Z_L Z_i}{Z_1 (Z_2 + R_L)^2 Z_i + (\omega M_{12})^2 (Z_2 + R_L) Z_i + (\omega M_{1i})^2} \tag{5.14}$$

5.2.1.4 Particular Case 2: Interfering Object only coupled to Receiver

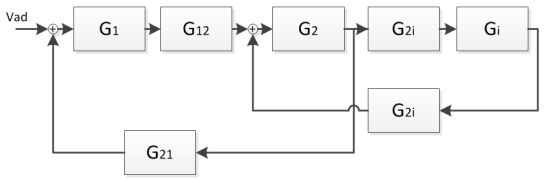

Figure 5.5: Simplified Model Diagram - Interfering Object coupled to Receiver

Similarly to the section above, the foreign object can be coupled only to the receiver coil and not the transmitter, thereby simplifying the general model described in section 5.2.1.2 as shown in 5.2.1.4..When this situation occurs, the transfer functions from foreign object to transmitter and the other way around are equal to 0 ($G_{1i} = G_{i1} = k_{i1} = k_{1i} = 0$). The equations of the current flowing through first (transmitter), second (receiver) and foreign object can be then simplified to:

$$\begin{aligned} V_1 &= V_{ad} + I_2 G_{21}; \qquad I_1 = V_1 G_1 \\ I_i &= (I_2 G_{2i}) G_i; \qquad I_2 = (I_1 G_{12} + I_i G_{i2}) G_2 \end{aligned} \tag{5.15}$$

which yields to:

$$I_1 = V_{ad} \frac{G_1}{1 + \frac{G_1 G_2 G_{21} G_{12}}{1 + G_i G_2 G_{2i} G_{i2}}} \tag{5.16}$$

The same procedure described in section 5.2.1.3 can be used in this simplified model. In this case, the effect of the foreign object only affects the output impedance of the system, and can be analyzed as a system without any interference but with a modified output impedance caused by the presence of the foreign object.

$$Z_{out} = Z_2 + \frac{(\omega M_{12})^2}{Z_1} + \frac{(\omega M_{i2})^2}{Z_i} \tag{5.17}$$

Using this result, the current that flows through the second coil can be expressed as:

$$I_2 = \frac{V_{ad} G_1 G_{12}}{Z_{out}} = V_{ad} \frac{G_1 G_{12} G_2}{1 + G_i G_2 G_{i2} G_{2i} + G_1 G_2 G_{12} G_{21}} \tag{5.18}$$

5.2.2 Design-Oriented Characterization of interfering objects

5.2.2.1 Interfering Object Coupled to Transmitter

In this section, the behavior of a RIC link in the presence of a foreign object only coupled to the transmitter ($k_{2i} = k_{i2} = 0$) is studied. The effects of the foreign object depend upon the natural resonant frequency of the foreign object with respect to the nominal resonant frequency of the RIC link ($\Delta f = (f_i - f_o)/f_o$), the resistance of the foreign object with respect to the load resistance ($\Delta R = R_i/R_L$) and the coupling between the object and the transmitter ($k_{i1} = k_{1i} \neq 0$). Therefore, these three variables (Δf, ΔR and k_{i1}) will be used to explore the effects of the foreign object upon the different system performance metrics, namely: Source Power, Power Transferred to the Load, Power coupled to the Interference and Power Transfer Efficiency.

Source Power

Due to the presence of the foreign object, the impedance of the source coil is modified, which can shift the frequency at which the maximum power is transferred, this is, the resonant frequency of the transmitter. In this case, this effect is of strong interest because the minimum impedance could appear at a frequency which does not correspond to the frequency at which the system efficiency is maximum (resonant frequency of the system without interference),thereby causing that, despite a very efficient system could be achieved, the actual power transferred from the source to the load would be very small. Using equation 5.7 and knowing that the maximum power at source will occur when the impedance is minimum, which is equivalent to consider the imaginary part of Z_{in} equal to 0, we can solve this set of equations to obtain the frequency at which the minimum impedance is achieved.

$$\begin{aligned} &\omega L_1 - \frac{1}{\omega C_1} + \frac{(\omega M_{1i})^2 (\frac{1}{\omega C_i} - \omega L_i)}{R_i^2 + (\omega L_i - \frac{1}{\omega C_i})^2} + \\ &+ \frac{(\omega M_{12})^2 (\frac{1}{\omega C_2} - \omega L_2)}{(R_2 + R_L)^2 + (\omega L_2 - \frac{1}{\omega C_2})^2} = 0 \end{aligned} \tag{5.19}$$

The effect of the interference upon the Source Power depends on the mutual couplings (k_{12} and k_{1i}, k_{i1}) and the receiver and interference impedances, namely:

- if $(Z_2 + R_L) > Z_i$: Z_{in} will be driven by the interference impedance and the minimum impedance frequency will shift to the frequency where $Z_{in} = Z_1 + (\omega M_{1i})^2/Zi$ is minimized.
- if $(Z_2 + R_L) < Z_i$: Z_{in} will be driven by the transmitter and receiver impedance, therefore being minimum at $f = f_o$.

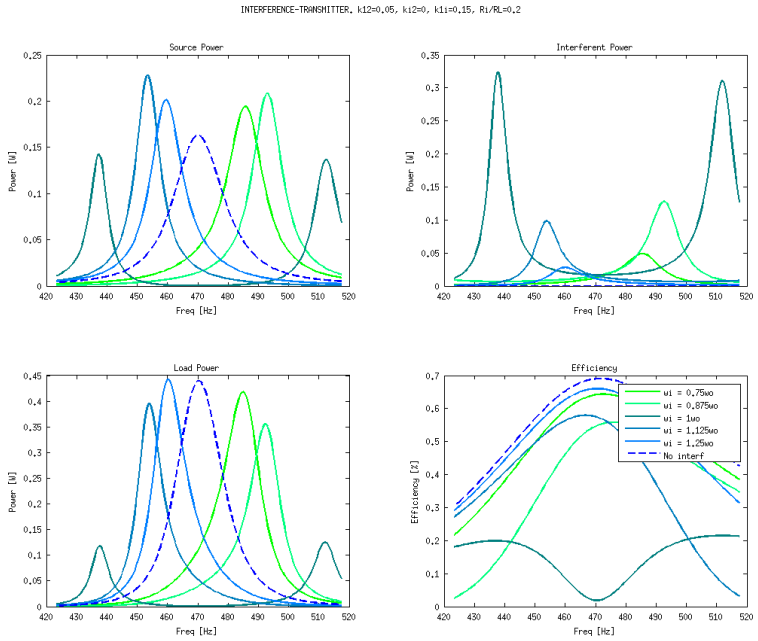

Figure 5.6: Interfering Object coupled to Transmitter. Low R_i ($Ri = 0.2R_L$)

In figure 5.2.2.1 and 5.7 this behavior is shown for a two-coil system resonating at a frequency of $f_o = 470Hz$ for $R_i = 0.2R_L$ (fig. 5.2.2.1) and $R_i = 10R_L$ (fig. 5.7) respeectively with $R_1 = R_2 = 0.4\Omega$, $R_L = 5\Omega$ and a fixed coupling factor between the coil and the foreign object of $k_{1i} = k_{i1} = 0.2$. In figure 5.2.2.1 it can be seen that if $R_i << R_L + R_2$ the maximum power from the source occurs at lower frequencies (shifted to the minimum impedance point due to the interference). However, if $R_i = R_L + R_2$ (as in figure 5.7) the resonant frequency of the foreign object has a very small impact upon the frequency at which the power delivered by the source is maximum, although it does on the maximum power value. For very high values of R_i the power transfer system is no longer affected by the foreign object. Finally, the relationship between the maximum source power frequency and the coupling between transmitter and foreign object is shown in 5.8, where the available source power from the source is shown for different values of coupling $k_{1i} = k_{i1}$ and in the scenario of a low resistance $R_i = 0.2R_L$ and a foreign object

frequency equal to the systems natural resonant frequency $\omega_i = \omega_o$.

Power Coupled to Interfering Object

The amount of power that is transferred from the source coil to the foreign object depends on the coupling $k_{i1} = k_{1i}$, its resonant frequency and resistance at resonance. The power coupled to the foreign object is maximum at the foreign object natural resonant frequency (minimum foreign object impedance Z_i and at the frequency at which the transmitter operates). Finally, the foreign object can be overcoupled, undercoupled and critically coupled to the transmitter, depending upon its impedance. By zeroing the derivative of the power transferred to the foreign object, the load that maximizes the current coupled to the interference (I_i) can be found as:

$$Z_i = \frac{(\omega k_{1i}\sqrt{L_1 L_i})^2}{(Z_2 + Z_L)} \tag{5.20}$$

which will be maximum when the resonant frequency of the system is the same as the natural resonant frequency of the foreign object $f_{oi} = f_o$ and proportional to $k_{1i} = k_{i1}$, which can be seen in figure 5.2.2.1 and 5.8.

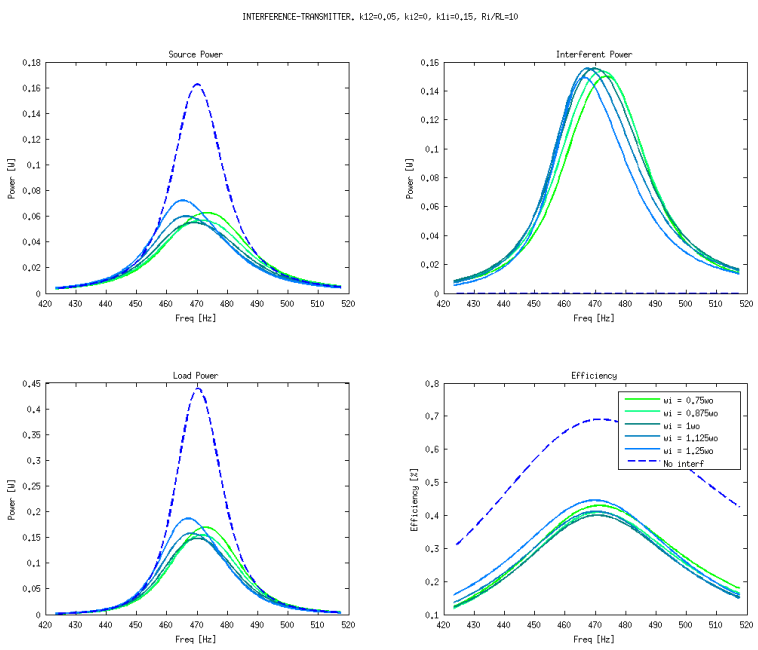

Figure 5.7: Interfering Object coupled to Transmitter. High Ri ($R_i = 10R_L$)

Power Transfer Efficiency

The power transfer efficiency is defined as the power effectively transferred to the load divided by the combined sum of losses of the system, including the power coupled to the foreign object. Hence, the power transfer efficiency depends on the foreign object resonant frequency Δf, the foreign object load (Z_i, R_i), the receiver

load (R_L) and the coupling between both transmitter-receiver and transmitter-foreign object. Similarly to the source power behavior, if the impedance of the foreign object is large enough with respect to the load impedance ($R_i >> R_L$), the maximum power transfer efficiency point does not experiment a frequency shift ($f_{max,\eta} \simeq f_{o1} = f_{o2} \neq f_{oi}$), as it can be seen in 5.2.2.1. However, if the impedance is small ($R_i << R_L$), the maximum power transfer efficiency points shifts to the foreign object frequency, as seen in 5.7.

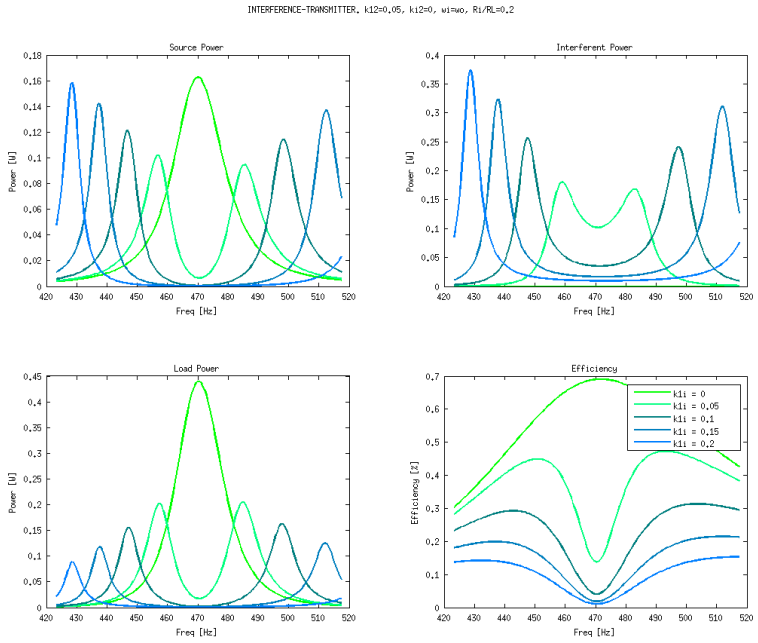

Figure 5.8: Interfering Object at Resonance (f_i=f_o) coupled to Transmitter. Low R_i ($R_i = 0.2R_L$) scenario.

Depending on the relation between the resonant frequency of the interference (f_{oi}) and the resonant frequency of transmitter and receiver coils ($f_{o1} = f_{o2}$), the power transfer efficiency maximum will experiment a frequency shift. This frequency shift will be inversely proportional to the difference $|f_{o1} - f_{oi}|$. Being the power transfer efficiency defined in 5.14, the maximum efficiency is found hence by setting the derivative of η with respect to f to 0. If the interference resonates at a frequency very distant from the frequency of transmitter and receiver, then the maximum power transfer efficiency still occurs at the same resonant frequency f_o. This behavior is shown in figure 5.7 where the power transfer efficiency of a two-coil system resonating at a frequency of $f_o = 470Hz$ (dotted line) is compared to the one obtained using the same system in the presence of a foreign object with $R_i = 10R_L$ resonating at $\omega_i = K\omega_o$ and coupled to the transmitter coil with $k_{1i} = 0.15$ and in figure 5.2.2.1 with a lower interfering resistance: $R_i = 0.2R_L$. It can be seen that when f_{oi} gets closer to the resonant frequency of the system $f_{oi} > f_o; f_{oi} \simeq f_o$ the frequency at which the maximum PTE occurs moves to

$f_{\eta_{max}} < f_o$. Similarly, if $f_{oi} < f_o; f_{oi} \simeq f_o$ then $f_{\eta_{max}} > f_o$. Finally, comparing figures 5.7 and 5.2.2.1 it can be easily seen that, if the resistance is lower, its effect upon power transfer efficiency in terms of frequency deviation is higher.

Load Power

When the foreign object is only coupled to the transmitter, its effects upon the received power at the load are a combination of the effects caused to the power transfer efficiency and to the power at source. Therefore, load power depends upon the coupling of the foreign object to the transmitter, load and foreign object impedances and resonant frequencies of foreign object and both transmitter and receiver. It is shown in figure 5.8 the resulting power load of a two-coil link at $f_o = 470Hz$ with an interference at $f_i = f_o$ and $R_i = 0.2\Omega$. In figure 5.8 it can be seen that, while the

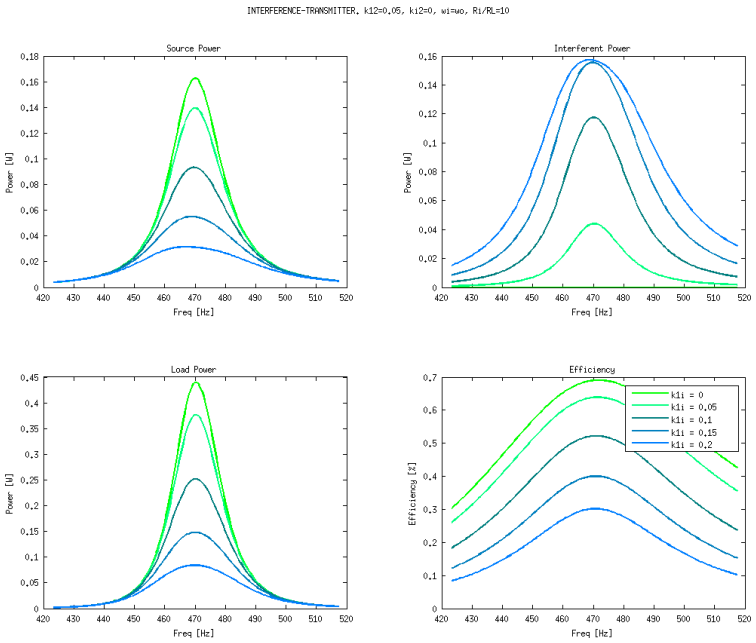

Figure 5.9: Interfering Object at Resonance ($f_i = f_o$) coupled to Transmitter. High R_i ($R_i = 10R_L$)

maximum source power occurs at near 470Hz, the maximum transfer efficiency can experiment a notch at the same frequency $f_i = f_o$, which causes the power received at load to be very small. This is due to an overcoupling between transmitter and foreign object, which is proportional to $k_{i1} = k_{1i}$. However, if $R_i >> R_L$ then the optimal frequency point is not modified, as seen in 5.9.

5.2.2.2 Design-Oriented Characterization of Interfering Object Coupled to Receiver

In this section, the behavior of a foreign object only coupled to the receiver ($k_{1i} = k_{i1} = 0$) is studied. The effects of such foreign object will depend upon the resonant frequency of the interference with respect to the resonant frequency of a coupled resonant system ($f_{o1} = f_{o2}$), the coupling between receiver and interference ($k_{i2} = k_{2i}$) and the load resistance. An object coupled only to the receiver can be seen as a modified output impedance. Since the output impedance is then shifted from the critical coupling, the system experiments a frequency and impedance mismatch, as seen in equation 5.17.

Source Power

Regarding the power available from the source, it is observed that, since the output impedance of the system is modified, if the coupling between transmitter and receiver is high enough, the reflected load of the foreign object upon the receiver does impact the transmitter source, thereby modifying its effective impedance. This behavior is shown in figure 5.10, where a link with a high coupling between transmitter and receiver ($k_{12} = 0.15$) is showcased.

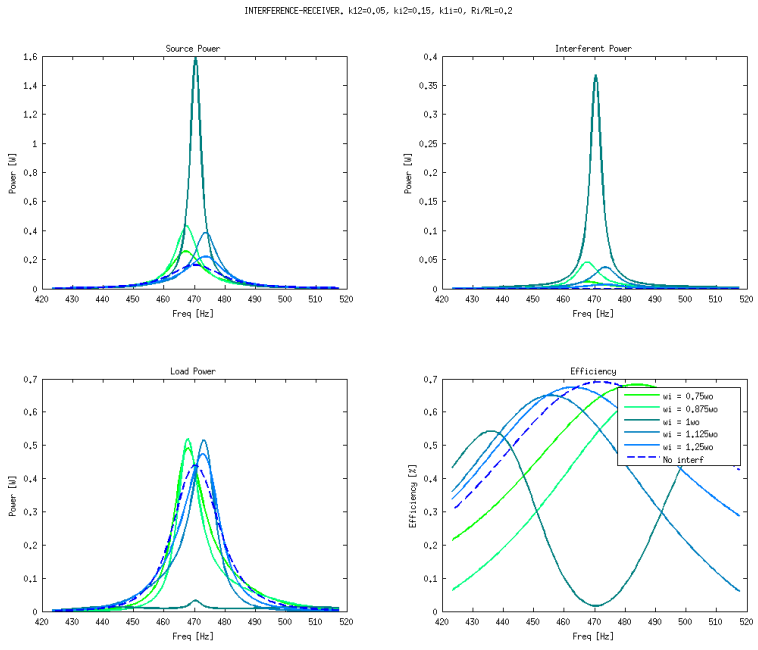

Figure 5.10: Interfering Object coupled to Receiver. Low R_i ($R_i = 0.2R_L$)

$$Z_{in} = Z_1 + \frac{(\omega M_{12})^2}{Z_2 + Z_L + \frac{(\omega M_{2i})^2}{Z_i}} \tag{5.21}$$

Since the impedance of the foreign object is small, at frequencies near the resonant

frequency of the system $f_{oi} \simeq f_o$, the effect of the reflected impedance back to the transmitter coil is not negligible. However, for large values of $R_i >> R_L + R_2$, the source power is not modified due to the foreign object, as seen in figure 5.11. On the other hand, if the impedance of the foreign object is low $R_i << R_L + R_2$ then the source power is modified in both frequency (due to the imaginary part of Z_i) and absolute value, as seen in 5.10.

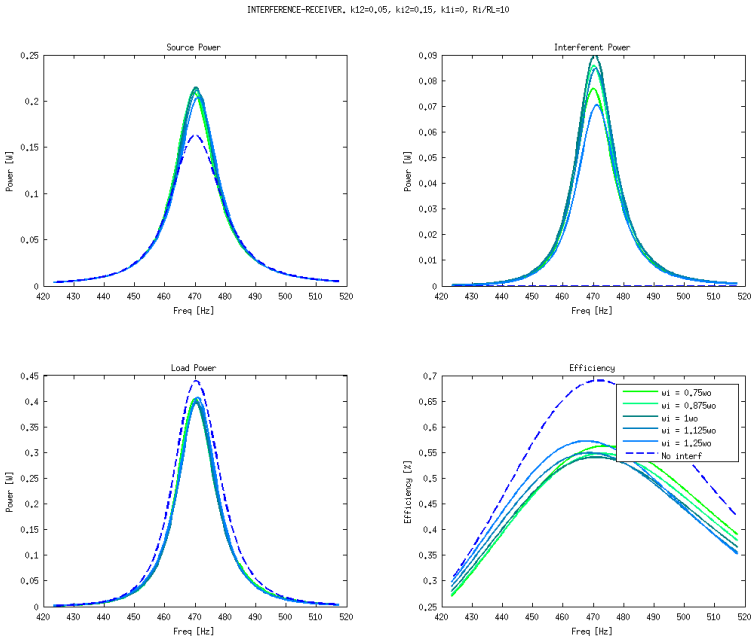

Figure 5.11: Interfering Object Coupled to Receiver. High R_i ($R_i = 10R_L$)

Interfering Object Power

Similarly to section 5.2.2.1, in which the foreign object was only coupled to the transmitter, the power received by the foreign object is also a function of the impedance of the foreign object, the natural resonant frequency of the foreign object and the coupling. Figure 5.12 shows the effect of a varying coupling between receiver and foreign object upon the power received at such object.

Load Power

Since the foreign object is only coupled to the receiver, this can be analyzed as a unmatched system with a complex load:

$$Z'_L = Z_L + \frac{(\omega M_{2i})^2}{Z_i} \tag{5.22}$$

Therefore, if $R_i >> Z_L$ the effect of the foreign object upon power transferred to the load is negligible. On the other hand, if $R_i << Z_L$ then the received power is diminished and depending on the coupling and the foreign object natural resonant frequency with respect to the resonant frequency of the system($\Delta f = (f_i - f_o)/f_o$) it can also experiment a frequency shift. Figures 5.10, 5.11, 5.12 and 5.13

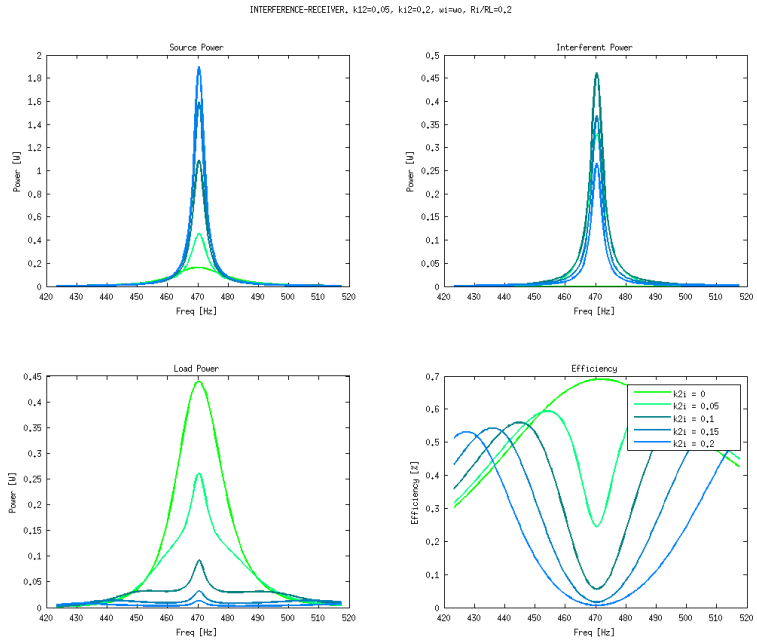

Figure 5.12: Interfering Object at Resonance ($f_i = f_o$) coupled to Receiver. Low R_i ($R_i = 0.2R_L$)

characterize this behavior for the complete parameter design space.

Power Transfer Efficiency

When the foreign object is only coupled to the receiver coil, the efficiency can be described using the expression below:

$$\eta = \frac{|I_2|^2 R_L}{|I_1|^2 R_1 + |I_2|^2 (R_2 + R_L + |\frac{\omega M_{2i}}{Z_i}|^2)} \tag{5.23}$$

The power transfer efficiency will then experiment a frequency shift proportional to Δf if the coupling between foreign object and receiver is high. On the other hand, if the coupling is low ($k_{2i} < k_{12}$), the power transfer efficiency will experiment a notch at a given frequency (frequency at which power from the receiver is coupled to the interference), as seen in figure 5.12, which is due to a higher power coupled to the foreign object.

5.2.2.3 Interfering Object Coupled to TX and RX

When the foreign object is coupled to both transmitter and receiver, the transfer functions of the system are affected by the combined effects described in previous sections for both de-embedded cases: only coupled to transmitter and only coupled to receiver. In this section, the behavior of such a generic system is analyzed and illustrated by means of a foreign object that is placed in different positions,

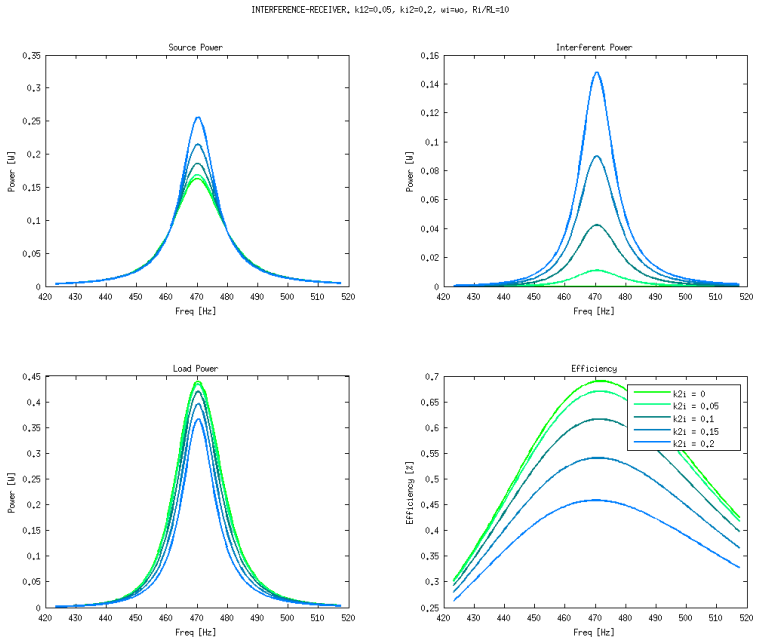

Figure 5.13: Interfering Object at Resonance ($f_i = f_o$) Coupled to Receiver. High R_i ($R_i = 10R_L$)

sweeping the full-range within a coupled wireless power transfer link. This object will experiment the three scenarios described above: only coupled to transmitter (when the foreign object is very near to the transmitter and far away from the receiver), coupled to both transmitter and receiver (when the foreign object is in between transmitter and receiver) and only coupled to the receiver (foreign object near to the receiver and far from the transmitter).

Source Power

Figure 5.14 explores the effects of a foreign object upon power available from the source. Several distances between receiver and transmitter are explored ($d_{12} = 0.3m - 0.8m$) and the foreign object is moved on the same plane so that it crosses through the three different regions (only coupled to transmitter, only to receiver and coupled to both transmitter and receiver). In addition, the foreign object resonant frequency is taken into account as a function of the resonant frequency of the system without interference ($f_{o1} = f_{o2} = f_o$).

In figure 5.14, it can be observed that, when the foreign object is in close proximity to the transmitter or the receiver, the power source available is lowered. For very high coupling values between transmitter and foreign object, the effect is independent of the resonant frequency of the foreign object. However, when the coupling is such that it is smaller than the coupling between transmitter and receiver, this effect is only visible when the object resonates at frequencies near the natural resonant frequency of the system. For large distances between transmitter and interference

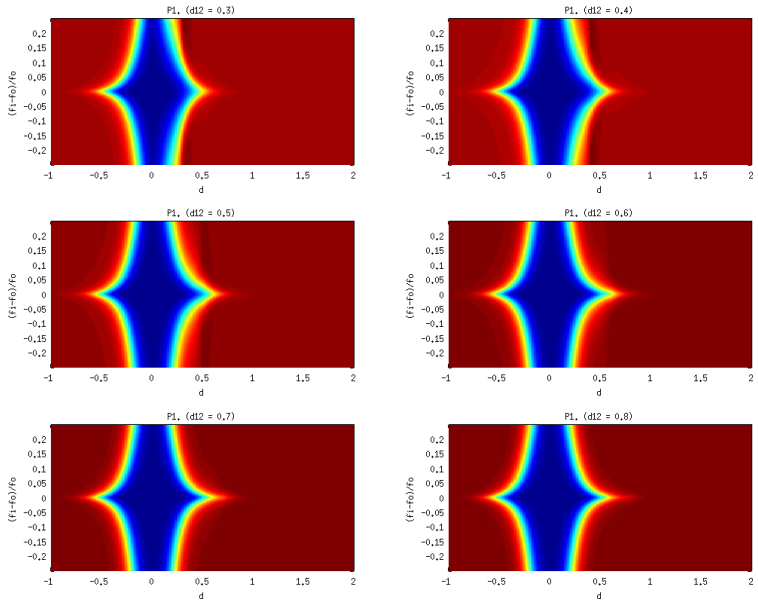

Figure 5.14: Source Power Characterization. Low Impedance Interfering Object ($R_i = 0.2R_L$)

and receiver and interference, this is, very low couplings, the effect of the external object is negligible and the behavior of the system tends to coincide with the interference-less system.

Load Power

The power available at the load is shown in 5.15 for a set of different distances between transmitter and receiver d_{12}. Several behaviors can be observed in this figure:

- When d_{12} is small, the power available at the load presents the effects of an overcoupling.
- When the foreign object is near the transmitter or the receiver, the power available at the load drops steadily. This is caused by an impedance mismatch caused by the presence of the foreign object.
- For small d_{12} and a foreign object between both, the system experiences an overcoupling and impedance mismatch in both source and load, thereby acting as an interference.
- When d_{12} is such that the presence of the foreign object between both does not overcouple the system, the interference acts as a relay. The presence of the foreign object increases the power at the load (or could otherwise extend the range), which can be easily seen for $d_{12} > 0.5$. Also, since the system experiments a frequency shift, the power is better transferred when the foreign object does not resonate at the same frequency than the receiver and

R_1	19mΩ
L_1	30μH
C_1	40nF
R_2	19mΩ
L_2	30μH
C_2	40nF
R_L	500mΩ

R_i	100mΩ
f_i	(0.85f_o - 1.15f_o)
L_i	30μH
f_o	144kHz
d_{12}	(0.3 - 0.8)m
$k_{12}(d_{12})$	(0.033 - 0.0016)

Table 5.1: System Parameters for Load Power Characterization - Low Impedance Interfering Object

transmitter. This is due to an overcoupling and impedance mismatch caused by the interfering load itself.

- For large d_{12} ($d_{12} > 0.6$), it can be seen that the power is only effectively transferred to the load when the foreign object is between the transmitter and the receiver, demonstrating the relay effect of such system.
- For very large distances, when the system is not overcoupled, the frequency at which the foreign object acts as a better relay is the natural resonant frequency of the system $f_i = f_{o1} = f_{o2}$.

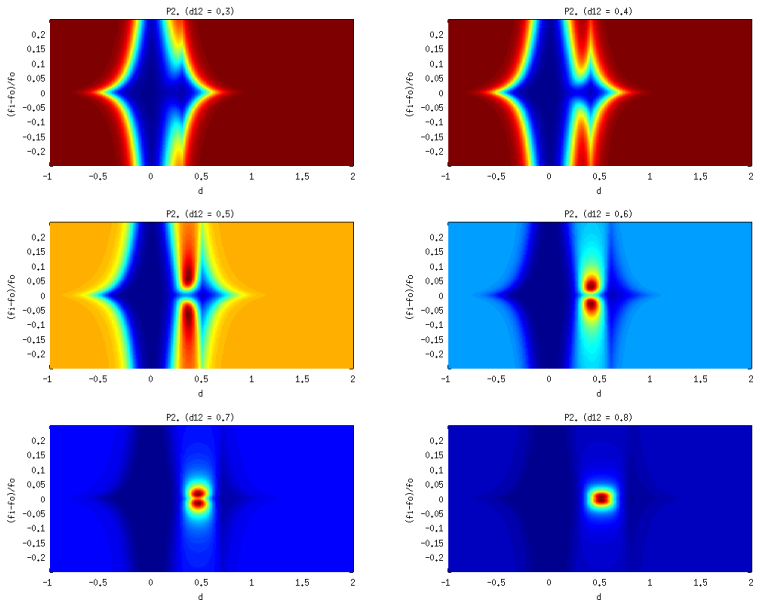

Figure 5.15: Load Power Characterization. Low Impedance Interfering Object ($R_i = 0.2R_L$)

Power Transfer Efficiency

Finally, the same design space exploration is performed to analyze the power transfer

efficiency behavior of the system. The first aspect that can be observed in figure 5.16 is that the effect of the foreign object near the transmitter or receiver is aggravated when the foreign object resonant frequency matches the resonant frequency of the system. On the other hand, when d_{12} is such that the foreign object starts acting as a relaying element (see subsequent section 5.3), for medium distances ($d_{12} = 0.5m$) the power transfer efficiency experiments a frequency splitting (therefore power is more efficiently transferred when the foreign object resonates at a different frequency from the system). On the other hand, for higher distances $d_{12} = 0.8m$, the only way to effectively transmit power to the receiver is by using the relay effect of an foreign object placed between transmitter and receiver and with a resonant frequency near the resonant frequency of the system.

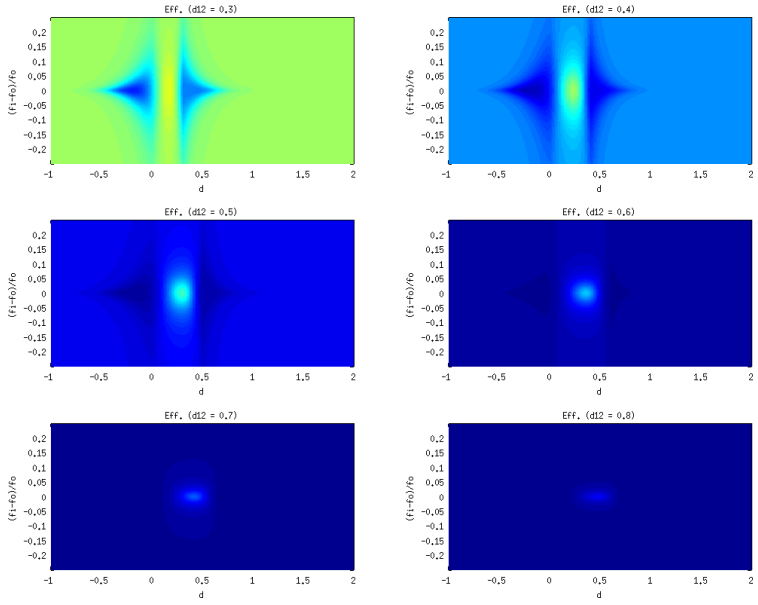

Figure 5.16: Power Transfer Efficiency Characterization. Low Impedance Interfering Object ($R_i = 0.2R_L$)

5.2.3 Overcoming Intefering Objects with Impedance Matching

Applying impedance matching techniques to source and load has demonstrated to increase the overall power transfer efficiency of a given link. In the presence of an foreign object, however, the required impedance to match the source needs to be modified to take into account such foreign object.

$$Z_L = Z_{out}* = \sqrt{Z_2^2 + \frac{Z_2(\omega M_{12})^2}{Z_1 + \frac{(\omega M_{1i})^2}{Z_i}} + \frac{Z_2(\omega M_{i2})^2}{Zi}} \tag{5.24}$$

Provided that the coupling between the foreign object and the receiver coil is null $k_{2i} = 0$, Z_L can be expressed as:

$$Z_L = Z_{out}* = \sqrt{Z_2^2 + \frac{Z_2(\omega M_{12})^2}{Z_1 + \frac{(\omega M_{1i})^2}{Z_i}}} \tag{5.25}$$

The optimal load impedance found from conjugately matching Z_{out} in equation 5.24 maximizes the power transferred to the load while derivating the power transfer efficiency in 5.23 with respect to Z_L to 0 will maximize the power transfer efficiency. In figure 5.17 the power transfer efficiency of a 2-coils plus interference RIC-WPT is shown with a) no impedance matching ($R_L = 50\Omega$) b) impedance matching without taking into account the foreign object ($R_{L,o}$) and c) impedance matching with the interference adjustment ($R_{L,o,i}$). To obtain maximum efficiency at the resonant frequency of the system, equation 5.25 has been used with $\omega = \omega_0 = 2\pi 18.19kHz$.

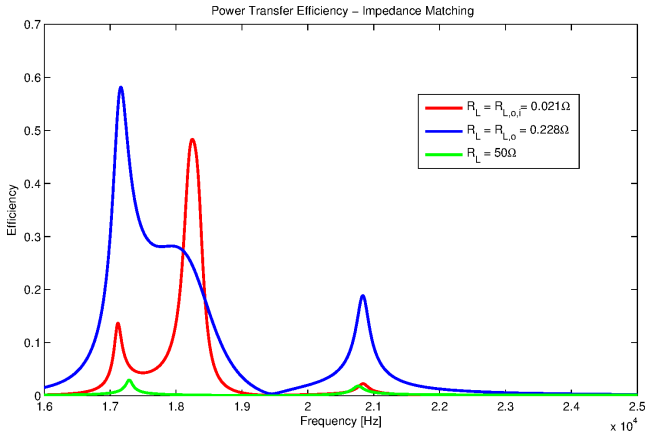

Figure 5.17: Impedance Matching

5.2.4 Finite-Element Field Solver Validation

In this section the results obtained using the circuit model described are verified with a Finite Element Field Solver Software (FEKO). To do this, a given interference (coil at 0.6 meters) has been measured with FEKO and approximated to its equivalent R_i,C_i and L_i representation. The coupling factors between the interference and the source coil k_{1i} and between transmitter and receiver coils k_{12} have been measured with FEKO and included in the circuit model. The obtained values for the foreign object are: $R_i = 13m\Omega$, $C_i = 5\mu F$, $L_i = 0.013mH$. The measured coupling factors are $k_{12} = 0.065$ at 0.6m and $k_{i1} = 0.1686$ at 0.1m. Figure 5.18 shows the input power source of the system obtained using the analytical method described and the results from FEKO simulation software for a two coil system with $R_1 = R_2 = 19m\Omega$, $R_L = 20m\Omega$, $f_{o1} = f_{o2} = 18.19kHz$, $f_{oi} = 19.45kHz$. In figure 5.18 it can be seen that the circuit model obtains very similar results to the finite element field solver.

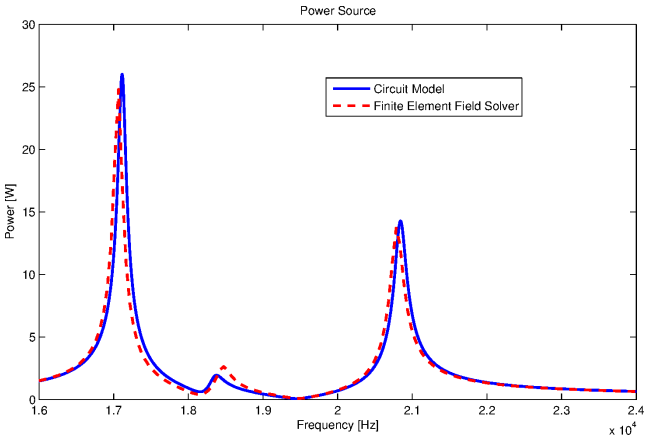

Figure 5.18: Power Source Circuit Model - Finite Element Field Solver

Differences can be explained by the used RLC circuit approximation of interference, transmitter and receiver impedances, which do not take into account frequency-dependant inductance and capacitance. In figure 5.19, the power transferred to the

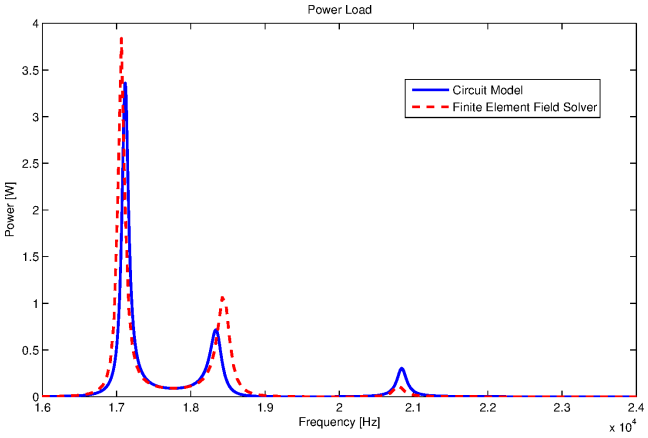

Figure 5.19: Power at Load

load at the receiver is shown for the same set of values. Figure 5.20 shows the power transfer efficiency defined as the power transferred to the load divided by the power available at the source $P_s = P_1 + P_2 + P_L + P_i$.

5.2.5 Experimental Validation

Experimental validation of a RIC link in the presence of a high-impedance foreign object (metal plate) at $\omega_i \neq \omega_0$ is shown in this section. Transmitter and receiver coils were made of 6061-O aluminum alloy with a rectangular cross-section of 0.1016cm x 0.635cm wrapped into a flat spiral of 20 windings with an inner diameter

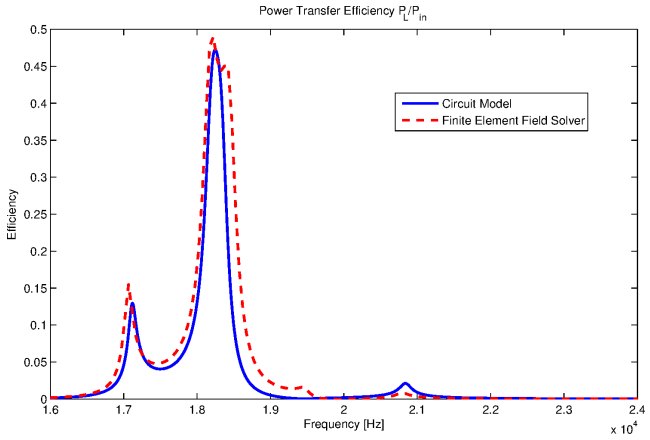

Figure 5.20: Power Transfer Efficiency

of 30cm and 0.1016cm between each of them. Five layers of the single flat spiral are vertically stacked together and electrically connected in series to create the resonant transmitting/receiving coils. The resonant frequency of the coils is dominated by an external capacitor $C = 10\mu F$ which is connected in parallel to the coils, resulting in $f_o = 462$Hz. The foreign object is an Aluminum plate of 61cm x 61cm x 0.32cm and coils were axially aligned at a 60cm distance, which can be seen in figure 5.21.

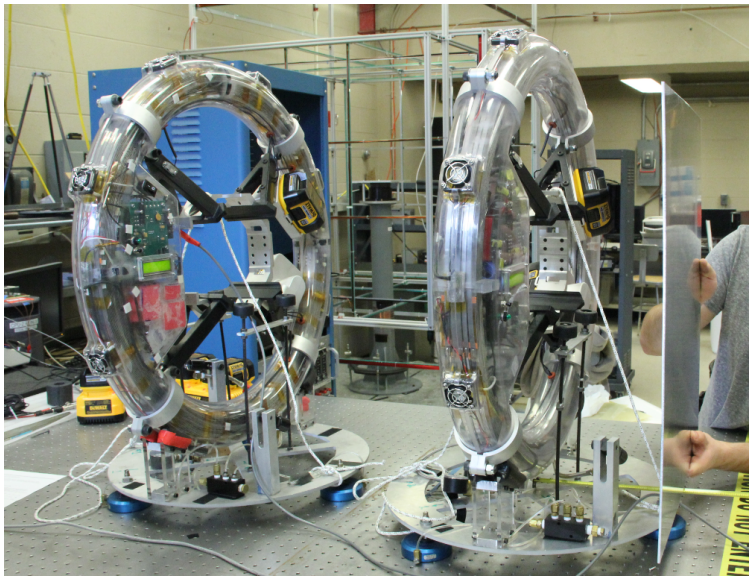

Figure 5.21: Experimental Setup: Transmitter, Receiver and Interfering Metal Plate. RINGS Project [81].

If the transmitter is considered to be placed at $d = 0$ and receiver at $d = 60cm$, the foreign object was placed before the transmitter ($d < 0$), between transmitter

and receiver ($0 < d < 60cm$) and after the receiver ($d > 60cm$). Currents running through the transmitter and receiver were measured and shown in figure 5.22. Physical obstructions on the RINGS [81] stands prevented the plate from being placed any closer to the coils, forcing $d_{1i} > 20cm$ and $d_{2i} > 20cm$. It can be observed that

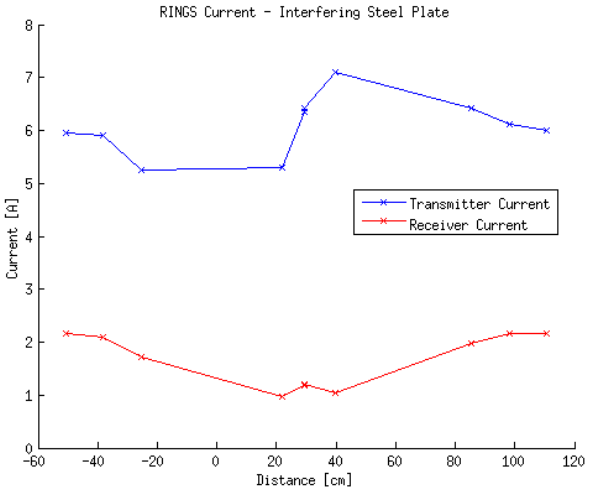

Figure 5.22: Transmitter and Receiver Currents. RINGS Experiment [81]

the effect of the metal plate in close proximity to the transmitter causes a drop in the transmitter current, due to causing a change in the source impedance. Since the system without foreign object was not critically matched, the effect of the foreign object also caused an increase of the source current at $d \simeq 50cm$. Regarding the receiver current, several behaviors, anticipated from the previous analysis, can be observed:

- When the distance between foreign object and transmitter/receiver is higher than 40cm, the effect of the metal plate becomes negligible. This is due to the object not having a natural resonant frequency close to the $f_o = 460$Hz and to a low coupling.

- When the foreign object is in close proximity to the transmitter or receiver, the current at the receiver drops due to the foreign object causing an impedance mismatch and change in the resonant frequency of transmitter or receiver respectively.

- Finally, when the foreign object is between transmitter and receiver coils, a slight increase in the current received by the receiver is visible. This is due to: a) the distance between foreign object and transmitter/receiver is increased and b) the foreign object acting as a relay and retransmitting some of the coupled field to the receiver.

5.2.6 Bridging the Circuit-Model to Magnetic Fields

While the functional forms of the equations defined above are quite complex, the factors that define the impact of the interfering object can be qualitatively understood to be:

- Resonant frequency of the interfering object with respect to the resonant frequency of the system: $\Delta f' = \frac{f_i - f_o}{f_o}$. The smaller the $\Delta f'$ isthe greater the effect of the interfering object will be. This is due to the fact that, near resonance, the reactive component of the impedance is greatly reduced, allowing for more current to flow and more power to be consumed by the resistive component.

- Resistance of the interfering object with respect to the load resistance: $R' = \frac{R_i}{R_L}$: if $R_i << R_L$, the system's input and output impedances (Z_{in} and Z_{out}) are driven by the interfering objects impedance, thus shifting the frequency response of the system depending upon $\Delta f'$. If $R_i >> R_L$ the effect of the interfering object is negligible.

- Distance and axial orientation between interference and transmitter/receiver, this is, coupling between interference and transmitter ($k_{i1} = k_{1i}$) and receiver ($k_{i2} = k_{2i}$). High values of coupling mean that the magnetic field is more effectively transmitted to the interfering object, which causes an increase of losses through coupling to the interfering object.

For simplicity, we suppose a RIC link in which transmitter and receiver share the same resonant frequency $\omega_o = \omega_1 = \omega_2$. Figures 5.23, 5.24, 5.25 showcase the effects explained above for a link resonating at $f_o = 240.8MHz$ made of two coils of 1-turn 16cm diameter with $R_1 = R_2 = R_{i,\Omega} = 60.9\Omega$, $L_1 = L_2 = L_i = 5.99uH$, $C_1 = C_2 = C_i = 0.0734pF$, $R_L = 70.2\Omega$ and $R_i = 45.5\Omega$.

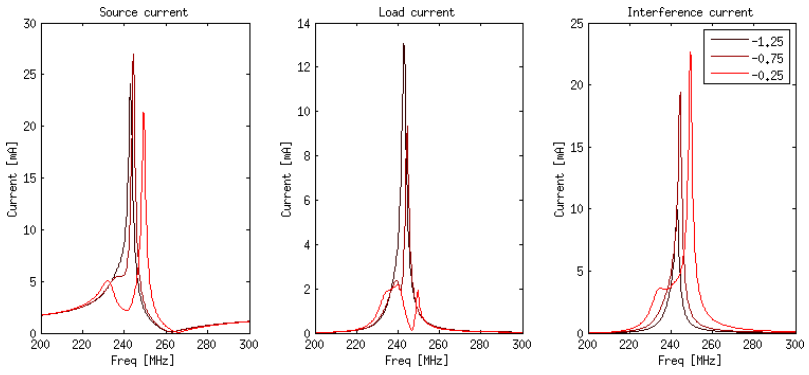

Figure 5.23: Currents in Transmitter, Load and Interference. FEKO Simulation. Transmitter Coupled

In figure 5.23, the interfering object is placed before the transmitter at several distances, represented as multiples of the antenna diameter: -1.25D, -1D, -0.75D, -0.5D, -0.25D. In this case, the interfering object is mostly coupled to transmitter ($k_{1i} = k_{i1} \neq 0$, $k_{i2} = k_{2i} \simeq 0$). It can be seen that the frequency response of the power available from the source is modified due to the presence of the interfering object and that the effect of a near object ($d_{i1} < 0.5D$) increases the power received at the interference and, at the same time, decreases the power received at load. Finally, if the distance $d_{1i} > 1D$, the effect of the interfering object is negligible. This is due to a low coupling $k_{1i}(d_{i1})$.

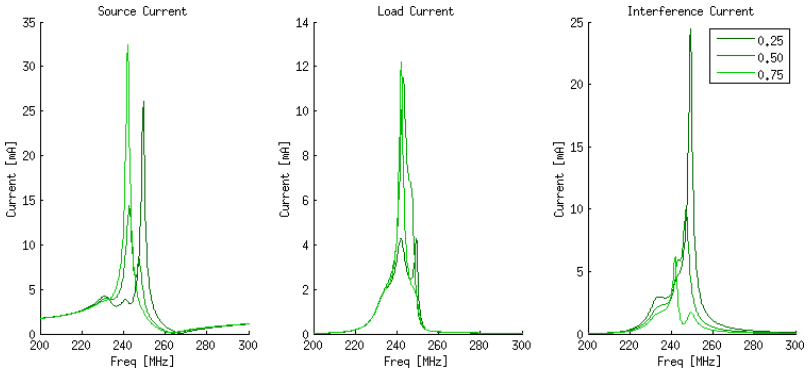

Figure 5.24: Currents in Transmitter, Load and Interference. FEKO Simulation. Transmitter and Receiver Coupled

Figure 5.24 illustrates the same scenario but with the interfering object placed between transmitter and receiver. It can be seen that, when the interfering object is in close proximity to the transmitter $d = 0.25D$, the source impedance is modified and the frequency response of the source current shifts and presents multiple peaks, thereby presenting an overcoupled response. Regarding the current at the load (receiver), we can see that it is maximum when the interfering object is placed between transmitter and receiver $d = 0.5D$ and that the current is higher than in the case of the same system operating without any interference. This is due to the intefering object acting as a relay between transmitter and receiver. Since the impedance of the interfering object is lower than the impedance of the load, more power is effectively transferred to the load. Finally, when the interfering object is closer to the receiver ($d = 0.75D$) it receives less power and its effect upon the power transfer link is causing an impedance mismatch at the receiver.

Finally, figure 5.25 illustrates the situation in which the interfering object is placed only near the receiver $d = 1.25D, 1.50D, 1.75D$ and $2D$. We can see that the effect upon the source power is negligible ($k_{i1} = k_{1i} \simeq 0$) and that, for large distances $d > 1D$, the effect of the interfering object upon the current the load receives is very small.

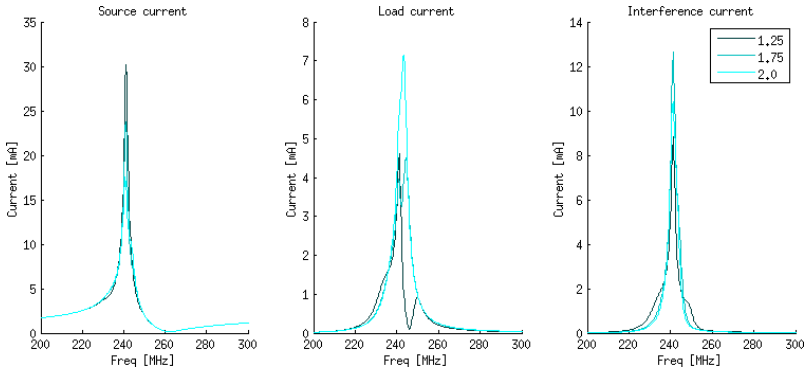

Figure 5.25: Currents in Transmitter, Load and Interference. FEKO Simulation. Receiver Coupled

5.2.6.1 Magnetic Characterization

In this section, a magnetic characterization of a RIC link in the presence of an interfering object obtained by a Finite Element Field Solver FEKO is presented to validate the previous design-oriented model-based results. This link is made of a 1-turn 16cm diameter coils with $R_1 = R_2 = R_{i,\Omega} = 58.8\Omega$, $L_1 = L_2 = L_i = 5.99uH$, $C_1 = C_2 = C_i = 0.075pF$. A load is added to the second coil $R_L = 33.3\Omega$ and a smaller one ($R_i << R_L$) to the interfering object $R_i = 0.1R_L$.

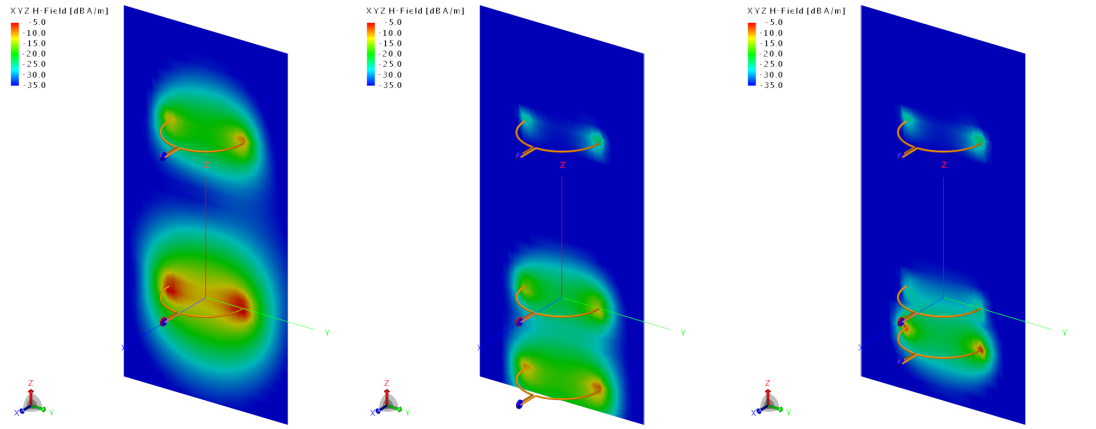

a) No Interference b) $d_{i1} = -1m$, $d_{i2} = -3m$ c) $d_{i1} = -0.5m$, $d_{i2} = -2.5m$

Figure 5.26: Magnetic Field Distribution of a RIC link with a resonant interfering object near the Transmitter

Figure 5.26 compares the magnetic field of a RIC link without any interfering object (a) to the one with an interfering object only coupled to the transmitter (b and c). In this case, two effects can be observed: first, the magnetic field that

effectively arrives to the load (receiver) is smaller. This is due to an impedance mismatch caused by the interfering object, which reduces the power provided by the source coil. Second, the interfering object, now in close proximity to the transmitter, receives most of the magnetic field, which is caused by a smaller interfering object resistance ($R_i << R_L$) and a higher coupling $k_{i1} = k_{1i} > k_{12} = k_{21}$.

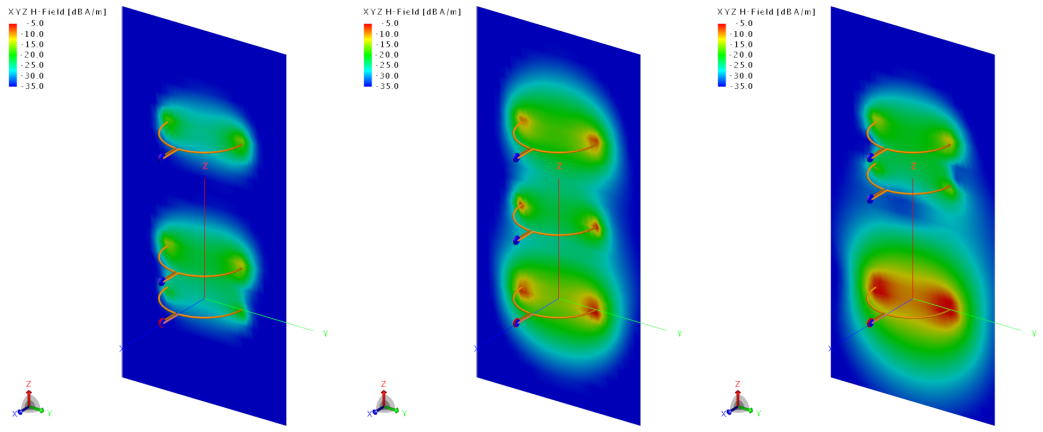

a) $d_{i1} = 0.5m$, $d_{i2} = 1.5m$ b) $d_{i1} = 1m$, $d_{i2} = 1m$ c) $d_{i1} = 1.5m$, $d_{i2} = 0.5m$

Figure 5.27: Magnetic Field Distribution of a RIC link with a resonant interfering object between Transmitter and Receiver

Figure 5.27 explores the effect of an interfering object between transmitter and receiver for three different distances: near the transmitter(a), in between(b) and near the receiver(c).

- If the interfering object is near the transmitter (case a), the effect is similar to the one described in figure 5.26b and 5.26c: the source impedance is modified, thereby decreasing the power available from the source and more power is coupled to the interfering object. However, in this case, the effect is diminished by the fact that part of the field that is effectively transferred to the interfering object is later transferred to the receiver, increasing the magnetic field at the load.

- If the interfering object is in between transmitter and receiver (case b), the magnetic field that is coupled to the receiver is increased with respect to the one obtained without any interfering object (figure 5.26a). The interfering object is, in this case, acting as a relay. This result agrees with the increase of the current at the receiver shown in figure 5.24. For this to happen, several things have to occur: first, the interfering object impedance has to be low in order to retransmit efficiently. Secondly, the interference has to be resonant at the same frequency of the system $\omega_i = \omega_o$. Third, the interfering object has to be sufficiently far away from the transmitter and receiver in order to minimize the impedance mismatch.

- If the interfering object is near the receiver (case c), the magnetic field at the receiver is lowered due to an impedance mismatch caused by the close proximity of interfering and receiver coils. Since the coupling between transmitter and interfering object is not negligible, the source power is also modified.

Finally, figure 5.28 shows the effect of the interfering object far from the transmitter ($k_{i1} = k_{1i} \simeq 0$) and in close proximity to the receiver ($k_{i2} = k_{2i} \neq 0$). Since the coupling between interference and source is very small, the source power is not affected by it. On the other hand, the receiver does experience an impedance mismatch, which results in less power transferred to it, and some of the power coupled to the receiver is later transferred to the interfering object, this is, the receiver acts as a high-loss relay between the source coil and the interfering object.

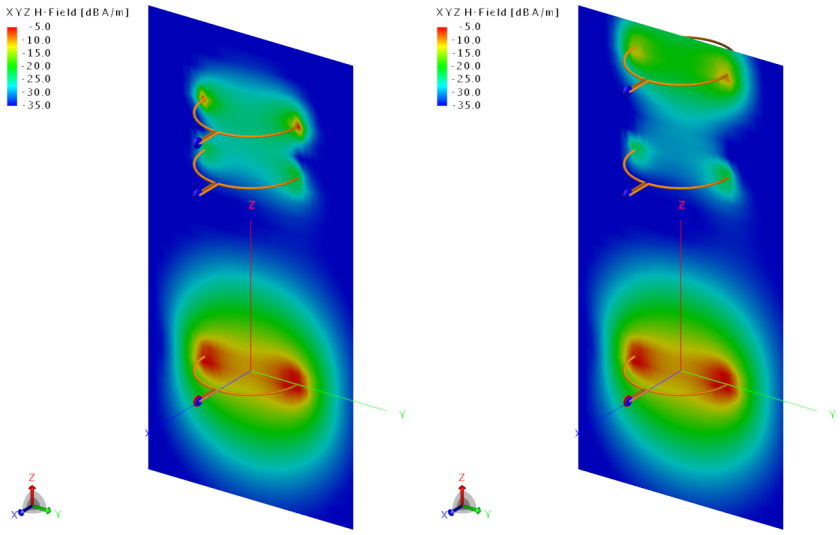

a) $d_{i1} = 2.5m$, $d_{i2} = 0.5m$ b) $d_{i1} = 3m$, $d_{i2} = 1m$

Figure 5.28: Magnetic Field Distribution of a RIC link with a resonant interfering object near the Receiver

5.3 Relaying Effects in RIC-WPT

As explained in previous sections, the behavior of a multiple-node Resonant Inductive Coupling system has a strong dependance upon a) the interfering objects in the vicinity of the link (intrinsic to the system or foreign) and b) their impedances, which will modulate their effect as an interference or a relay. This chapter provides an analytical model for Multi-Node Resonant Inductive Coupling links together with an impedance analysis to understand and optimize system performance based upon this design parameter.

5.3.1 Analytical Model of Relay Effects in multiple-node RIC WPT

In this section, the relaying effects described in previous chapters 5.2 are extended to a Multi-Node RIC WPT Scenario, in which a Single Input - Multiple Output System can have several nodes acting as relays that enhance the behavior of the System through a multi-path relaying effect. SIMO, which generally stands for single-input multi-output systems are used in this context as a denomination of a RIC-WPT with single transmitter or input energy port and multiple receiver or output energy ports, not to be confused with the stablished use of SIMO/MIMO in the communications discipline to connote methods for multiplying the capacity of a radio link [82].
To analyze this behavior, an analytical model of a MIMO System can be used [37], in which the behavior of the system is defined by the equations:

$$\begin{pmatrix} I_1 \\ I_2 \\ .. \\ I_n \end{pmatrix} = \begin{pmatrix} 0 & Z_{21}Y_1 & .. & Z_{n1}Y_1 \\ Z_{12}Y_2 & 0 & .. & Z_{n2}Y_2 \\ .. & .. & .. & .. \\ Z_{1n}Y_n & Z_{2n}Y_n & .. & 0 \end{pmatrix} \begin{pmatrix} I_1 \\ I_2 \\ .. \\ I_n \end{pmatrix} + \begin{pmatrix} V_1Y_1 \\ V_2Y_2 \\ .. \\ V_nY_n \end{pmatrix} \tag{5.26}$$

To analyze the relaying effect, only three different types of nodes are considered: a transmitter node G_t, a receiver node G_r and the interfering/relaying nodes G_i. Under this assumption, the system of equations is particularized to:

$$\begin{pmatrix} I_t \\ I_i \\ I_i \\ I_r \end{pmatrix} = \begin{pmatrix} 0 & Z_{ti}Y_t & Z_{ti}Y_t & Z_{tr}Y_t \\ Z_{ti}Y_i & 0 & Z_{ii}Y_i & Z_{ir}Y_i \\ Z_{ti}Y_i & Z_{ii}Y_i & 0 & Z_{ir}Y_i \\ Z_{tr}Y_r & Z_{ir}Y_r & Z_{ir}Y_r & 0 \end{pmatrix} \begin{pmatrix} I_t \\ I_i \\ I_i \\ I_r \end{pmatrix} + \begin{pmatrix} VY_t \\ 0 \\ 0 \\ 0 \end{pmatrix} \tag{5.27}$$

Solving this system of equations for N nodes and considering that 1) the coupling between the transmitter and all the interfering objects is the same, 2) the coupling between all the interfering objects and the receiver is the same and 3) the interfering objects are only coupled to the adjacent nodes, it is obtained:

$$\begin{aligned} I_t &= \frac{VY_t[(N-2)Y_iY_rZ_{ri}^2 + 2Y_iZ_{ii} - 1]}{A} \\ I_i &= \frac{VY_iY_t[Z_{ti} + Y_rZ_{ri}Z_{tr}]}{A} \\ I_r &= \frac{VY_rY_t[Z_{tr}(1 - 2Y_iZ_{ii}) + (N-2)Y_iZ_{ri}Z_{ti}]}{A} \end{aligned} \tag{5.28}$$

where

$$\begin{aligned} A = (N-2)Y_i[Y_rZ_{ri}(2Y_tZ_{ti}Z_{tr} + Z_{ri}) + Y_tZ_{ti}^2] + \\ +2Y_iZ_{ii}(1 - Y_rY_tZ_{tr}^2) + Y_rY_tZ_{tr}^2 - 1 \end{aligned} \tag{5.29}$$

and the current is the same in any of the interfering nodes. Once the currents are known, the power at the transmitter P_t, the power at each interfering/relaying node

P_i, the power at the receiver P_r and the power transferred to the load P_{rl} are:

$$\begin{aligned} P_t &= |I_t|^2\mathbb{R}\frac{1}{2Y_t}; \quad P_i = |I_i|^2\mathbb{R}\frac{1}{2Y_i} \\ P_r &= |I_r|^2\mathbb{R}\frac{1}{2Y_r}; \quad P_{rl} = \frac{|I_r|^2}{2}R_L \end{aligned} \tag{5.30}$$

The total input power of the system can be found equal to the sum of the powers as:

$$\begin{aligned} P_{in} = P_t + \sum_{N-2} P_{i,N} + P_r = P_t + (N-2)P_i + P_r = \\ V^2\frac{Y_t^2((N_2)Y_iY_rZ_{ri}^2 + 2Y_iZ_{ii} - 1)^2}{A^2}\mathbb{R}Z_t + \\ (N-2)V^2\frac{(Y_iY_t[Z_{ti} + Y_rZ_{ri}Z_{tr}])^2}{A^2}\mathbb{R}Z_i + \\ V^2\frac{(Y_rY_t[Z_{tr}(1-2Y_iZ_{ii}) + (N-2)Y_iZ_{ri}Z_{ti}])^2}{A^2}\mathbb{R}Z_r \end{aligned} \tag{5.31}$$

And the output power of the system is equivalent to the power transferred to the load:

$$P_{out} = V^2\frac{(Y_rY_t[Z_{tr}(1-2Y_iZ_{ii}) + (N-2)Y_iZ_{ri}Z_{ti}])^2}{A^2}R_L \tag{5.32}$$

Finally, the efficiency of the system is defined as:

$$\begin{aligned} \eta &= \frac{P_{out}}{P_{in}} = \frac{(Y_rY_t[Z_{tr}(1-2Y_iZ_{ii}) + (N-2)Y_iZ_{ri}Z_{ti}])^2R_L}{D+E+F} \\ D &= Y_t^2((N_2)Y_iY_rZ_{ri}^2 + 2Y_iZ_{ii} - 1)^2\mathbb{R}(Z_t) \\ E &= (N-2)(Y_iY_t[Z_{ti} + Y_rZ_{ri}Z_{tr}])^2\mathbb{R}(Z_i) \\ F &= (Y_rY_t[Z_{tr}(1-2Y_iZ_{ii}) + (N-2)Y_iZ_{ri}Z_{ti}])^2\mathbb{R}(Z_r) \end{aligned} \tag{5.33}$$

5.3.2 Design-Oriented Impedance Characterization

From the analytical model described above, it can be seen that the behavior of the system strongly depends upon the impedances of the transmitter, receiver and interfering nodes. In this section the resonant frequency has been designed to be the same in each node to fulfill two objectives: first, the target application of a multi-path relaying scenario is a SIMO system with some nodes acting as receivers and others acting as interfering/relaying nodes, which requires that all the nodes operate at the same frequency (in order to resonate when acting as receivers). Second, to maximize the relaying effect of the interfering object, the magnetic field transferred to it should be maximized. In such scenario, the resistive load of the interfering object (ohmic and radiative losses) relative to the transmitter and receiver resistances and the receiver load have a strong effect upon the behavior of the system. The effect of the node resistance on the relaying capabilities of the interfering nodes is analyzed in this section and illustrated with regards to the

efficiency of the system. For this purpose, a 10-Node (1 transmitter, 1 receiver and 8 interfering nodes) RIC WPT System with the geometrical distribution displayed in figure 5.29 is studied, chosen for its relevance within the application and because it is representative of the multi-node system behavior [78].

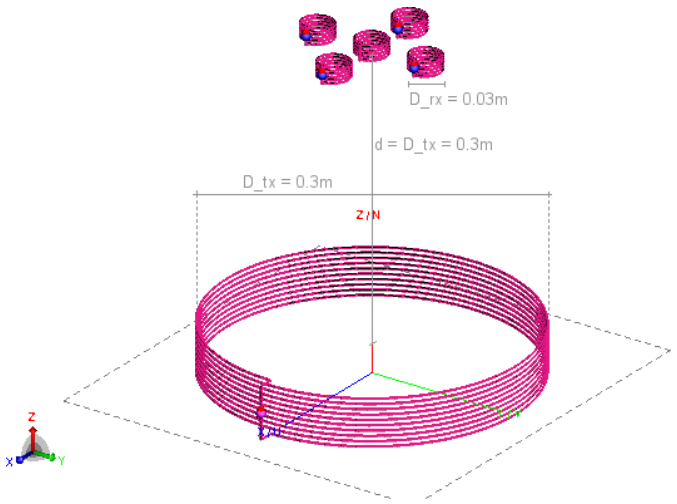

Figure 5.29: Multi-Node RIC WPT System

In this system, the coupling between transmitter and interfering nodes (k_{ti}), the coupling between receiver and interfering nodes (k_{ri}), and the coupling between adjacent interfering nodes (k_{ii}) has been considered equal (and obtained through the Finite Element Field Solver FEKO). This section presents the effect of the transmitter, receiver and interfering node impedances upon the power transfer efficiency, calculated as the quotient between the power transferred to the system P_{in} and the power obtained by the receiver P_{out} through direct transmission ($P_{in,out}$) and through the interfering nodes ($P_{j,out}; j = 1..8$).

R_r	5.56Ω
R_L	0.5Ω
$R_i(Fig.4,5)$	Swept: R_L to $10R_L$
$R_t(Fig.4,5)$	Fixed: 53mΩ
$R_i(Fig.6,7)$	Fixed: 53mΩ
$R_t(Fig.6,7)$	Swept: R_L to $10R_L$
f_o	6.625MHz

L_t	0.26mH
L_r	686nH
L_i	686nH
k_{ti}	5.89E-4
k_{tr}	5.89E-4
k_{ri}	0.015
k_{ii}	0.015

Table 5.2: System Design Variables

Figure 5.30 shows the power transfer efficiency (in percentage, normalized to 1) of the system for different values of interfering object resistance normalized to the load of the system. Figure 5.30(a) showcases the behavior of the system and figure

5.30(b) displays the frequency response for different values of R_i for illustration purposes. In this figure several behaviors can be observed:

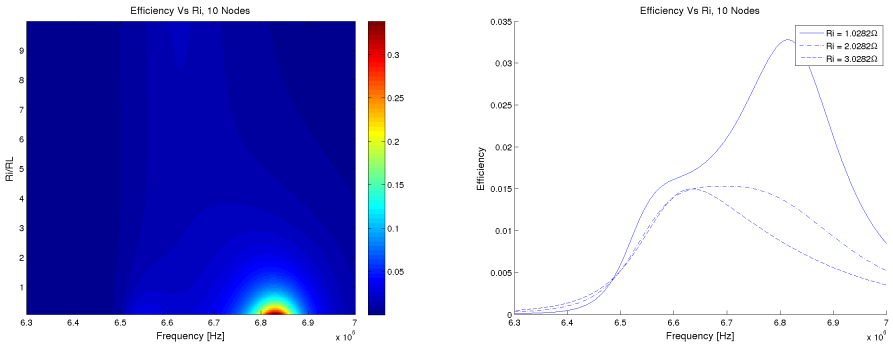

(a) Ri/RL. 10-Node RIC System

(b) Ri/RL. 10-Node RIC System

Figure 5.30: Interfering Resistance - RIC WPT with 8 Relaying Nodes

- There is a positive multi-node relaying effect that increases the power transfer efficiency of the system when the losses of the interfering nodes are small compared to the load of the system ($R_i/R_L < 3$).
- When the interfering object resistance is high compared to the load resistance, the interfering objects have no effect upon the power transfer efficiency. Looking at figure 5.31 it is possible to observe that the system with 8 interfering nodes has the same power transfer efficiency than a system without any interfering nodes, provided that their resistance is high compared to the load of the system $R_i > 9R_L$.
- The relaying effect also causes a change of the frequency at which maximum power transfer efficiency is obtained, which causes a frequency deviation from the resonant frequency of the system.

Analogous results are shown in figure 5.31 for a system with no interfering object (2 Nodes: transmitter and receiver). It can be seen that the system response to a change on the interfering object resistance is null, which is consistent with having no interfering nodes. However, this figure is shown here to provide a fair comparison of the system behavior with and without interfering objects.

It is of interest to characterize not only the effect of the interfering resistance but also the effect of transmitter resistance upon Single-Node and Multi-Node RIC WPT Systems. Figure 5.32 and 5.33 showcase this effect for Multi-Node and Single-Node scenarios respectively.

Comparing the two figures, it is possible to observe that an increase in the transmitter losses has a detrimental effect in both cases. However, due to the presence of the relaying nodes, a higher power transfer efficiency can be obtained even with

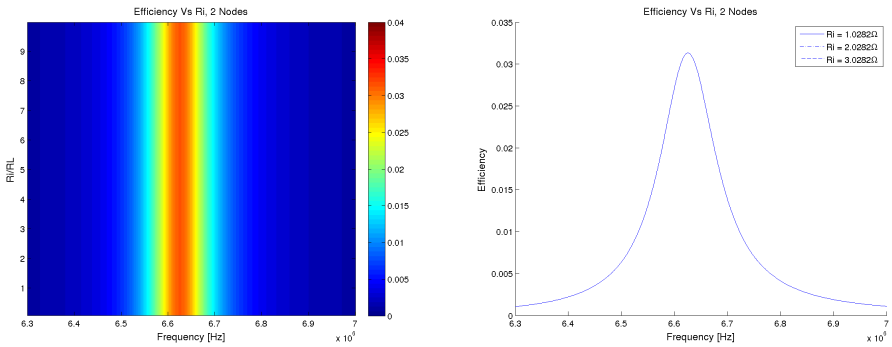

(a) Ri/RL 2-Node RIC System (b) Ri/RL 2-Node RIC System

Figure 5.31: Interfering Resistance - RIC WPT System without Relaying Nodes

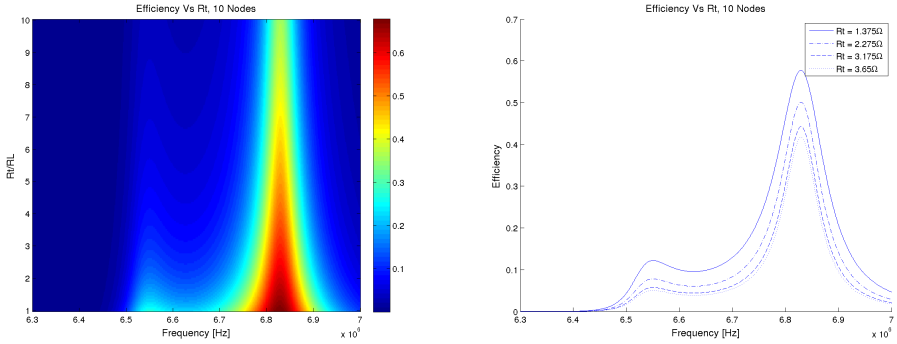

(a) Rt/RL. 10-Node RIC System (b) Rt/RL. 10-Node RIC System

Figure 5.32: Transmitter Resistance - RIC WPT with 8 Relaying Nodes

a high transmitter resistance compared to the receiver load. Finally, it is possible to calculate the maximum efficiency in both scenarios (with and without relaying nodes).

Figure 5.34 shows the normalized efficiency $\eta_{multi-node}/\eta_{pp}$ for different interfering object resistance and transmitter resistance values (normalized to the load resistance of the system) where it can be observed that: 1) when the interfering object resistance is small, the power transfer efficiency is greatly increased with respect to the efficiency without any relaying nodes. 2) when the interfering object resistance is close to the load resistance, the increase in efficiency is still significant (around twice the efficiency without relaying nodes) and 3) the relaying effect starts to be negligible when the resistance of the relaying nodes is higher than the load resistance. Finally, it is important to note that for a given R_i there is an optimal R_t that maximizes the efficiency. In point-to-point systems, the output resistance of the system is optimal in terms of efficiency for a given R_L, R_T [40][41]. Trans-

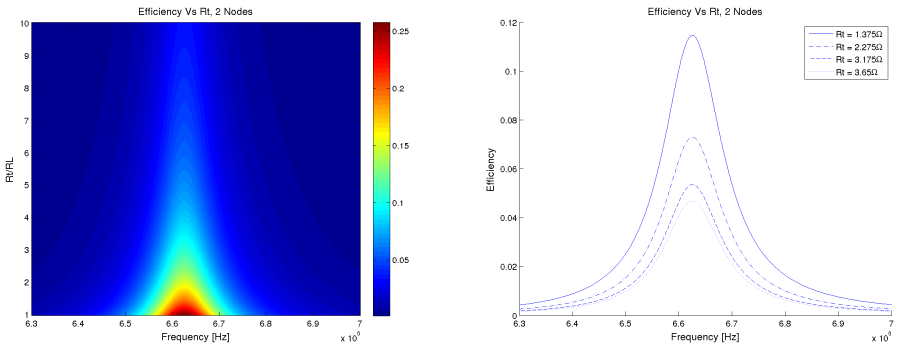

(a) Rt/RL. 2-Node RIC System

(b) Rt/RL. 2-Node RIC System

Figure 5.33: Transmitter Resistance - RIC WPT without Relaying Nodes

lating this to a Multi-Node scenario means that there is a combination of R_L and reflected impedances of the interfering nodes R_i that optimize the same output resistance. It is possible to observe that when the resistance of the transmitter is low, the system acts in the over-coupled regime, thereby requiring higher interfering node impedances to counteract this effect. On the other hand, if a higher transmitter resistance is considered, the required interfering node impedance to operate in maximum efficiency conditions is lowered. The very purpose of Figure 5.34 is to provide system design guidelines and in turn a method to realize the best efficiency when considering as open design variables the coil parasitic resistances for the multi-receiver scenario characterized in this work.

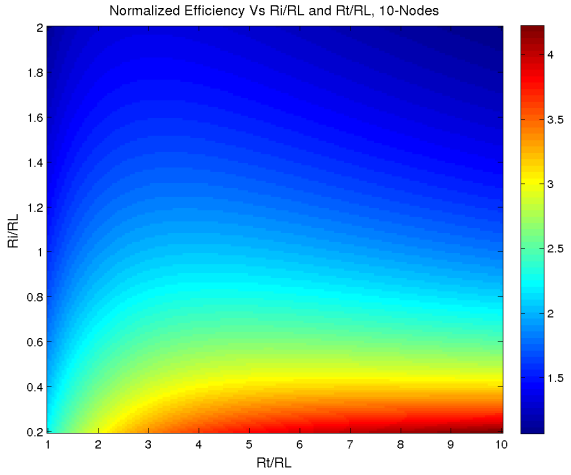

Figure 5.34: Efficiency Normalized to Efficiency Without interfering Nodes

5.4 Conclusions

In this chapter we have presented a model that predicts the behavior of resonant inductive coupled wireless power transfer systems in the presence of a foreign object. This design-oriented model has been analized for three different scenarios: foreign object only coupled to transmitter, only coupled to receiver or coupled to both transmitter and receiver; and its effects have been studied separately. The behavior of such system has been qualitatively examined and the relay effect, caused by the foreign object being placed between transmitter and receiver has been identified and explored. Finally, the model has been illustrated and validated first with a Finite-Element Field Solver (FEKO) and later with an experimental setup as part of the NASA RINGS Project [83].

The relaying effects in point-to-point resonant inductive coupling WPT link have been revisited and extended to the scenario of multiple node systems potentially acting as relays showing interdependence. This extended study has been carried out by means of an analytical circuit-based multidimensional model. Beyond such formal extension and its corresponding matrix description, the model has been benchmark validated with electromagnetic numerical simulations to characterize multi-coil relaying effects. The study considers representative implementation, design and application variables such as resistances of the transmitter, receiver and interfering nodes in the SIMO WPT system, thereby providing a design-oriented exploration of relay effects in multiple receiving coil systems both unveiling fundamental limits and practical interest in WPT system deployments. This work demonstrates a multi-node RIC WPT scenario which could potentially benefit a lot of applications such as wireless sensor networks and IoT.

Chapter 6

System Codesign

Contents

6.1 Introduction

Previous chapters have reviewed the fundamental challenges precluding the growth of RIC-WPT and design guidelines to overcome these challenges have been provided. However, due to the very multidomain nature of RIC and the interrelationship between the design components, it is necessary not only to optimize the wireless power transfer link but also the efficiency of the DC-AC and AC-DC converters. The efficiency of a WPT link can be expressed by:

$$\eta_{sys} = \eta_{DC-AC}\eta_L\eta_{AC-DC} \tag{6.1}$$

where η_L is the efficiency of the link and η_{DC-AC} and η_{AC-DC} are the DC-AC and AC-DC power converter efficiencies.

This chapter aims at providing design guidelines for the efficiency of the link η_L as well as a design-oriented joint circuit-system approach to design a high-efficiency resonant inductive coupling wireless power transfer link embedded in a class E^2 DC-DC converter.

6.2 On Frequency Optimization of RIC WPT Links

Current applications to WPT links are limited to symetric point-to-point-links. New challenges and applications of RIC-WPT emphasize the necessity to explore, predict and optimize the behavior of these links for different configurations: multi-point RIC-WPT networks and assymetrical systems. In this section a design methodology oriented towards the optimization of assymetric RIC-WPT links is presented, resulting in a closed analytical formulation of the optimal frequency at which an assymetrical RIC-WPT link should operate. Finally, the resulting efficiency-optimized link si explored and compared to previous results obtained in RIC-WPT symetric configurations [1][39].

Power transfer efficiency is key in wireless power transfer systems. In particular, in RIC-WPT links, the efficiency of the physical layer strongly depends upon a) the frequency of operation (resonant frequency of the link), b) the losses of the transmitter and receiver coils and c) the mutual inductance between them. Since both the losses and the mutual inductance are frequency-dependant, it is of interest to analyze the optimal frequency at which a given link should operate to maximize its efficiency. This has been previously studied for symetric point-to-point RIC-WPT links[39], but it is still unexplored for assymetrical configurations (different transmitter and receiver sizes), in which the difference between transmitter and receiver minimum-loss frequencies emphasize the need for an optimal system co-designed frequency of operation. In this section, the power transfer efficiency of impedance-matched Assymetric RIC-WPT links is studied in terms of frequency and a closed analytical expression of the optimal frequency of operation is provided. Finally, the System Efficiency of Assymetric Frequency-Optimized RIC-WPT links is analyzed and compared to the Symetric Frequency-Optimized Configuration.

6.2.1 Efficiency in Assymetric RIC-WPT

The power transfer efficiency in RIC-WPT links, defined as the ratio between the power delivered to the load and the total input power, can be expressed as a function of the input frequency ω, the load R_L, transmitter and receiver losses (R_1,R_2), and the mutual inductance between them M_{12} [38]

$$\eta = \frac{R_L(\omega M_{12})^2}{(\omega M_{12})^2(R_2 + R_L) + R_1(R_2 + R_L)^2} \tag{6.2}$$

If impedance matching conditions are fulfilled ($R_L = \sqrt{R_2^2 + (\omega M_{12})^2 R_2/R_1}$, [40]), the efficiency of the system only depends upon the equivalent resistance of the coils (radiative, ohmic and dielectric losses), the mutual impedance between them and the frequency of operation, resulting in:

$$\eta_o = \frac{\sqrt{1 + \left(\frac{\omega M_{12}}{\sqrt{R_1 R_2}}\right)^2} - 1}{1 + \left(\frac{\omega M_{12}}{\sqrt{R_1 R_2}}\right)^2 + 1} = \frac{\sqrt{1 + S_a^2} - 1}{\sqrt{1 + S_a^2} + 1} \tag{6.3}$$

It can be observed in 6.3 that, to maximize efficiency, the relationational factor S_a -which is equivalent to the Coupled mode Theory K/Γ [74]- has to be maximized.

$$S_a = \frac{\omega M_{12}}{\sqrt{R_1 R_2}} \tag{6.4}$$

To accomplish this, it is necessary to 1) Maximize the frequency of the resonators (ω) 2) maximize the mutual inductance between coils (M_{12}) and 3) minimize the transmitter (R_1) and receiver (R_2) losses, which depend upon the technological parameters of the coils and the separation between them as follows:

$$\begin{aligned} M_{12} &= f(N_1, a_1, N_2, a_2, D_{12}) \\ R_1 &= f(\omega, N_1, a_1, b_1, c_2, \sigma_1) \\ R_2 &= f(\omega, N_2, a_2, b_2, c_2, \sigma_2) \end{aligned} \tag{6.5}$$

where two circular loop antennas with $N_{1,2}$ turns, coil diameters $a_{1,2}$, wire radius $b_{1,2}$, inter-turn separation $c_{1,2}$, conductivity $\sigma_{1,2}$ and a distance D_{12} between them, have been assumed.

To maximize the efficiency, the frequency should be chosen so that S_a is maximized (highest frequency, maximum mutual inductance and minumum coil's losses). In the forecoming sections, the mutual inductance as well as the coil's losses are derived for N-turn circular loop antennas.

6.2.1.1 Mutual Inductance

In the quasi-static limit, at large distances ($D_{12} >> a_1$) the magnetic flux density at the receiver coil as a result of the transmitter coil has the form of a dipole [2].

$$B_{12} \simeq \frac{\mu_0}{2} \frac{N_1 i a_1^2}{D_{12}^3} \tag{6.6}$$

where coaxial orientation between coils has been assumed. The mutual inductance is then found froum the flux through the N_2 linkages in the receiver coil:

$$M_{12} = N_2 \frac{\partial \Psi_{12}}{\partial i} \simeq \frac{\pi}{2} N_1 N_2 \mu_0 \frac{a_1^2 a_2^2}{D_{12}^3} \tag{6.7}$$

6.2.1.2 Evaluation of Losses

The losses of the resonators depend upon their constituent materials $(\sigma_{1,2}, \delta_{1,2})$ and geometry $(a_{1,2}, b_{1,2}, c_{1,2})$ and can be divided into Radiative Losses (R_r), Ohmic Losses (R_o) and Dielectric Losses (R_d):

$$R_1 = R_r^1 + R_o^1 + R_d^1 \tag{6.8}$$

In this section, the losses of two electrically small $(a << \lambda)$ circular loop antennas (chosen for their low radiation resistance [42]) are considered.

The radiation losses of a circular N_1-turn loop antenna with loop radius a_1 can be found by [2]:

$$R_r^1 = 20\pi^2 N_1^2 a_1^4 \frac{\omega^4}{c_o^4} \tag{6.9}$$

The ohmic resistance, which is in general much larger than the radiation resistance, depends upon the proximity effect (if the spacing between the turns in the loop antenna is small) and the skin effect. The total ohmic resistance for an N_1-turn circular loop antenna with loop radius a_1, wire radius b_1 and loop separation $2c_1$ is given by [2]:

$$R_o^1 = \frac{N_1 a_1}{b_1} R_s^1 \left(\frac{R_p^1}{R_0^1} + 1 \right) \tag{6.10}$$

where $R_s^1 = \sqrt{\omega\mu_0/2\sigma_1}$ is the surface impedance of the conductor and R_p^1 is the ohmic resistance per unit length due to proximity effect.

Finally, if a dielectric loop antenna is considered, the dielectric losses are given by:

$$R_d^1 = \frac{\tan\delta_1}{\omega C_1} = \omega L_1 \tan\delta_1 \simeq \omega 4\mu_0 a_1 N_1^2 \tan\delta_1 \tag{6.11}$$

where $\tan\delta_1$ is the loss tangent of the coil and L_1 has been approximated to $L_1 = 4\mu_0 a_1 N_1^2$. Defining the ratios of assymetry in number of turns (u_N), antenna diameter (u_a), wire radius (u_b), inter-turn distance (u_c), conductivity (u_σ) and loss tangent (u_δ) as follows:

$$\begin{aligned} u_N &= \frac{N_2}{N_1}; \quad u_a = \frac{a_2}{a_1}; \quad u_b = \frac{b_2}{b_1} \\ u_\sigma &= \frac{\sigma_2}{\sigma_1}; \quad u_c = \frac{c_2}{c_1}; \quad u_\delta = \frac{\delta_2}{\delta_1} \end{aligned} \tag{6.12}$$

the losses at the receiver (assuming $u_\delta = u_c = 1$) can be expressed as:

$$R_2 = R_r^2 + R_o^2 + R_d^2 = u_N^2 u_a^4 R_r^1 + \frac{u_N u_a}{u_b\sqrt{u_\sigma}} R_o^1 + u_a u_N^1 R_d^1 \tag{6.13}$$

6.2.2 Frequency Optimization of Assymetric RIC-WPT

6.2.2.1 Optimal Frequency

To find the optimal frequency at which the Assymetric RIC-WPT link should operate, it is necessary to take the derivative of S_a with respect to ω. To do this, the losses in the transmitter coil are expressed as:

$$\begin{aligned} R_r^1 &= C_r^1\omega^4; \quad & C_r^1 &= \frac{20\pi^2 N_1^2 a_1^4}{c_o^4} \\ R_o^1 &= C_o^1\sqrt{\omega}; \quad & C_o^1 &\simeq \frac{N_1 a_1}{b_1}\sqrt{\frac{\mu_0}{2\sigma_1}} \\ R_d^1 &= C_d^1\omega; \quad & C_d &\simeq 4\mu_0 a_1 N_1^2 \tan\delta_1 \end{aligned} \tag{6.14}$$

where C_r^1, C_o^1 and C_d^1 are the frequency-independent cofficients corresponding to the radiation, ohmic and dielectric losses respectively. Similarly, the losses at the receiver coil can be defined as:

$$\begin{aligned} R_r^2 &= C_r^2\omega^4; \quad & C_r^2 &= K_r C_r^1; \quad & K_r &= u_N^2 u_a^4 \\ R_o^2 &= C_o^2\sqrt{\omega}; \quad & C_o^2 &= K_o C_o^1; \quad & K_o &= \frac{u_N u_a}{u_b\sqrt{u_\sigma}} \\ R_d^2 &= C_d^2\omega; \quad & C_d^2 &= K_d C_d^1; \quad & K_d &= u_a u_N^2 \end{aligned} \tag{6.15}$$

where K_r, K_o and K_d model the effect of the assimetries between transmitter and receiver upon the receiver's losses. Finally, the mutual inductance can be expressed as a function of the equivalent mutual inductance obtained in a symetric link ($u_{N,a,b,c,\sigma,\delta} = 1$) as:

$$M_{12}^a = K_m M_{12}; \quad K_m = u_N u_a^2; \tag{6.16}$$

Once this is known, both the mutual inductance (6.16) and the transmitter and receiver losses (6.14,6.15) can be substituted in equation 6.4 resulting in:

$$S_a = \frac{\omega K_m M_{12}}{\sqrt{(C_r^1\omega^4 + C_o^1\sqrt{\omega} + C_d^1\omega)(K_r C_r^1\omega^4 + K_o C_o^1\sqrt{\omega} + K_d C_d^1\omega)}} \tag{6.17}$$

which is then be derived with respect to ω to obtain the optimal frequency at which the assymetric link should operate. The resulting ω_o^a is the solution of:

$$\begin{aligned} 6\omega^7 C_R^2 K_r + 6\omega^4 C_d C_r\left(\frac{K_d + K_r}{2}\right) + 5\omega^{\frac{7}{2}} C_o C_r\left(\frac{K_o + K_r}{2}\right) \\ -\omega^{\frac{1}{2}} C_d C_o\left(\frac{K_o + K_d}{2}\right) - K_o C_o^2 = 0 \end{aligned} \tag{6.18}$$

For illustration purposes and in order to achieve a closed analytical formulation, dielectric-less transmitter and receiver coils are assumed ($C_d^1 = C_d^2 = 0$), obtaining:

$$\omega_{opt}^a = K_w \omega_{opt} \tag{6.19}$$

where:

$$K_w = \left(\frac{(K_o + K_r)}{K_r} \left[\sqrt{\frac{25}{16} + \frac{6K_oK_r}{(K_o + K_r)^2}} - \frac{5}{4} \right] \right)^{\frac{2}{7}} \tag{6.20}$$

and ω_{opt} is the optimal frequency corresponding to a symmetric link ($u_{N,a,b,c,\sigma,\delta} = 1$):

$$\omega_{opt} = \left(\frac{C_o^1}{6C_r^1} \right)^{\frac{2}{7}} \tag{6.21}$$

6.2.2.2 Maximum Efficiency

Once the optimal frequency at which the link should operate is obtained, the maximum relational factor S_a and the resulting maximum efficiency η_{max}^a can be found by substituting ω by ω_{opt} in 6.4:

$$S_a^{max} = S^{max} \frac{7K_m\sqrt{K_w}}{\sqrt{K_rK_w^7 + 6K_w^{\frac{7}{2}}(K_o + K_r) + 36K_o}} \tag{6.22}$$

where S^{max} is the maximum relational factor S for a symetric link:

$$S^{max} = \frac{6M}{7C_o^1} \left(\frac{C_o^1}{6C_r^1} \right)^{\frac{1}{7}} \tag{6.23}$$

and the maximum power transfer efficiency is then obtained by:

$$\eta_a^{max} = \frac{\sqrt{1 + (S_a^{max})^2} - 1}{\sqrt{1 + (S_a^{max})^2} + 1} \tag{6.24}$$

6.2.3 Results

The results obtained above regarding the optimal frequency of the assymetric link, the maximum relational factor $S_{a,max}$ and the corresponding maximum efficiency $\eta_{s,max}$ are illustrated below. First, the normalized frequency deviation due to the link assymetry is shown in figure 6.1:

$$\Delta w = \frac{w_o^a - w_o^s}{w_o^s} = k_w - 1 \tag{6.25}$$

where $k_w = f(K_o, K_r)$ as per equation 6.20. It can be observed that, when the assymetry between transmitter and receiver represents around a 40% of difference either in the radiation or the ohmic losses, the optimal frequency of operation for the assymetric link experiments a 20% deviation from the optimal frequency in the symetric link, showcasing the impact of this study. When assessing the effect of the assymetry in RIC-WPT links, it is also of interest to study how this assymetry (described in a compressed manner by the coefficients K_r, K_o and K_m) affects S_{max} and the maximum achievable efficiency. To do this, figure 6.2.3 illustrates the obtained S_{max} for different K_o/K_r and C_o/C_r coefficients as a function of frequency,

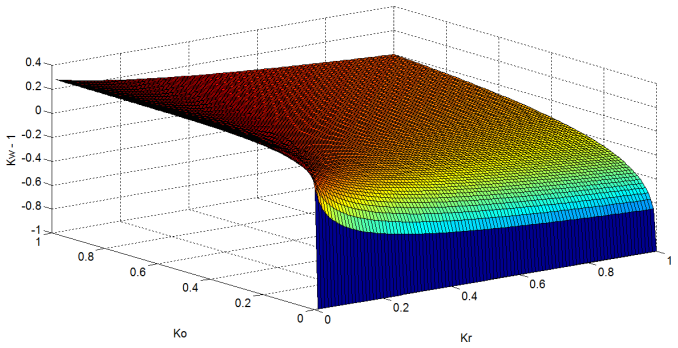

Figure 6.1: Normalized Frequency Deviation (Δw) with $C_o/C_r = 0.05$

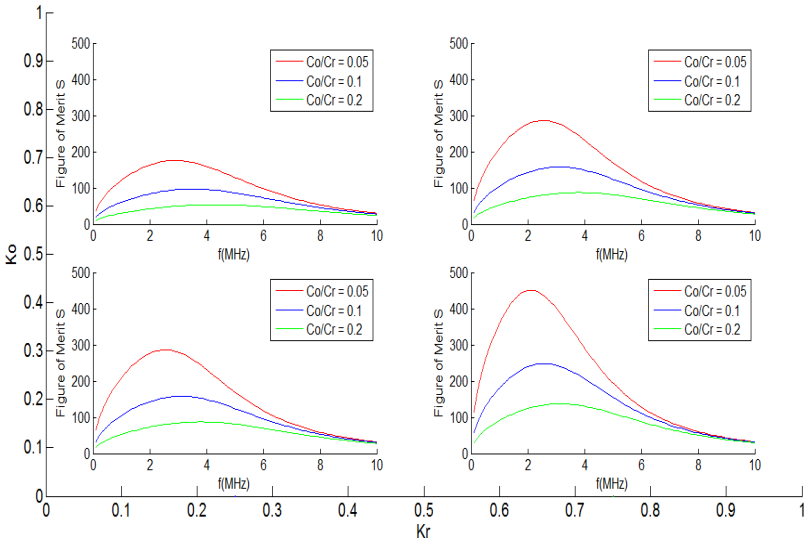

Figure 6.2: S^a_{max} study for different K_o, K_r configurations.

where the frequency deviation explained in figure 6.1 can be observed. Finally, figure 6.2.3 shows the resulting maximum efficiency ($\eta^a_{max} = \eta^a|_{w=w^a_{opt}}$) normalized with respect to the symetric link maximum efficiency ($\eta^a_{max} = \eta^a|_{w=w^s_{opt}}$)

The efficiency of Assymetric RIC-WPT systems has been studied and presented in this chapter, together with a closed analytical formulation for optimal frequency in RIC-WPT Assymetric links. Finally, the scalability of Assymetric Frequency-Optimized RIC-WPT Links has been assessed and benchmarked with Symetric Frequency-Optimized RIC-WPT links.

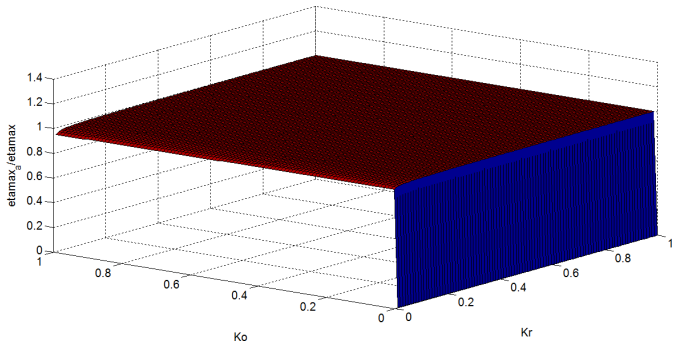

Figure 6.3: Normalized Maximum Efficiency for different K_o, K_r configurations. $C_o/C_r = 0.05$

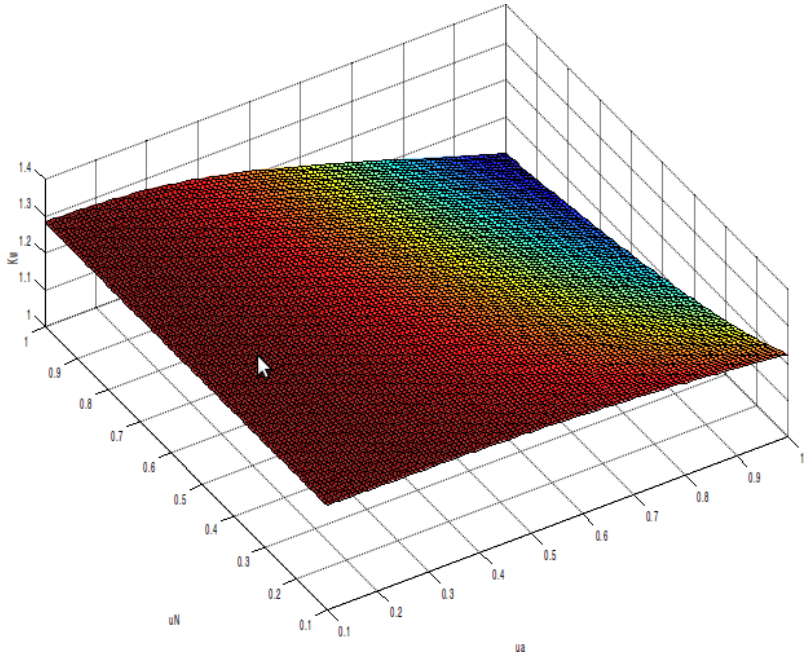

Figure 6.4: Optimal Frequency in Assymetric Links, normalized to 10MHz

6.3 On Antennae Optimization for RIC WPT Links

6.3.1 Coil Design - Number of Turns

Because the maximum achievable efficiency under impedance matching conditions depends only on the geometry of the coils and the frequency at which the system is fed, it makes sense to ask what is the optimal number of turns to maximize S for a given ω.

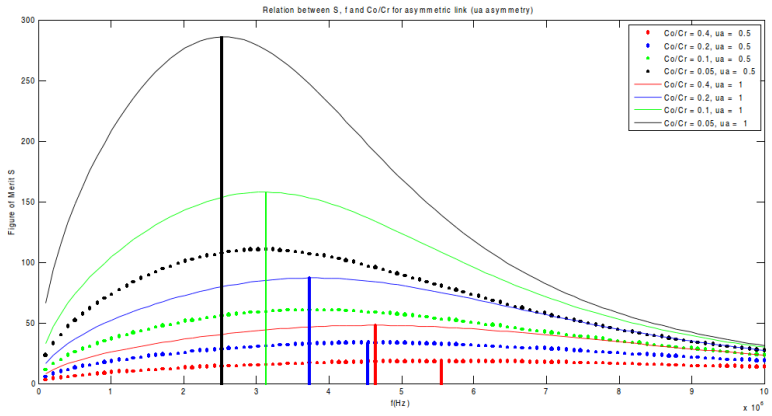

Figure 6.5: Optimal Frequency in Assymetric Links, normalized to 10MHz

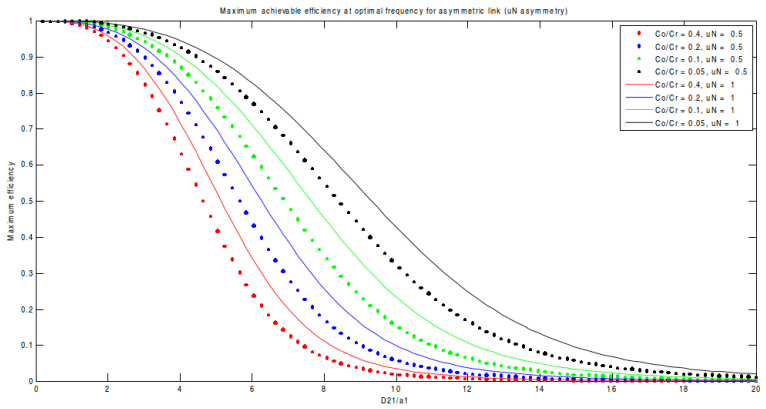

Figure 6.6: Maximum Efficiency - N assymetry

Therefore, derivating S over N, we obtain:

$$\frac{\partial S}{\partial N} = \frac{\partial}{\partial N} \frac{M' N \omega}{N(C'_d \omega + C'_r \omega^4) + C'_o \sqrt{\omega}} \tag{6.26}$$

where

$$\begin{aligned} M' &= M/N^2 \\ C'_d &= L \tan\delta / N^2 = C_d / N^2 \\ C'_o &= C_o / N \\ C'_r &= C_r / N^2 \end{aligned} \tag{6.27}$$

Which shows that there is no N that maximizes or minimizes S. However, the S parameter function has a limit at:

$$S_{N \to \infty} = \frac{M'}{\omega^3 C'_r + C'_d} \tag{6.28}$$

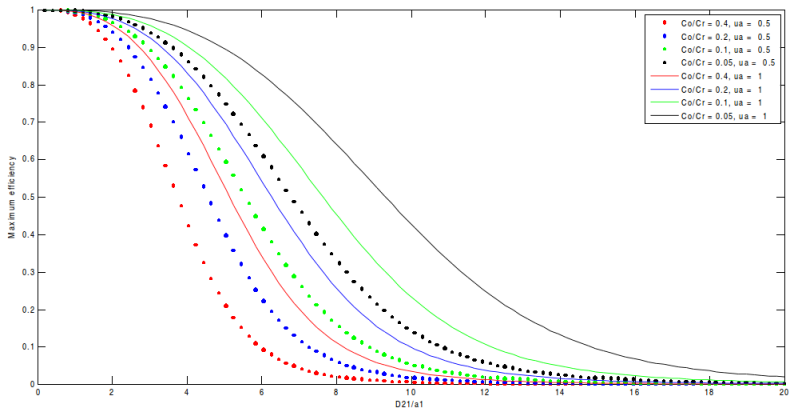

Figure 6.7: Maximum Efficiency - A assymetry

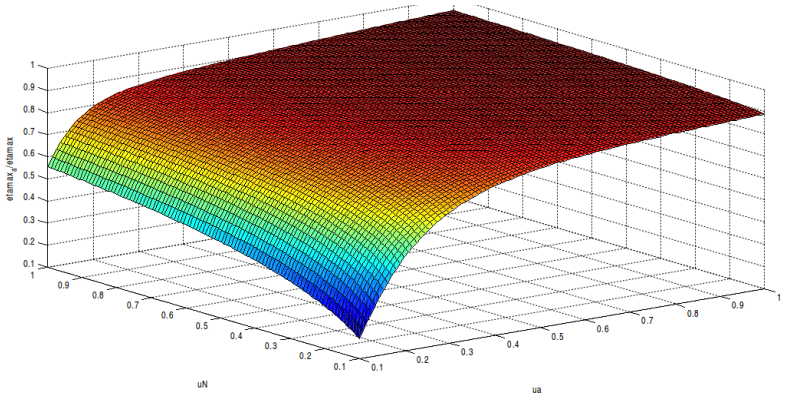

Figure 6.8: Normalized Maximum Efficiency

which means that there is a number of turns from which the S parameter and the efficiency stop increasing.

In figure (6.3.1), the obtained S factor for an impedance-matched system fed with non-optimal frequency ($\omega = 10$MHz) is shown. It can be seen that the S function approximates the limit given in 6.28 and that the function moves quicker to this value when Co/Cr is reduced. Therefore, a lower number of turns will be needed to achieve maximum S if Co/Cr is reduced.

It is also interesting to find the number of turns that maximize S when the system is fed with optimal frequency. It is important to note that optimal frequency depends on C_o/Cr which is proportional to $N^{-2/7}$. Therefore rewriting ω as a function of N:

$$\omega = \omega_o = \left(\frac{C_o}{C_r}\right)^{\frac{2}{7}} = \left(\frac{C'_o}{C'_d}\right)^{\frac{2}{7}} N^{-\frac{2}{7}} = \omega'_o N^{-\frac{2}{7}} \tag{6.29}$$

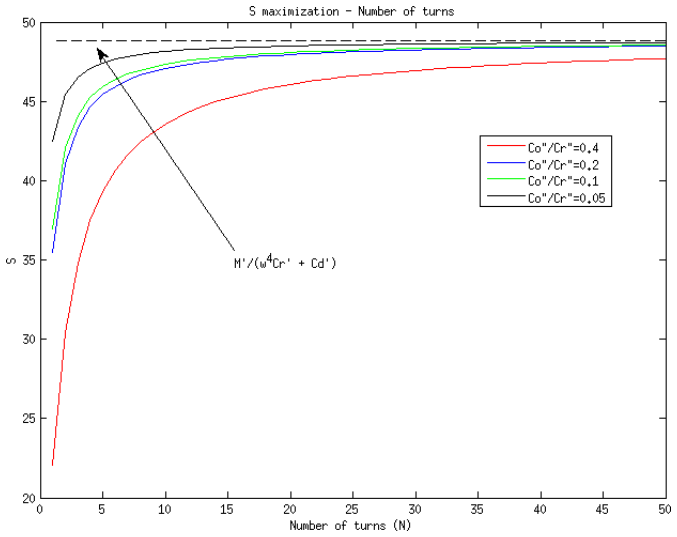

Figure 6.9: S parameter for a system fed with $\omega = 10MHz$ over N for different Co/Cr ratios.

and substituting ω for $\omega'_o N^{-2/7}$ in S function, we obtain:

$$S = \frac{\omega'_o M' N^{\frac{5}{7}}}{N^{\frac{5}{7}}\omega'_o C'_d + N^{-\frac{1}{7}}(C'_r\omega'^4_o + C'_o\sqrt{\omega'_o})} = \frac{\omega'_o M' N}{N\omega'_o C'_d + N^{\frac{1}{7}}(C'_r\omega'^4_o + C'_o\sqrt{\omega'_o})} \tag{6.30}$$

Similarly as before, there isn't an optimal value of N that maximizes S but the function is limited. The limit of S when $N \to \infty$ if optimal frequency is used is:

$$S_{N\to\infty} = \frac{M'}{C'_d} = \frac{M}{C_d} \tag{6.31}$$

In figure 6.3.1, the S function for two impedance matched coils fed with optimal frequency is shown. It can be observed that the limit of S has been increased when compared with the one obtained in 6.3.1 but not significantly because $C_r\omega^3$ was negligible in equation 6.28.

6.3.2 Loss Reduction: SuperConducting Coils

Recently, some models to increase power transfer efficiency (and therefore the achievable distance) through the evaluation and reduction of the resistive losses (increase in Q-factor) have been developed [1] [39], which will extend the RIC efficient wireless power transfer from several meters to hundreds of meters. In a dielectric-less superconducting coil, the ohmic losses would be negligible and therefore the radiative losses will dominate:

$$S_s = \frac{\omega M}{\sqrt{\omega}C_o + \omega^4 C_r + \omega C_d} \simeq \frac{\omega M}{\omega^4 C_r} = \frac{\mu_0 c_o^4}{40\pi D^3 \omega^3} \tag{6.32}$$

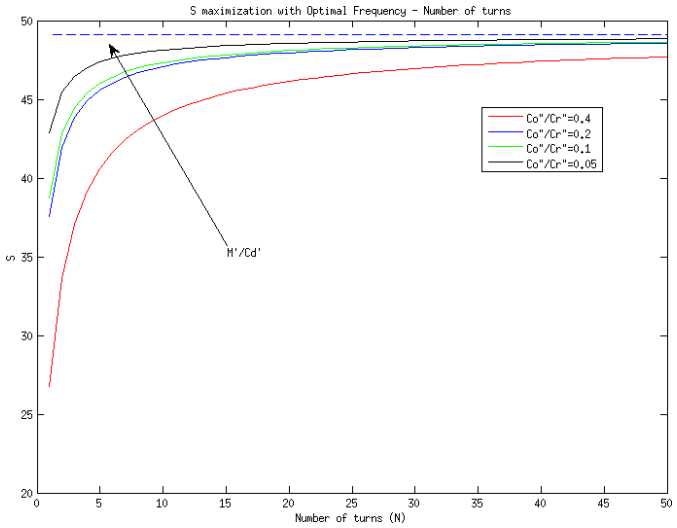

Figure 6.10: S parameter for a system fed with $\omega = \omega_o$ over N for different Co/Cr ratios.

Which doesn't depend on the number of transmitter and receiver coils turns but it does on frequency. In this case, there is no optimal frequency but it should be as low as possible in order to minimize radiative losses and increase S.

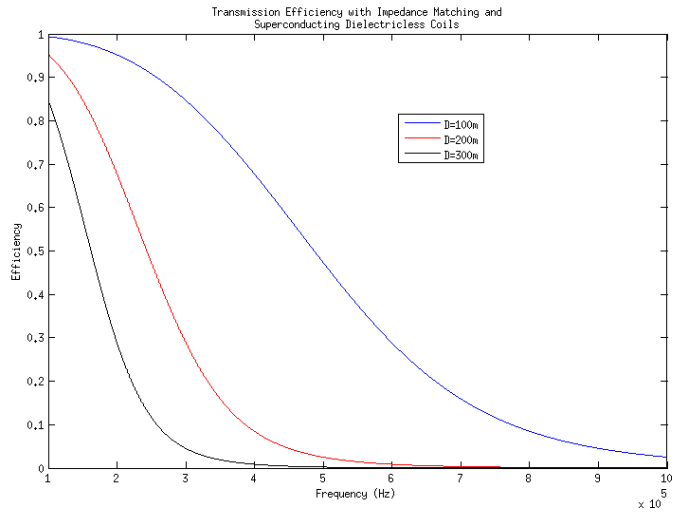

However, these solutions involve the use of high temperature superconducting (HTS) wire which substantially increases the resulting size of the coil and complexity of the systems.

6.3.3 Reduction of losses: Litz Wires

Litz wires are commonly used in the manufacture of inductors and transformers in order to minimize the skin and proximity effects that increase the resistance of the system. Litz wires allow to decrease the ohmic resistance of the coils (increase their Q factor) when resonant frequencies up to 1-2 MHz are used [84] [32] by using individually insulated strands. Also, it is possible to find the optimal number of wire strands in a Litz-wire transformer [85].

6.3.4 Reduction of losses: Dielectric-less Coils

If a dielectric-less coil is considered ($C_d = 0$) then we can rewrite equations 6.30 and 6.34 to:

$$S_{nd} = \frac{\omega'_o M' N^{\frac{6}{7}}}{C'_r \omega'^4_o + C'_o \sqrt{\omega'_o}} \tag{6.33}$$

$$S_{N\to\infty} = lim_{N\to\infty} \frac{M' N^{\frac{6}{7}}}{C'_r \omega'^4_o + C'_o \sqrt{\omega'_o}} = \infty \tag{6.34}$$

And operating 6.33 using equations 6.19, 6.45 and 6.27 we obtain:

$$S_{max} \simeq \frac{34212\mu_0}{D^3} \left(a^3 b N \sqrt{\frac{2\sigma}{\mu_0}} \right)^{\frac{6}{7}} \tag{6.35}$$

Where it can be seen that to maximize S, the number of turns of the coils should be maximized too. In figure 6.3.4, the relation between S and N for a dielectric-less coil with optimal frequency is explored, showing that the S parameter is, in this case, unlimited.

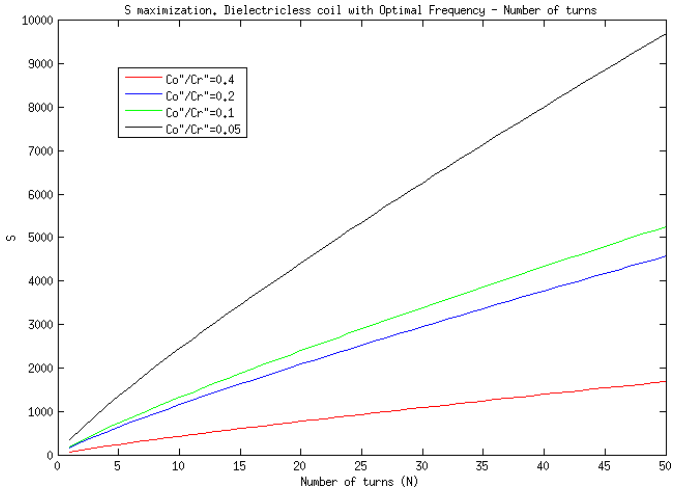

Figure 6.11: S parameter for a Dielectric-less Coil with optimal frequency over number of turns (N)

Figure 6.12 shows the behavior of the merit factor S over distance between transmitter and receiver coils upon impedance matching, optimal frequency and dielectric-less conditions for different number of turns (N). It is important to note that while the efficiency at $D \simeq 0$ does not increase (arrives at a maximum of 100%) the addition of turns increases the magnetic field of the coil and therefore the mutual inductance, allowing to maintain better efficiency values at higher distances.

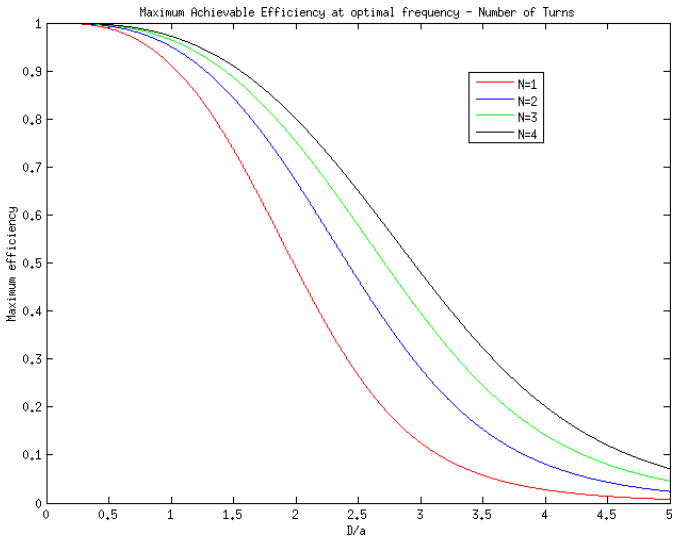

Figure 6.12: Relation between S and Distance (D/a)

6.4 Class E^2 RIC-WPT Link: A design-oriented joint circuit-system approach

Due to the behavior of the resonant inductive coupling link, the wireless power transfer system has to be co-designed together with the power electronics front-end, thereby requiring of a design-oriented joint circuit-system co-characterization approach. Additionally, key for designing such a WPT link there is the need of modeling and characterizing the relationships between low-level circuit and subsystem intrinsic behavior up to high-level system performance, in face of conflicting requirements such as lower mass, maximum power transferred to the load and maximum efficiency, building a translayer bridge between different system levels. In this section we propose a high-efficiency class E^2 WPT link, demonstrate how to system co-design a resonant inductive coupling WPT link together with the power electronics front-end targetting certain behavior thresholds and requirements with a given set of design constraints and present the results obtained using this approach.

6.4.1 System Design

In order to achieve high efficiency DC-DC wireless power transfer, it is necessary to design a system that combines a low loss wireless power link as well as an electronic front-end with high power conversion efficiency: a class E inverter at the transmitter and a class E rectifier at the receiver, both achieving zero-voltage switching and zero-derivative switching (ZVS/ZDS) at turn-on/turn-off instants. With this goal, a class E^2 Resonant Inductive Coupling Wireless Power Transfer link (shown in figure 6.13) is proposed in this section.

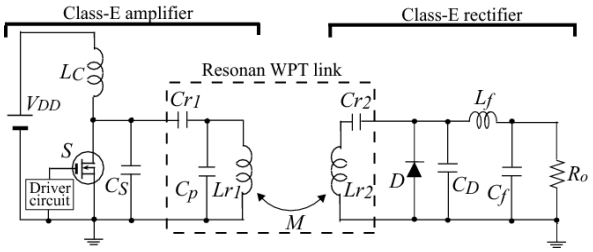

Figure 6.13: Class E^2 WPT System Diagram

System analysis/design techniques have been used to divide the final system and requirements to be met in subsystem elements, which could be analyzed separately but need to be optimized jointly. Connecting system-level performance models can be particularly complex because of the interplay between the WPT link and the power electronics. Therefore this problem has been analyzed similarly to circuit and system co-design optimization framework [86]. By the use of system/design methodology, the wireless power transfer system is divided in two subsystems: the wireless power link (transmitter and receiver coils and associated magnetic field distribution) and the power electronics front-end (inverter and rectifier). Both subsystems have been modeled and expressed in terms of their design variables and then condensed in a figure of merit that compresses the requirements of the designed system.

6.4.1.1 Figure of Merit

For illustration purposes, the selected figure of merit of the complete system combines the performance metrics specified below:

- Provide an output power of 1W with a regulated 5V when the distance between transmitter and receiver is $D = 50cm$. $P1 = 2$.
- Maximize the power transfer efficiency at 1m.
  $P2 = 6 \times \eta_T$ (max 3p).
- Minimize the mass of the system.
  $P3 = 1.5/w_T$ (max 3p).

- Maximize the distance at which the regulated output is achieved. $P4 = 1.5 \times (D - 0.5)$. (max 2p).

These performance metrics are then united into the figure of merit, which has a maximum value of 10.

$$P_T = P_1 + P_2 + P_3 + P_4 \tag{6.36}$$

To design the WPT System, two metrics should be observed: the total DC-DC efficiency and its mass.

$$\eta_T = \eta_I \times \eta_L \times \eta_R; \quad w_T = w_I + w_L + w_R \tag{6.37}$$

where η_T is defined as the DC-DC efficiency of the system, η_I, w_I are the efficiency and mass of the class E inverter, η_L, w_L are the efficiency and mass of the link and η_R, w_R the rectifier efficiency and mass.

6.4.1.2 Design Variables

Two levels of design variables are identified: the design variables that are enclosed within a given subsystem (inverter, link, rectifier) and the design variables that have a cross-system impact. While the behavior of most of the RIC-WPT link design variables can be constrained within the subsystem and therefore optimized locally, others such as the frequency of operation affect both the power electronics and the link, therefore requiring a system analysis and co-design. Table 6.1 shows the design variables, where subindexs, L,I and R indicate that the variable belongs to the link, inverter and rectifier respectively.

Subsystem-specific	System-Wide
N_L: Number of turns of the coils	f_L: Link frequency
a_L: Coil Diameter	f_I: Inverter frequency
b_L: Wire Diameter	f_R: Rectifier frequency
c_L: Separation between turns	
σ: Conductivity of the material	
δL: Density of the material	

Table 6.1: Subsystem and System Design Variables

Once the design variables are known, the subsystem metrics can be expressed as a function of these design variables:

$$\begin{array}{ll} \eta_L(N_L, a_L, b_L, c_L, \sigma, f_L) & w_L(N_L, a_L, b_L, \delta_L, f_L) \\ \eta_I(f_I); w_I(f_I) & \eta_R(f_R); w_R(f_R) \end{array} \tag{6.38}$$

where $f_L = f_I = f_R$ is the frequency of operation of the system, which has to be optimized across layers.

6.4.2 Wireless Power Transfer Link

Regarding the resonant inductive coupling wireless link, the transmitter and receiver coils have to be designed together with the required capacitances to make them resonate at the selected operating frequency. The transmitter and receiver coils, which are considered equal for simplicity, will be made of copper ($\sigma = 5.96 \times 10^7 Sm^{-1}$ and $\delta_L = 8.96 gcm^{-3}$).

6.4.2.1 Wireless Power Transfer Efficiency

If the system is impedance matched for maximum power transfer efficiency (load resistance adjusted for a given distance and coupling between transmitter and receiver) [40], the maximum efficiency can be then expressed as:

$$\eta_{L,max} = \frac{\sqrt{1 + \left(\frac{\omega_L M_L}{R_L}\right)^2} - 1}{\sqrt{1 + \left(\frac{\omega_L M_L}{R_L}\right)^2} + 1} \tag{6.39}$$

From equation 6.39 it can be seen that to maximize the achievable efficiency it is necessary to maximize $\frac{\omega_L M_L}{R_L}$ where M_L is the mutual inductance of the coils, ω_L is the frequency at which the system operates and R_L the sum of the coils losses (ohmic, radiative and dielectric).

Losses can be divided into radiative (R_r), ohmic (R_o) and dielectric (R_d).

$$\begin{aligned} R(a_L, b_L, c_L, N_L, f_L, \sigma) = R_r(a_L, N_L, f_L) + \\ R_o(a_L, b_L, c_L, N_L, f_L, \sigma) + R_d(f_L, \delta_L) \end{aligned} \tag{6.40}$$

The radiative losses are caused by the radiation of electromagnetic waves from the transmitter and receiver. The radiation resistance of circular and square N-loop antennas can be found from [2] to be:

$$R_r(a_L, N_L, f_L) = 320 \left(\frac{\pi^2 N_L A}{\lambda_L^2}\right)^2 \tag{6.41}$$

where A is the perimeter of the coil, being equal to $A_c = \pi a_L^2$ for circular loop antennas and $A_s = (2a_L)^2$ for square loop antennas. The ohmic resistance, which is in general much larger than the radiation resistance, depends upon two factors: the proximity effect (if the spacing between the turns in the loop antenna is small) and the skin effect. The total ohmic resistance for an N-turn circular loop antenna with loop radius a, wire radius b and loop separation $2c$ is given by [87]:

$$R_o(a_L, b_L, c_L, N_L, f_L, \sigma) = \frac{N_L a_L}{b_L} R_s \left(\frac{R_p}{R_0} + 1\right) \tag{6.42}$$

where $R_s = \frac{\omega \mu_0}{2\sigma}$ is the surface impedance of the conductor, R_p is the ohmic resistance per unit length due to the proximity effect and $R_0 = \frac{N R_s}{2\pi}$ is the ohmic skin effect

resistance per unit length. It is important to note that for close spacing, the ohmic resistance is twice as large as that in absence of proximity effect ($R_p/R_0 = 0$). Finally, if a dielectric antenna is considered, the dielectric losses can be defined as:

$$R_d(f_L, \delta_L) = \omega_L L \tan \delta_L \tag{6.43}$$

where L is the coil inductance and $\tan \delta$ is the loss tangent of the coil.

Mutual inductance is defined as the ratio of the electromagnetic field induced in the secondary coil to the rate of change of electric current in the primary coil. In the quasi-static limit and at large distances ($D >> a$) the magnetic flux density at the second coil as a result of the first has the form of a dipole [1]:

$$B = \frac{\mu_0 N i A}{4\pi D^3} sqrt1 + 3\sin^2\theta \simeq \frac{\mu_0 N i a^2}{2D^3} \tag{6.44}$$

where coaxial orientation of the coils has been assumed. The mutual inductance is then found from the flux through the N linkages of the second coil as:

$$M(N_L, a_L) = N_L \frac{\partial \Psi}{\partial i} \simeq \frac{\pi}{2} N_L^2 \mu_0 \frac{a_L^4}{D^3} \tag{6.45}$$

where μ_0 is the free-space permeability and D is the distance between transmitter and receiver antennas.

Frequency of operation: Although it is possible to find the optimal frequency of the WPT link[39], the frequency of operation is a system-wide variable that should not be optimized locally.

6.4.2.2 Mass

The mass of the wireless power link depends upon the geometry of the coils as well as the supporting structure. The WPT link mass is found by:

$$w_L(a_L, b_L, N_L) = 2(4\pi \rho_{cu} N_L a_L b_L^2 + w_s) \tag{6.46}$$

where w_s is the mass of the supporting structure.

6.4.2.3 Results

From the equations obtained, several design decisions can be taken at subsystem level. First, since a required efficiency of 10% was considered necessary to maintain the power output at 1.8m (maximum distance), a diameter of the coils of $a_L = 0.4m$ was selected, as shown in 6.14. Secondly, the wire diameter was decided based upon availability of the material to be $b_L = 0.16mm$. To minimize losses and mass, dielectric-less coils were considered ($R_d = 0$) and to minimize proximity effect losses, a separation between turns of $c_L = 3b_L$ was stablished.

Using these results, the WPT link efficiency and mass performance metrics were simplified to:

$$\begin{gathered} \eta_L(a_L, b_L, c_L, N_L, f_L, \sigma) \rightarrow \eta_L(N_L, f_L) \\ w_L(a_L, b_L, c_L, N_L, \delta_L, f_L) \rightarrow w_L(N_L, f_L) \end{gathered} \tag{6.47}$$

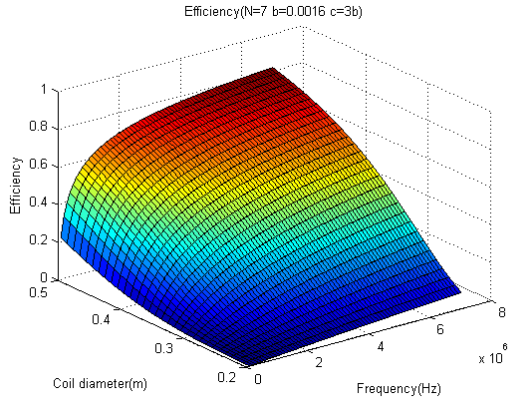

Figure 6.14: Efficiency of the WPT link at 1.8m

6.4.3 Power Electronics Front-End

To obtain the efficiency and mass of the class E^2 DC-DC power electronics system, the inverter and rectifier components were dimensioned for the operating frequencies of the resonant inductive coupling wireless power transfer link (1-10MHz) and simulated. To select these components, a coupling between coils of $k = 0.0087$ (intermediate distance of 1 meter) and a coil inductance of $L_1 = L_2 = 50\mu$H were suposed. The performance metrics of the power electronics frontend are:

$$\eta_I(f); \quad w_I(f); \quad \eta_R(f); \quad w_R(f) \tag{6.48}$$

6.4.3.1 Efficiency

The required components to achieve class E switching conditions have been selected for the frequencies between 1 and 10MHz and then simulated using SPICE to obtain the efficiency of the inverter and rectifier circuits.

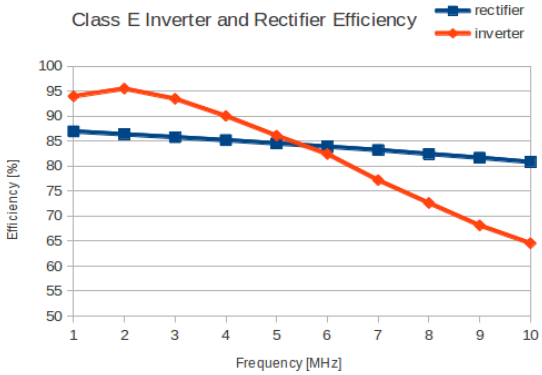

Figure 6.15: Class E Rectifier and Class E Inverter Efficiency

To do this, Finite Element Field simulations of the WPT link have been performed at the specified frequency range and the equivalent output and input impedance of the link has been added to the simulation profile.

6.4.3.2 Mass

The same procedure has been applied to obtain the mass of the system. The required values to achieve class E switching conditions were obtained and then the resulting mass was calculated from the commercial components.

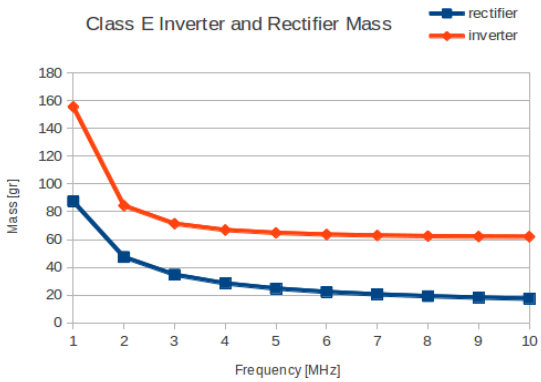

Figure 6.16: Class E Rectifier and Class E Inverter Mass

6.4.4 Results

Once the performance metrics of both subsystems are known it is possible to calculate the overall system results regarding the DC-DC power transfer efficiency and mass. Since the wireless link performance metrics were compressed into two variables (N_L and f_L) and the power front-end performance metrics were considered only as a function of the frequency of operation ($f_i = f_r = f_l$), the resulting performance metrics can be explored in terms of N_L and f. Figures 6.4.4 show this design space exploration.

Finally, the resulting figure of merit defined in equation 6.36 is plotted in terms of N_L and f in figure 6.18.

Figure 6.18 shows that the FOM is maximized at an operating frequency of 5.5MHz together with an optimal number of turns of $N_L = 7$. With this information, the transmitter and receiver coils can be designed and simulated using a Finite ELement Field Solver. Figure 6.4.4 shows a Finite Element Field Simulation of the magnetic fields of the designed coils at $D = 1m$ and $D = 1.8m$.

Once the frequency and number of turns are known, we can re-calculate the required components to achieve class E switching conditions at both the inverter and the rectifier. Due to the nature of the Resonant Inductive Coupling Wireless

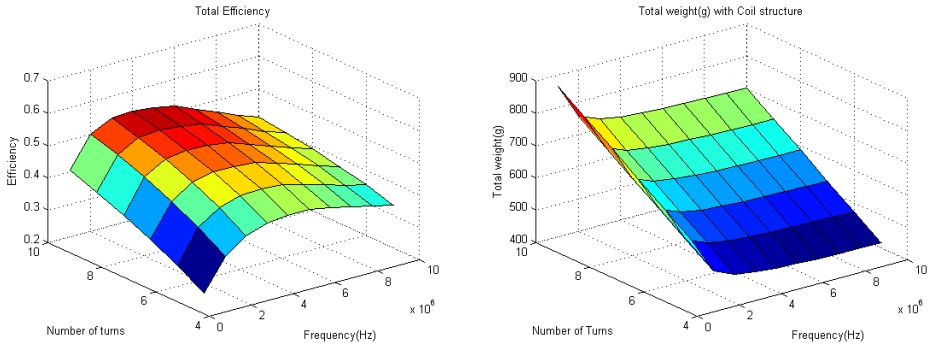

(a) DC-DC System Efficiency at $D = 0.5m$ (b) System Mass

Figure 6.17: Performance Metrics

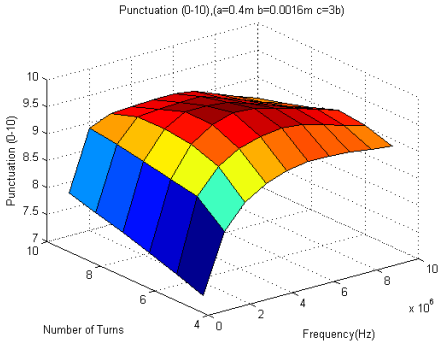

Figure 6.18: Figure of Merit

Power Transfer link, three different sets of components had to be chosen for the three operational distances of the link, namely: $d = 0.5m$, $d = 1m$ and maximum achievable distance $d = 1.8m$. This is due to the fact that the reflected impedance of the link is modified with distance (depends on the mutual inductance $(M(D))$ and therefore, the necessary values to achieve zero-voltage/zero-derivative switching conditions have to be adjusted accordingly. To select the required components, the mutual inductance as well as the impedance of the coils have been obtained using a Finite Element Field Solver for the three distances and added to the SPICE model. Table 6.2 shows the resulting values for each distance. Finally, the total mass of the system can be found to be 0.750kg and the efficiencies at the three different operating distances are shown in table 6.3, obtaining a FOM of 9/10.

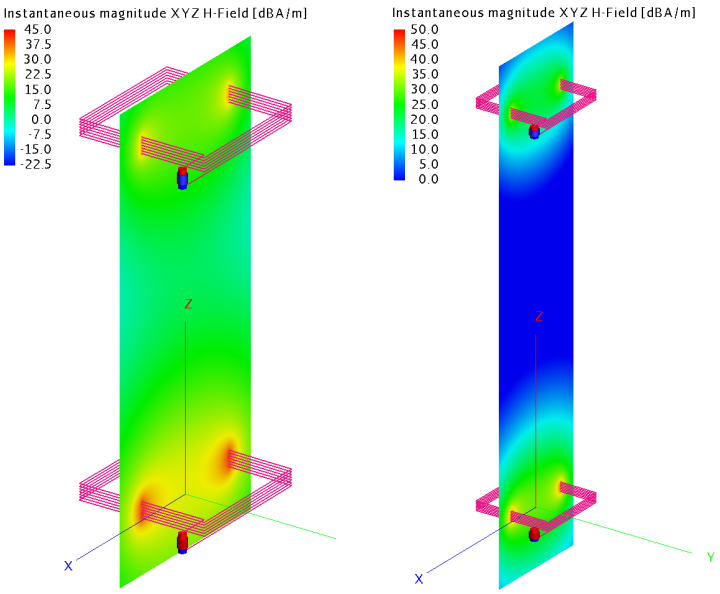

(a) $D = 1m$ (b) $D = 1.8m$

Figure 6.19: FEKO Magnetic Field of the WPT Link at $D = 1m$ and $D = 1.8m$

Amplifier	$d = 0.5$m	$d = 1.0$m	d= 1.833m
L_C	827μH	217μH	34.8μH
S(MOSFET)	SUD06N10225LE3	-	-
C_s	8.08pF	30.8pF	192pF
C_{r1}	9.18pF	3.92pF	4.59pF
C_p	0pF	5.12pF	4.44pF
Rectifier			
C_{r2}	9.05pF	9.05pF	9.05pF
D(Diode)	ZHCS1000	-	-
C_D	25pF	25pF	25pF
L_f	31.5μH	31.5μH	31.5μH
C_f	0.47μF	0.47μF	0.47μF

Table 6.2: Selected components Class E Inverter and Class E Rectifier

6.5 Conclusions

In this chapter, design guidelines to optimize assymetrical WPT systems have been derived and characterized in terms of operating frequency and antennae design. Moreover a circuit-system co-characterization approach has been proposed to design a resonant inductive coupling wireless power transfer link together with a class E

Efficiency	$d = 0.5$m	$d = 1.0$m	d= 1.833m
	53.60%	58.40%	7.41%

Table 6.3: DC-DC Efficiency

inverter and a class E rectifier to obtain a high-efficiency class E^2 WPT link. A DC-DC wireless power transfer system that maximizes a figure of merit combining both mass and efficiency performance metrics has been designed, demonstrating the necessity to co-design the wireless link and the power electronics front-end.

Chapter 7

Scalability Analysis

Contents

7.1 Introduction

RIC-WPT applications are currently mainly limited to point-to-point-links and do not target Single Input - Multiple Output (SIMO) scenarios. New challenges and applications of Resonant Non-Radiative Wireless Power Transfer emphasize the necessity to explore, predict and assess the behavior of RIC-WPT in SIMO links. Moreover, new system-level metrics have to be derived to study the scalability of multi-point Wireless Power Transfer applications and to provide design guidelines for these systems. In this chapter a Multiple Input - Multiple Output RIC-WPT System is modeled analytically from a circuit-centric point of view and validated using a Finite Element Field Solver. The analytical model and associated closed formulation is finally used to derive system-level metrics to predict the behavior and scalability of RIC MIMO Systems, showcasing the results for an asymmetric MIMO scenario.

Notwithstanding the notable progress of this research field, it is still unclear how a system-wide deployment of a WPT system capable of remotely supplying multiple receiver ends will perform for an increasing number of receivers. To address this legitimate and crucial question, this chapter provides a design-oriented model-based scalability analysis of a SIMO WPT system performance. In that pursuit, system-wide performance metrics are defined and their evolution when the dimensional

complexity of the system scales up in terms of number of receiver units is studied. As study context, note that, in the systems domain, scalability is defined as the ability of the system to maintain its performance and function, and retain all its desired properties when its scale is increased greatly without having a corresponding increase in the systems complexity. This topic has been analyzed in other fields where system interaction is essential, such as communication networks [88], distributed computing systems [89], smart grids [90], sensor networks [91] or software architecture [92]. The uniqueness of the SIMO Wireless Power Transfer application domain compared to the aforementioned fields lies in the tight electromagnetic and circuital intricate co-dependence present in a multiple receiver scenario. Accordingly, pursuing the deployment of RIC-WPT technology in multiple receiver applications with potentially a large number of units, it is necessary to revisit the current models of RIC-WPT systems from the SIMO perspective and to find new performance metrics and analytical procedures to optimize the behavior of such systems. A circuit-centric analytical scalable matrix model of a MIMO Resonant Inductive Coupling Wireless Power transfer System is provided in this chapter and validated using a Finite Element Field Solver, followed by a definition of system-level performance metrics including both overall and per node power efficiency and transferred power that are used together with the complete model to derive the behavior and scalability of a SIMO RIC-WPT system for two representative deployment scenarios of increasing and constant receiver densities.

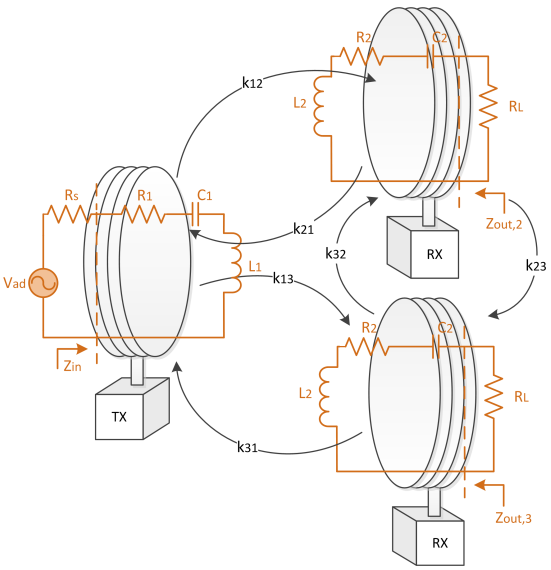

Figure 7.1: SIMO System Diagram

7.2 MIMO RIC System Circuit-Centric Matrix Model

As explained in previous chapters, Resonant inductive coupling between two electromagnetic resonators can be described by Lumped circuit theory using a coupled RLC representation system [40][38]. In this section, the circuit-centric analytical model is extended to a Single Input - Multiple Output Scenario, shown in figure 7.1 (illustrated for two receiving coils but scalable). In such a system, the capacitances and inductances model the resonant nature of the loops (C_i, L_i), the resistors model both the radiative and ohmic losses of the coils (R_i) and the coupling coefficients (k_{ij}) the magnetic coupling between them.

A MIMO Resonant Inductive Coupling Wireless Power Transfer System can be described and compressed in a system of equations, modeling the relationship between the currents at each node. To do this, two transfer functions have to be defined, namely: the relationship between current and voltage at a single node (local admittance, I_i/V_i) and the relationship between the induced voltage at a node i and the current in the node j that generated it (transimpedance, V_j/I_i) [39]. The local admittance (G_i) and transimpedance (G_{ij}) are shown in equation 7.1 for a RIC-WPT system.

$$G_i = \frac{I_i}{V_i} = \frac{1}{Z_i}; \quad G_{ij} = \frac{V_j}{I_i} = j\omega M_{ij} = j\omega k_{ij}\sqrt{L_i L_j} \tag{7.1}$$

where I_i, V_i are the current and voltage across the element (frequency dependance is ommited for compactness), Z_i is the impedance of the node, M_{ij} is the mutual inductance between two nodes and k_{ij} the coupling coefficient between them.

Using the defined local admittance and transimpedance, the system of equations that govern the relationship between currents at each node can be defined for a Multiple Input - Multiple Output (MIMO) system made of N elements as:

$$\begin{pmatrix} I_1 \\ I_2 \\ .. \\ I_N \end{pmatrix} = \begin{pmatrix} 0 & G_{21}G_1 & .. & G_{N1}G_1 \\ G_{12}G_2 & 0 & .. & G_{N2}G_2 \\ .. & .. & .. & .. \\ G_{1N}G_N & G_{2N}G_N & .. & 0 \end{pmatrix} \begin{pmatrix} I_1 \\ I_2 \\ .. \\ I_N \end{pmatrix} + \begin{pmatrix} V_{in,1}G_1 \\ V_{in,2}G_2 \\ .. \\ V_{in,N}G_N \end{pmatrix} \tag{7.2}$$

where G_1, G_2,.. G_N are the node gains (local admittances, $G_i = I_i/V_i$); G_{ij} is the transfer function related to the coupling between them (transimpedance, $G_{ij} = V_j/I_i$) and $V_{in,i}$ the input voltage applied in each transmitter.

Using the system of equations defined in 7.2, the power lost by the transmitters $(P_{i,T})$, the receivers $(P_{i,R})$ and the power transferred to the loads $(P_{i,L})$ in a MIMO scenario can be defined by:

$$P_{i,T} = \frac{|I_i|^2 \mathbb{R}(Z_i)}{2}; \quad P_{i,R} = \frac{|I_i|^2 \mathbb{R}(Z_i)}{2}; \quad P_{i,L} = \frac{|I_i|^2 R_L}{2} \tag{7.3}$$

and the total input power:

$$\sum_{i=0}^{i=N_T} P_{in,i} = \sum_{i=0}^{i=N_T} \left| \frac{V_{in,i}^2}{Z_{in,i}} \right| = \sum_{i=0}^{i=N_T+N_R} P_{i,R/T} + \sum_{i=0}^{i=N_R} P_{i,L} \tag{7.4}$$

where $Z_{in,i}$ is the input impedance seen by each transmitter, and N_T, N_R are the number of transmitters and receivers respectively.

A particularization of this model, in which only one node acts as a transmitter ($\forall V_{in,i\neq 1} = 0$), results in a Single Input-Multiple Output System configuration, defined in 7.5.

$$\begin{pmatrix} I_1 \\ I_2 \\ .. \\ I_n \end{pmatrix} = \begin{pmatrix} 0 & G_{21}G_1 & .. & G_{n1}G_1 \\ G_{12}G_2 & 0 & .. & G_{n2}G_2 \\ .. & .. & .. & .. \\ G_{1n}G_n & G_{2n}G_n & .. & 0 \end{pmatrix} \begin{pmatrix} I_1 \\ I_2 \\ .. \\ I_n \end{pmatrix} + \begin{pmatrix} V_{in,1}G_1 \\ 0 \\ 0 \\ 0 \end{pmatrix} \tag{7.5}$$

In such a system, the power lost by the transmitter $P_{1,T}$ ($P_{\forall i\neq 1,T} = 0$), the receivers ($P_{i,R}$) and the power transferred to the loads ($P_{i,L}$) is:

$$P_{1,T} = \frac{|I_1|^2 \mathbb{R}(Z_1)}{2}; \quad P_{i,R} = \frac{|I_i|^2 \mathbb{R}(Z_i)}{2}; \quad P_{i,L} = \frac{|I_i|^2 R_L}{2} \tag{7.6}$$

and the total input power:

$$P_{in} = \left| \frac{V_{in,1}^2}{Z_{in,1}} \right| = P_{1,T} + \sum_{i=0}^{i=N_R} (P_{i,R} + P_{i,L}) \tag{7.7}$$

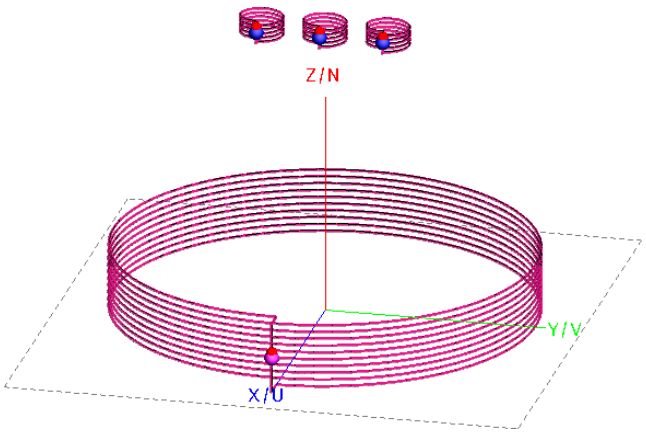

Figure 7.2: 4-Node SIMO System - FEKO

An Assymetrical RIC System made of 4 nodes (1 transmitter and 3 receivers) tuned to the same resonant frequency but with different inductances and losses (ohmic and radiative) has been used for illustration purposes (figure 7.2). Both

transmitter and receiver coils have been connected to an external capacitance C_s to force the resonance at $f = 6.65$MHz [1] and have been approximated by the equivalent circuits and values shown in figure 7.3.

The system of equations described in (7.5) can be solved yielding the currents at each node. In figure 7.4 the behavior of a SIMO RIC System (obtained through a Finite Element Field simulation) is compared to the analytical model provided in this thesis.

$R_{ac,TX}$	13.48MΩ
$R_{dc,TX}$	0.7109Ω
L_{TX}	0.507μH
$C_{p,TX}$	6.652pF
$C_{s,TX}$	5pF

$R_{ac,RX}$	67.46kΩ
$R_{dc,RX}$	0.04Ω
R_L	0.25Ω
L_{RX}	714.38pH
$C_{p,RX}$	9.45E-23F
$C_{s,RX}$	807.2pF

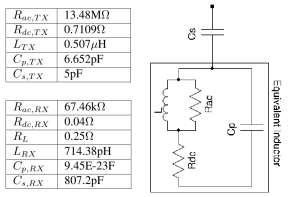

Figure 7.3: Transmitter and Receiver Equivalent Model

The transmitter current (I_1) and the receiver currents (I_2, I_3 and I_4) are illustrated in figure 7.4, showing a good agreement between the analytical model and the Finite Element Field Simulations and demonstrating the validity of the model.

The differences between both are explained by several approximations used in the analytical model, namely: a) the ohmic and radiative losses have been considered constant with frequency, b) the idealization of the equivalent inductances of the coils and c) the coupling between them ($k_{12} = k_{14} = 0.0056$, $k_{13} = 0.0061$, $k_{23} = k_{34} = 0.0218$, $k_{24} = 0.0015$).

7.3 System-Level Power-Related Metrics

In a Single Input - Single Output point-to-point RIC-WPT link, two metrics are used to assess the behavior of the link, namely: the maximum power transferred to the receiver PTL_{pp} and the power transfer efficiency PTE_{pp} (quocient between the power transferred to the receiver load and the input power). In such a link, the receiver load plays an important role upon the transfer function of the system, thereby affecting both the PTE and PTL. Moreover, the distance and orientation

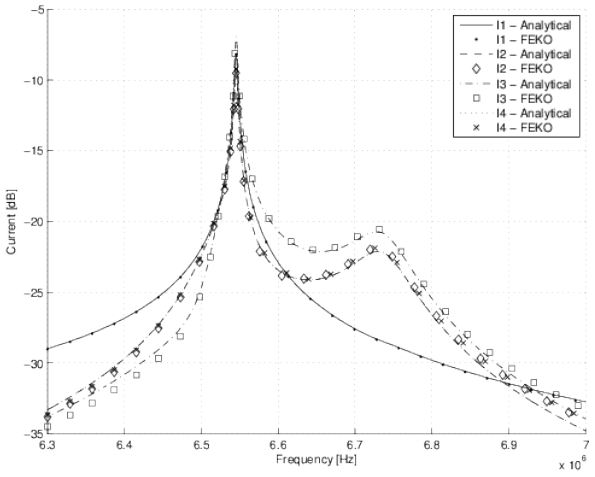

Figure 7.4: Analytical Model - Finite Element Comparison of circulating currents in a SIMO 3-Receiver System

of the coils greatly affect the reflected load impedance on the transmitter side, thus making both the transmitter and receiver impedances crucial when designing a RIC-WPT link [74, 41].

In a multi-node RIC-WPT link, due to the cross-coupling between the different nodes, the effects of the load upon the transfer function and efficiency of the system are increased. Moreover, the conflicting requirements between different operation modes of a RIC-WPT Multi-Node Link and the higher sensibility have stressed the necessity to derive system-wide metrics to evaluate, design and optimize the behavior of such a link.

In this chapter, two metrics are proposed to evaluate 1) the average power transfer efficiency and 2) the net power transferred to the loads in multi-node scenarios. These metrics, in addition to the point-to-point metrics PTE_{pp} and PTL_{pp} will provide a comprehensive system behavior evaluation and will be used to derive design guidelines. Therefore, four different performance metrics are proposed in this work: the power transfer efficiency of a point-to-point link between two nodes of the MIMO system (PTE_{pp}), the power transferred to the load in a point-to-point link (PTL_{pp}), the average net efficiency of the system (PTE_{sys}) and the average power transferred to the loads (PTL_{sys}).

7.3.1 Power Transfer Efficiency (PTE_{pp} and PTE_{sys})

The power transfer efficiency of a point-to-point link in an N-Node MIMO System with N_R receivers and N_T transmitters is:

$$\eta_{pp,j} = \frac{|I_j|^2 R_{L,j}}{\sum_{i=0}^{i=N_T} |I_{i,T}|^2 \mathbb{R}(Z_i) + \sum_{i=0}^{i=N_R} |I_{i,R}|^2 \mathbb{R}(Z_i)} \tag{7.8}$$

where j denotes the receiver node of the point-to-point link.

For illustration purposes, the point-to-point transfer efficiency $\eta_{N,PP}$ of the previous example (figure 7.2) is shown in figure 7.5, in which the analytical point-to-point efficiencies are compared to the Finite Element Field Solver results. Three different efficiencies are illustrated in this figure: $\eta_{pp,2}$, $\eta_{pp,3}$ and $\eta_{pp,4}$, related to the point-to-point efficiencies between the transmitter and the receivers 2, 3 and 4 respectively. Since the receivers 2 and 4 are placed symmetrically (they have the same couplings to the transmitter and to the rest of receivers), the currents flowing through them are almost the same $I_{L,2} = I_{L,4}$, which causes $\eta_{pp,2} = \eta_{pp,4}$. Finally, due to the fact that receiver 3 is more axially oriented to the transmitting coil, the coupling is higher ($k_{13} > k_{12} = k_{14}$) and hence the power received by this node (and thus the point-to-point efficiency) is higher.

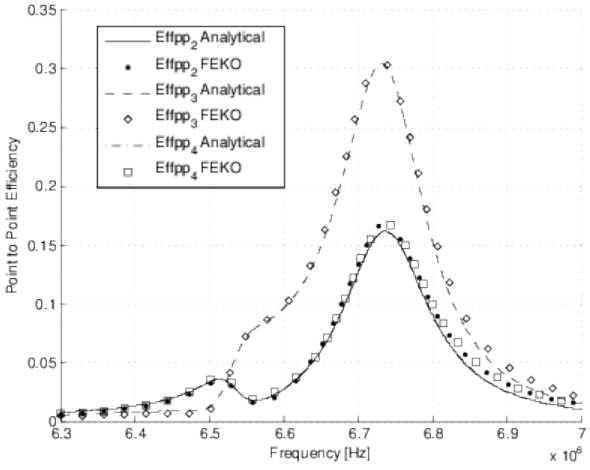

Figure 7.5: Point to Point Efficiency

It is important to note that, even though all the nodes have the same resonant frequency (6.65MHz), the maximum point-to-point efficiency is not obtained at this frequency, which can be explained by the fact that, since all the receivers are coupled between them, the system presents an overcoupled regime response [40].

If the overall system efficiency is to be analyzed, the efficiency has to be defined as the aggregation of power received by the loads divided by the input power of the

system. For a MIMO scenario with N_R receivers, N_T transmitters and $N = N_R + N_T$ number of nodes, this can be expressed as:

$$\eta_{N,avg} = \frac{\sum_{j=0}^{j=N_R} |I_j|^2 R_{L,j}}{\sum_{i=0}^{i=N} |I_i|^2 \mathbb{R}(Z_i)} \tag{7.9}$$

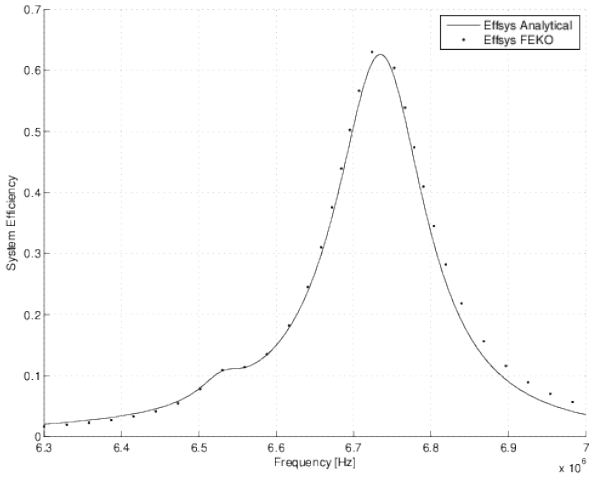

Figure 7.6: System Efficiency of a SIMO System

Figure 7.6 shows the system efficiency (analytical and FEKO) of the 4-Node SIMO System described above. It is possible to observe that, although the efficiency is decreased near the resonant frequency of the system due to the over-coupling, the overall efficiency is still very high.

7.3.2 Power Transferred to the Loads (PTL_{pp} and PTL_{sys})

In a Multi-Node Wireless Power Transfer Link, two different power metrics coexist: a) the power transferred between the transmitter and one of the receivers PTL_{pp} (point-to-point link inside a multi-node deployment) and b) the total output power of the system, defined as the sum of powers drained by each of the receiving nodes PTL_{sys}. The power transferred between a transmitting node and a receiving node (PTL_{pp}) placed inside a MIMO deployment can be obtained by:

$$P_{L,pp} = \frac{|I_{i,R}|^2 R_{L,i}}{2} \tag{7.10}$$

where $I_{i,R}$ is the current that flows through the receiver i and $R_{L,i}$ is the receiver load value.

Similarly, the System Output power, defined as the aggregation of power transferred to the loads of a N-Node System with N_R receivers is:

$$P_{L,sys} = \sum_{i=0}^{i=N_R} \frac{|I_{i,R}|^2 R_{L,i}}{2} \tag{7.11}$$

The PTL_{pp} in each of the receiving nodes of the 4-Node SIMO system described above is shown in figure 7.7 for illustration purposes, where a behavior similar to the point-to-point efficiency described in figure 7.5 can be observed: the point-to-point powers of nodes 2 and 4 are the same and the power level of the third receiver is higher due to a better coupling to the transmitter coil.

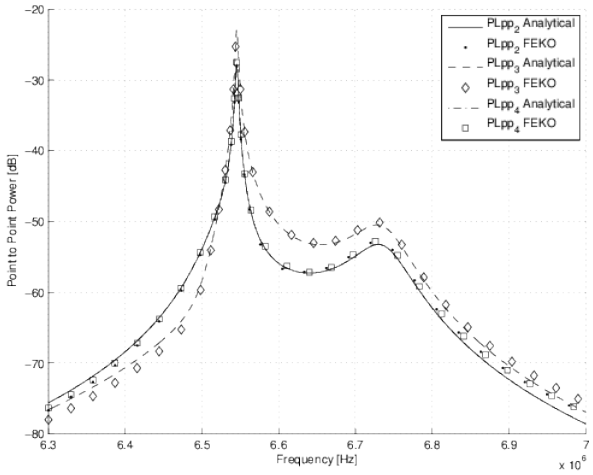

Figure 7.7: Point to Point Power of a SIMO System

The total output power (P_{sys}) has been obtained analytically for the 4-Node SIMO System and compared to the Finite Element Field Solver (FEKO) in figure 7.8, showing a good agreement between both.

7.4 Exploring Scalability in SIMO WPT links

Having validated the analytical model and provided the basis to assess the behavior of a multi-node wireless power transfer system with respect to a set of metrics, it is of interest to study the scalability of such systems. The scalability and behavior of a SIMO link strongly depends upon how the coupling between the transmitter and the receivers (G_{tr}) and the coupling between receivers (G_{rr}) scale when the number of nodes is increased, which is determined by the spatial geometry and distribution of the nodes. Therefore, the scalability model is derived for a general case ($G_{rr} = f(N)$ and $G_{tr} = f(N)$) and the results are studied and illustrated for two key scenarios which entail different couplings between the system nodes, namely:

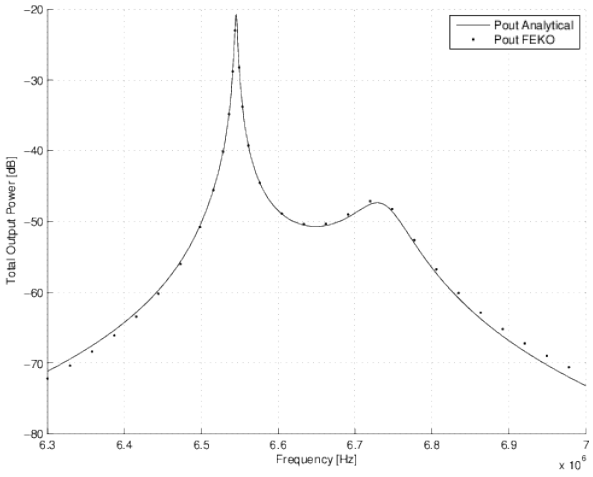

Figure 7.8: Output Power of a SIMO System

1. Increased Density: when the number of receivers N_R is increased within a constrained area. The coupling between the transmitter and the receivers is maintained $G_{tr} = ct$ but the coupling between the receivers is increased due to their reduced separation $G_{rr} = f(N)$.

2. Constant Density: when the number of receivers N_R is increased together with the deployment area. The coupling between transmitter and receivers is decreased $G_{tr} = f(N)$ but the coupling between receivers is maintained $G_{rr} = ct$ because the density remains constant.

These two scenarios will be explored in this section together with the approximations used to obtain a closed analytical formulation of the system metrics.

The deployment scenario targeted in this section consists on one transmitter coupled to a variable number of receivers, all of them with the same equivalent impedance ($G_T \neq G_R$ and $G_{R,\forall i} = G_R$). Figure 7.4 shows a SIMO 9-Node Deployment, used in the scalability analysis.

7.4.1 Scalability Model

To provide a closed-form analytical formulation of the system metrics, the following assumptions (applicable to the two SIMO scenarios explored in this section) have been considered: 1) the coupling between the transmitter and any of the receiver nodes has been considered equal $G_{t,\forall i} = G_{tr}$ and 2) the coupling between a receiver and any of its adjacent nodes has been considered the same ($G_{r,\forall i} = G_{rr}$), resulting

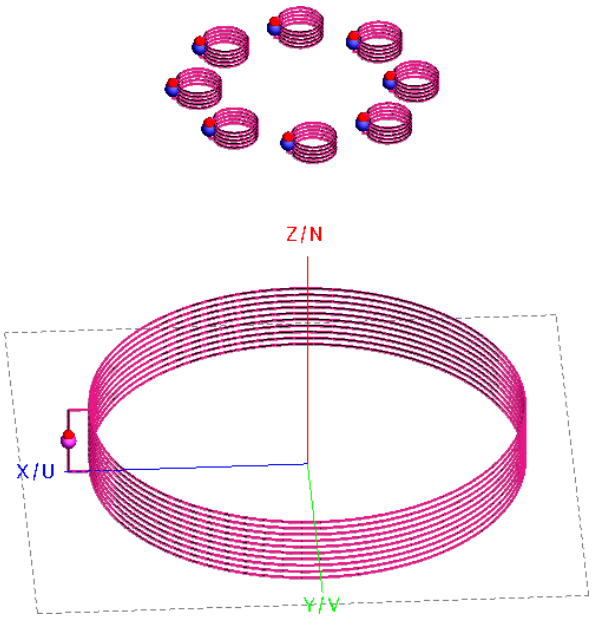

Figure 7.9: Assymetrical 9-Node SIMO System (1 Transmitter - 8 Receivers)

in the system of equations shown in (7.12).

$$\begin{pmatrix} I_T \\ I_{R,1} \\ .. \\ I_{R,N} \end{pmatrix} = \begin{pmatrix} 0 & G_{tr}G_t & .. & G_{tr}G_t \\ G_{tr}G_r & 0 & .. & G_{rr}G_r \\ .. & .. & .. & .. \\ G_{tr}G_r & G_{rr}G_r & .. & 0 \end{pmatrix} \begin{pmatrix} I_T \\ I_{R,1} \\ .. \\ I_{R,N} \end{pmatrix} + \begin{pmatrix} VG_t \\ 0 \\ 0 \\ 0 \end{pmatrix} \tag{7.12}$$

Moreover, if the coupling between non-adjacent receiving nodes is considered negligible with respect to the coupling between adjacent nodes ($G_{r,i+1} >> G_{r,i+2}$), the currents at the transmitter and the currents at each of the receivers of a N-Node SIMO System can be expressed analitically in closed-form formulation as:

$$\begin{aligned} I_T &= V_{in}\frac{G_t[2G_rG_{rr}-1]}{(N-1)G_rG_tG_{tr}^2+2G_rG_{rr}-1} \\ I_R &= V_{in}\frac{G_rG_tG_{tr}}{(N-1)G_rG_tG_{tr}^2+2G_rG_{rr}-1} \end{aligned} \tag{7.13}$$

where N is the number of nodes ($N-1$ receiver nodes), V_{in} is the input voltage of the transmitter, G_r is the transmitter gain, G_t is the receiver gain, G_{rr} is the mutual coupling between two adjacent receivers, and $G_{tr} = G_{rt}$ is the coupling between a receiver and a transmitter node.

These assumptions are validated in figure 7.10, where the current at the transmitter (I_T) and at each of the receiver nodes I_R of a 5-Node SIMO System with the approximations described above are compared to the currents obtained using the Finite Element Field Solver FEKO (I_T,$I_{R,1}$,$I_{R,2}$,$I_{R,3}$,$I_{R,4}$), showing a

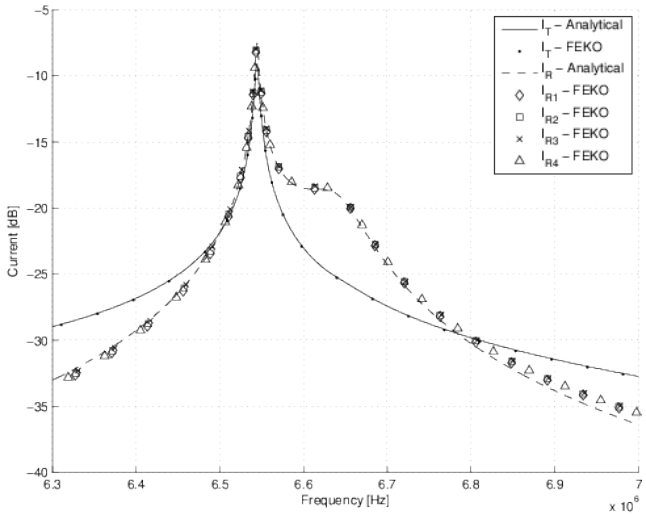

Figure 7.10: Currents I_T and I_R in a 5-Node SIMO System

good agreement between them. In this system, both transmitter and receiver coils are defined by the values shown in figure 7.3 with a transmitter-receiver coupling of $k_{tr} = 5.15 \times 10^{-3}$ and an adjacent coupling between receivers of $k_{rr} = 1.82 \times 10^{-3}$.

It is important to note that, as a result of the modelling assumptions, the current at each of the receiving coils is considered the same and equal to I_R while, when no approximations are used (FEKO) the currents differ. However, figure 7.10 demonstrates that the analytical results tightly agree with the Finite Element Field Solver results (in which none of the approximations were used), thus demonstrating the validity of the model and in turn allowing the formulation of the scalability analysis.

Using the transmitter and receiver currents in 7.13, the point-to-point efficiency (equal for all the receivers since the currents are considered the same and equal to I_R) and the system efficiency can be expressed as:

$$\begin{aligned} \eta_{pp} &= \frac{G_r^2 G_t G_{tr}^2 R_L}{4G_r^2 G_{rr}^2 - G_r(4G_{rr} - N_R G_t G_{tr}^2) + 1} \\ \eta_{sys} &= \frac{N_R G_r^2 G_t G_{tr}^2 R_L}{4G_r^2 G_{rr}^2 - G_r(4G_{rr} - N_R G_t G_{tr}^2) + 1} \end{aligned} \tag{7.14}$$

where $N_R = N - 1$ is the number of receiver nodes and R_L is the receiver load.

The point-to-point efficiency η_{pp}, which is equal for all the nodes, and the total system efficiency η_{sys} are shown in figures 7.11 and 7.12 respectively showing a good agreement with the Finite Element numerical results. In figure 7.11 a slight difference between the analytical model and the FEKO data can be observed, which is explained by the fact that all the receivers have been considered equal but

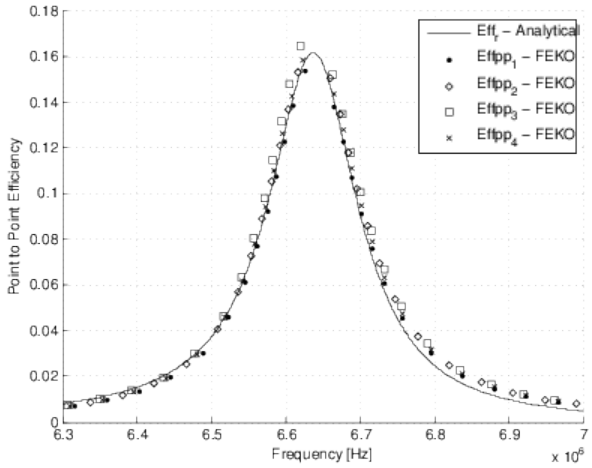

Figure 7.11: Point to Point Efficiency

the system is not absolutely symmetrical (the load is placed in a different position with respect to the transmitter, which slightly varies the coupling between them).

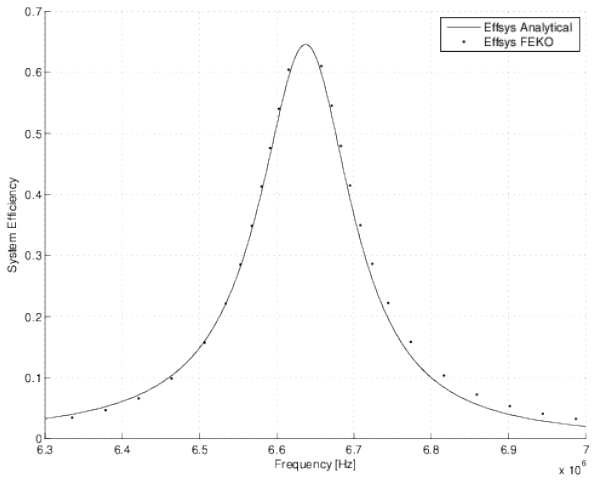

Figure 7.12: System Efficiency

The power transferred to the loads (total output power of the system) can be expressed as the sum of the power transferred to the load at each receiver:

$$\begin{aligned} P_{L,pp} &= \frac{G_r^2 G_t^2 G_{tr}^2 R_L V_{in}^2}{2(N_R G_r G_t G_{tr}^2 + 2G_r G_{rr} - 1)^2} \\ P_{L,sys} &= \sum_{N_R} P_{L,i} = \frac{N_R G_r^2 G_t^2 G_{tr}^2 R_L V_{in}^2}{2(N_R G_r G_t G_{tr}^2 + 2G_r G_{rr} - 1)^2} \end{aligned} \tag{7.15}$$

Figure 7.13 illustrates the results for the point-to-point power at each of the receivers

$PTL_{pp,i}$ and the total output power PTL_{sys}.

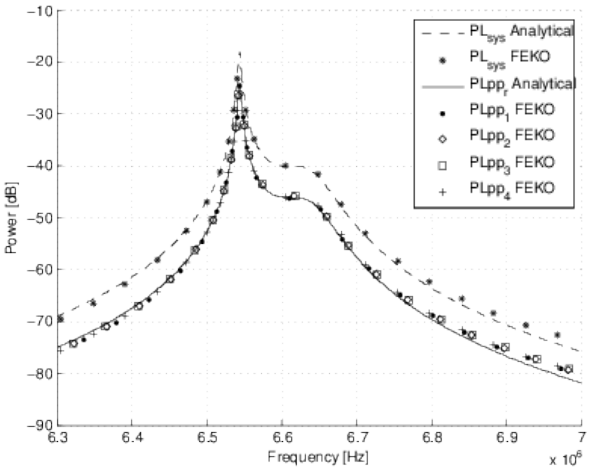

Figure 7.13: Power Transfer to the Loads

It is important to note that, for a given distribution, the coupling between receivers G_{rr} and between the transmitter and the receivers G_{tr} can be expressed by a function of the number of receivers N_R. Provided that this function is known for a given deployment node distribution, the number of nodes that maximizes each of the system metrics (Point-to-Point Efficiency, System Efficiency, Point-to-Point Power Transferred to the load and total Output Power) can be found by differentiating the equations given in 7.14 and 7.15 with respect to N_R:

$$\begin{aligned} N_{o,\eta_{pp}} \rightarrow \frac{\partial \eta_{pp}}{\partial N_R} = 0; \qquad N_{o,\eta_{sys}} \rightarrow \frac{\partial \eta_{sys}}{\partial N_R} = 0 \\ N_{o,P_{L,pp}} \rightarrow \frac{\partial P_{L,pp}}{\partial N_R} = 0; \quad N_{o,P_{L,sys}} \rightarrow \frac{\partial P_{L,sys}}{\partial N_R} = 0 \end{aligned} \tag{7.16}$$

The optimal number of nodes will strongly depend upon the distribution of the deployment (how the receiving nodes are distributed within the area when N_R increases), which is represented by the variation of the inter-node coupling/gains $G_{rr}(N)$ and $G_{tr}(N)$. Therefore, when exploring the scalability of a RIC-WPT link with regards to the number of receivers, it is necessary to take into account how G_{tr} and G_{tr} are modified when N_R increases, which has to do with the deployment geometry and spatial distribution. Two particular cases of the spatial distribution: $G_{tr} = ct$; $G_{rr} = f(N)$ (increased density) and $G_{tr} = f(N)$; $G_{rr} = ct$ (constant density) are explored below.

7.4.2 Increased Density Scalability: $G_{tr} = ct$, $G_{rr} = f(N)$

Once the model has been verified, it is possible to analyze the performance scalability of a multi-node RIC-WPT SIMO System. In this section, the number of

receiver nodes is increased (from 5 to 17) within a constrained deployment area, thus increasing the density of nodes. In this scenario, the coupling between the transmitter and the receivers is maintained while the coupling between adjacent receivers increases proportionally to the number of nodes due to the increased density (k_{rr} increases with N).

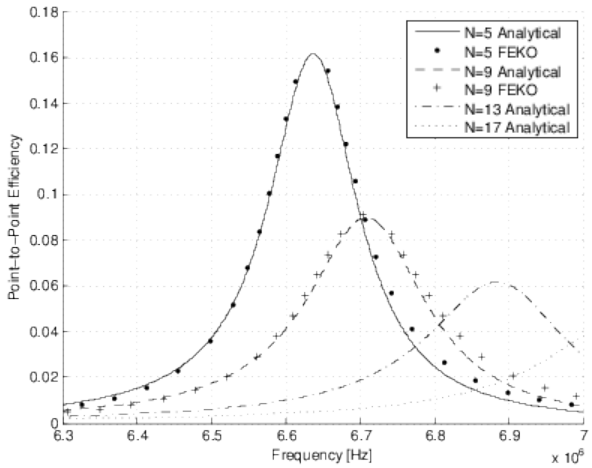

Figure 7.14: Scalability with increased density: Point - to Point Efficiency

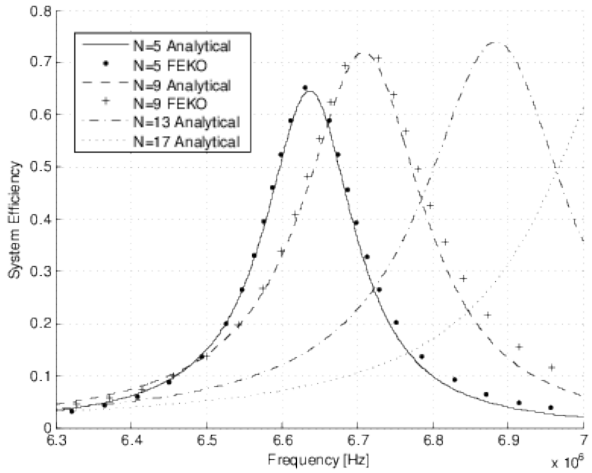

Figure 7.15: Scalability with increased density: System Efficiency

Figures 7.14 and 7.15 show the analytical point-to-point efficiency η_{pp} and total system efficiency η_{sys} for a different number of receiving nodes ($N_R = 4, 8, 12$ and 16), contrasted to the Finite Element results for $N_R = 4$ and $N_R = 8$. It is possible to see that, while the point-to-point efficiency decreases when the number of nodes increase (figure 7.14) the system efficiency increases (figure 7.15). This is explained

by two different behaviors: a) since all the receiving nodes are equally coupled to the transmitter, all of them drain power and, thus, the total power is divided amongst the receiving nodes resulting in a low point-to-point efficiency, which is equal to say that all the receivers act as interfering objects draining power from the point-to-point link in this configuration [52]. However, in the second scenario (b) all of them contribute to the system efficiency and an increase in the number of nodes is not detrimental to the link.

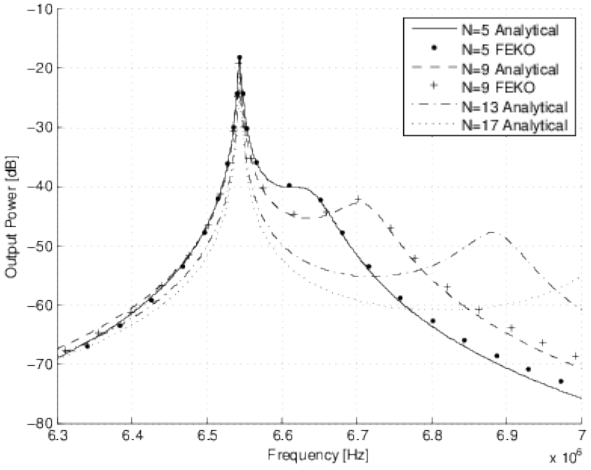

Figure 7.16: Scalability with increased density: Output Power

Not only the point-to-point maximum efficiency decreases when the number of nodes increases (as seen in figure 7.14) but also the maximum efficiency point (which can be seen in both figures 7.14 and 7.15) is shifted to higher frequencies. This is explained by a change in the resonant frequency of the system (the input impedance from the transmitter is modified due to the additional receivers). Finally, it is important to note that the maximum system efficiency is obtained when the number of receiving nodes is increased. This is due to a higher coupling between transmitter and receiver, caused by the interrelation between the number of nodes (N_R) and their equivalent impedances ($1/G_R$) in this case.

Figures 7.16 and 7.17 show how the point-to-point power transferred to the load and the total output power scale when the number of receivers is increased. It can be observed that neither the point-to-point not the output power is increased when the number of receivers is, which is explained by the fact that the system is operating in the overcoupling regime and, thus, when the number of receivers is increased, the overcoupling is increased too.

7.4.3 Constant Density Scalability: $G_{tr} = f(N)$, $G_{rr} = ct$

In this section, the scalability is studied for a deployment scenario in which the number of receivers N_R is increased while maintaining their spatial density, this is, the deployment area is increased as the number of nodes increases. In this case,

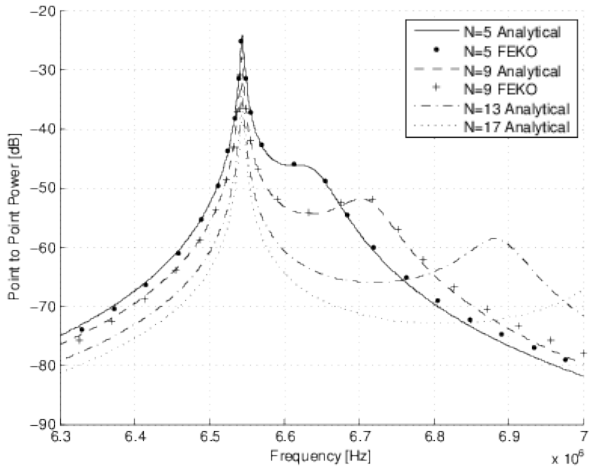

Figure 7.17: Scalability with increased density: Point - to - Point Power

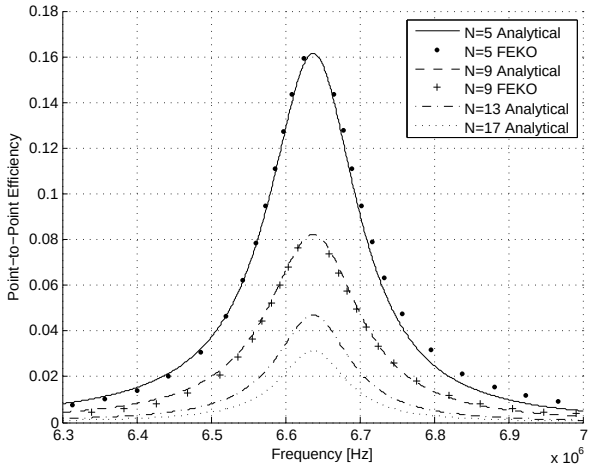

Figure 7.18: Scalability with Constant Density: Point - to Point Efficiency

the coupling between receivers is maintained constant ($G_{rr} = ct$) but the coupling between the transmitter and the receivers is decreased ($G_{tr} = f(N)$) due to the larger distance between the transmitter and the receivers.

Figures 7.18 and 7.19 showcase the point-to-point efficiency and the system efficiency for this particular but representative configuration. In this scenario, since k_{rr} remains constant, there is no change in the resonant frequency of the system (the maximum efficiency point is always at 6.65MHz) but a difference arises: while the point-to-point efficiency decreases with N_R (as in the previous sections), the total system efficiency reaches a maximum when the number of receivers $N = 9$ and then decreases with N_R. This means that the system efficiency is

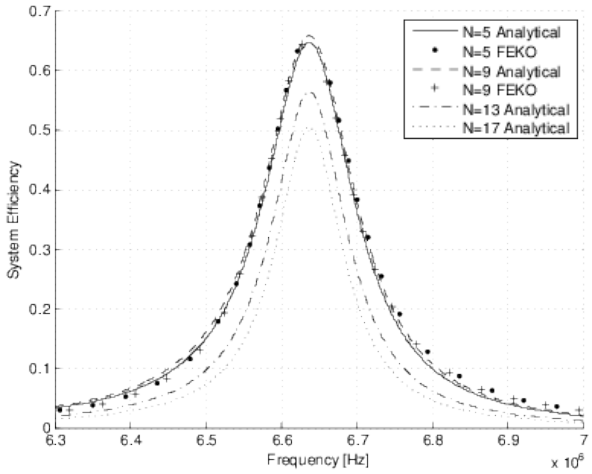

Figure 7.19: Scalability with Constant Density: System Efficiency

maximum for $N_{o,R} = 8$, as derived -for the general case scenario- from equation 7.16.

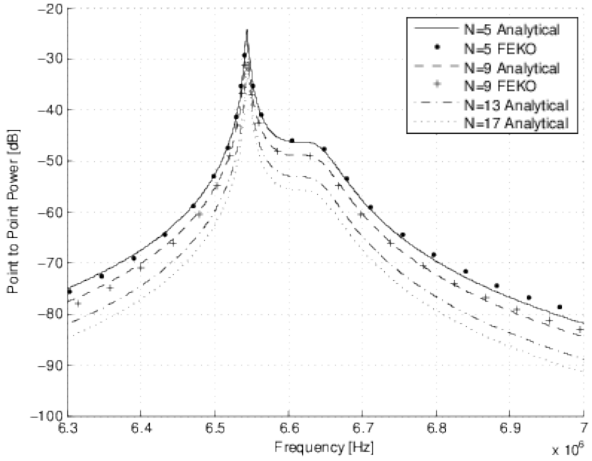

Figure 7.20: Scalability with Constant Density: Point - to - Point Power

Figures 7.20 and 7.21 illustrate the point-to-point power transferred to the load and the total output power respectively. It can be observed that, similarly to the efficiency results, the point-to-point power transferred to the load decreases with N_R but the total output power is very close in the $N_R = 4$ and $N_R = 8$ configurations, since the optimal number of receivers (for maximum output power) is between these two scenarios.

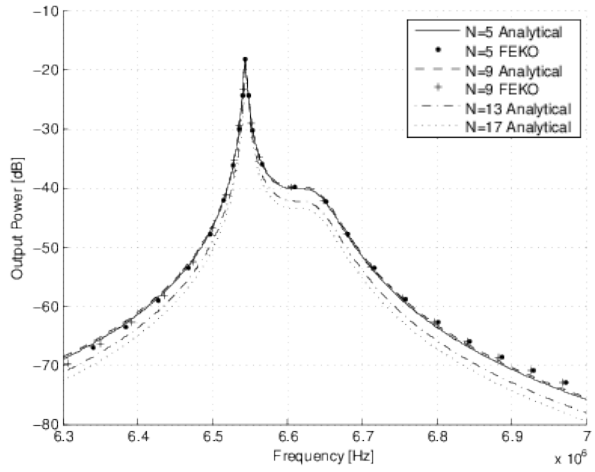

Figure 7.21: Scalability with Constant Density: Output Power

7.5 Conclusions

A circuit-centric matrix analytical model that predicts the behavior of Multiple Input-Multiple Output Resonant Inductive Coupling Wireless Power Transfer Systems has been presented. The analytical model has been benchmarked using a Finite Element Field Solver and used to derive system-level metrics to assess the performance of such systems. Finally, based on derived closed formulation, these metrics have been applied to analyze the scalability of SIMO RIC-WPT Systems oriented to dimension and provide design guidelines aiming the applicability and practical deployment of this technology in SIMO Scenarios.

Chapter 8

Conclusions

Contents

8.1 Conclusions

This thesis has explored the different challenges at various design levels that are currently precluding the adoption of Resonant Inductive Wireless Power Transfer. By circumventing those challenges, a myriad of applications of Wireless Power Transfer would be enabled in the areas of biomedical, electric vehicle battery charging, industrial robotics and space power.

Towards the practical deployment of RIC-WPT applications, this thesis has first provided a unified analytical model that merges the electromagnetic field theory with circuit theory, unifying the two research communities that first addressed this problem. This model, which provided an equivalence demonstration between the current theories in both research fields, has been analyzed in both single-node and multi-node wireless power transfer applications and benchmarked using a multi-domain cross-model validation, thus resulting in a common ground to understand and design wireless power transfer systems.

Once the analytical model had been demonstrated, the fundamental challenges that were limiting the applicability of RIC-WPT were analyzed, namely: Port Impedance Matching, Distance and Frequency Effects, and Interfering Objects and Relaying Effects, providing a system-level model for those together with a complete characterization of their effects. Finally, a set of design methodologies to counteract or minimize these effects has been provided.

- Port Impedance Matching: chapter 3 has modeled the impedance matching problem affecting both single-node and multi-node RIC-WPT scenarios and provided design guidelines to achieve maximum power transfer efficiency in

terms of source and load impedance and distance between coils.

- Distance and Frequency Effects: chapter 4 analyzed the effects of distance and frequency mismatch effects upon a RIC-WPT system. A complete design-space exploration was developed to characterize the effects of such variations and guidelines to adapt the impedance of transmitter and receiver antennas in order to minimize these effects were proposed. Finally, the behavior of a distance/frequency variation upon the the transient performance of RIC-WPT was studied.

- Interfering Objects and Relaying Effects: one of the main challenges towards multi-node RIC-WPT is the effect of multiplicity of nodes (either active or passive) to the overall system efficiency and performance. Due to this, chapter 5 provided an analytical model of interfering objects and benchmarked its results with the ones obtain through a Finite-Element Field Solver Tool (FEKO), using the same methodology as in the unified analytical model. Once the analytical model was obtained, a design-oriented characterization of its effects was studied for different use-case scenarios (interfering objects close to transmitter, receiver or both). Finally, a set of guidelines to overcome interfering objects using impedance matching techniques has been proposed and applied to benchmark the effects of the International Space Station upon a Wireless Power Transfer Satellital Link (used in RINGS-NASA Project). Finally, this work has unveiled the capacity of interfering objects to potentially improve the performance of multi-node WPT scenarios as relays. This chapter revisits the previous analytical model from the relaying perspecctive and provides design guidelines to force this behavior.

By solving the first group of fundamental challenges, this thesis has provided a better understanding of the key elements that affect the design of such RIC-WPT system. However, the optimization of such design and its scalability was still unclear.

Chapter 6 provides a frequency optimization methodology to maximize the wireless power transfer efficiency in RIC-WPT systems in both Symetric and Assymetric deployments. Moreover, the antennae optimizations of such links are studied and guidelines to minimize the losses of RIC-WPT antennae are proposed, which result key in the deployment of these networks. Finally, the front-end electronics that drive the RIC-WPT link are analyzed and a complete design-oriented joint circuit-system approach is proposed to optimize the performance of such links using class E^2 inverter and rectifiers.

Towards the application of RIC-WPT systems on multi-node deployments such as IoT, chapter 7 provides a circuit-centric matrix analytical model that predicts the behavior of Multiple Input-Multiple Output WPT Systems. The analytical model is then benchamarked using a Finite Element Field Solver and system-level

metrics to assess the performance of such systems was proposed. Finally, based on this derived closed formulation, these metrics have been provided to analyze the scalability of SIMO RIC-WPT systems oriented to dimension and provide design guidelines towards the practical applicability of such systems.

8.2 Future Work

This work has explored several challenges precluding the applicability of RIC-WPT and it has demonstrated that, due to the sensitivity of such systems, it is necessary to optimize several design variables at different domain levels. In this sense, future work encompasses the application of these analytical models to multi-domain optimization tools to be able to better overcome such challenges and provide a complete system-design approach.
Also, due to the applicability of RIC-WPT to the Internet of Things, Smart Buildings and large deployments of small sensor networks, future work should pay special attention to the requirements of such applications, namely: a) the transmission of data and power over RIC to minimize the energy consumption of communication between such nodes, b) a control system that enables WPT over a mobile network of sensors (distance that connect and disconnect and vary the distance between them), c) applying intelligent control methods and artificial intelligence to the matching and control of such wireless power transfer networks and finally d) generating a set of standars that could provide the means to mass production of RIC-WPT compatible devices.

8.3 Participation in Research Projects

This work has been part of several researh projects, namely:

- Horizon 2020-Earth Observation-3-2015. ONION: Operational Network of Individual Observation Nodes. 2016-2018.

- Spanish Ministry of Economy and Competitiveness, state plan for Scientific and Technical research and innovation 2013-2016, State program for Research, Development and Research oriented to Society challenges (ref. DPI2013-47799-C2-2-R) “Health aware enhanced range Wireless Power Transfer (WPT) systems”, Sep 2014 â Sept 2017.

- Google Faculty Research Awards “Phone-satellite: Android beyond the stratosphere”, Sept. 2013 â Sept. 2014.

- Resonant Inductive Near-field Generation System (RINGS). Defense Advanced Research Projects Agency (DARPA) National Aeronautics and Space Administration (NASA). University of Maryland - Massachusetts Institute of Technology. Jan 2012 - December 2014.

- Spanish Ministry of Science and Technology, CONSOLIDER-INGENIO program “Advanced Wide Band Gap Semiconductor Devices for Rational Use of Energy (RUE)”, Project period: Jan 2010 â Jan 2014.

8.4 Publications

- Maximizing efficiency through impedance matching from a circuit-centric model of non-radiative resonant wireless power transfer, [40]
- A Comparison of Analytical Models for Resonant Inductive Coupling Wireless Power Transfer [74]
- Demonstration of electromagnetic formation flight and wireless power transfer [36]
- Analytical design procedure for resonant inductively coupled wireless power transfer system with class-E 2 DC-DC converter [43]
- Optimization of WPT efficiency using a conjugate load in non-impedance matched systems. [41]
- Inductively coupled wireless power transfer with class-E 2 DC-DC converter [93]
- Translayer optimized co-design of in-space microwave based wireless power transfer [14]
- Interference analysis on resonant inductive coupled wireless power transfer links [94]
- Analysis and Design of Loosely Inductive Coupled Wireless Power Transfer System Based on Class-E^2 DC-DC Converter for Efficiency Enhancement [95]
- Scalability analysis of SIMO non-radiative resonant wireless power transfer systems based on circuit models [78]
- Analytical design for resonant inductive coupling wireless power transfer system with class-E inverter and class-DE rectifier [96]
- Advances in non-radiative resonant inductive coupling wireless power transfer: a comparison of alternative circuit and system models driven by emergent applications [37]
- Temperature gradient sensor from pulsed power supply duty cycle in ultra-low-power energy harvesting system [97]
- On Frequency Optimization of Assymetric Resonant Inductive Coupling Wireless Power Transfer Links [47]

- Class e2 resonant non-radiative wireless power transfer link: A design-oriented joint circuit-system co-characterization approach. [45]
- Dual-purpose Resonate Actuators for Electromagnetic Formation Flight and Wireless Power Transfer [81]
- Interference analysis on resonant inductive coupled wireless power transfer [94]
- Steady-State Analysis of Isolated Class-E2 Converter Outside Nominal Operation [98]
- Multipath relaying effects in multiple-node resonant inductive coupling wireless power transfer [75]
- On tunable switch-mode reactive networks: A gyrator-based resonator emulation [99]
- Relay effects in multiple-node Resonant Inductive Coupling Wireless Power Transfer systems [100]
- Unveiling nonlinear dynamics in resonant inductively coupled wireless power transfer [101]

8.5 Patents

- System and method for tuning wireless power transfer receivers. Mohamed Saad, Elisenda Bou-Balust, Eduard Alarcon. 2017/2 ES. App. Number: P201730148

List of Figures

List of Tables

Bibliography

[1] R. Sedwick, "Long range inductive power transfer with superconducting oscillators," *Annals of Physics*, vol. 325, 2010. (Cited on pages 1, 41, 112, 121, 130 and 140.)

[2] C. Balanis, *Antenna Theory Analysis and Design*. Wiley, 3 ed., 2005. (Cited on pages 3, 7, 9, 25, 27, 113, 114, 129 and 163.)

[3] C. Dailey, "Microwave power receiving antenna," October 1970. (Cited on page 8.)

[4] W. Brown, "Experimental airborne microwave supported platform," Tech. Rep. AD0474925, NASA, 1965. (Cited on page 9.)

[5] W. Brown, "The history of power transmission by radio waves," *Microwave Theory and Techniques, IEEE Transactions on*, vol. 32, pp. 1230 – 1242, sep 1984. (Cited on page 9.)

[6] J. Lan Sun Luk, A. Celeste, P. Romanacce, L. Chane Kuang Sang, and J. Gatina, "Point to point wireless power transportation in reunion island," *48th International Astronautical Congress*, 1997. (Cited on page 9.)

[7] N. Kaya, H. Matsumoto, S. Miyatake, I. Kimura, and M. Nagatomo, "Nonlinear interaction of strong microwave beam with the ionosphere minix experiment," *International Symposium of Antennas and Propagation*, vol. 6, no. 3, pp. 181–186, 1986. (Cited on page 9.)

[8] H. Matsumoto and N. Kaya, "Isy-mets rocket experiment and its preparatory airplane experiment," *43rd International Astronautical Congress*, 1992. (Cited on page 9.)

[9] M. G. E., "Status of international experimentation in wireless power transmission," *Elsevier - Solar Energy*, vol. 56, no. 1, pp. 87–91, 1996. (Cited on page 9.)

[10] P. Glaser, "An overview of the solar power satellite option," *Microwave Theory and Techniques, IEEE Transactions on*, vol. 40, pp. 1230 –1238, jun 1992. (Cited on page 9.)

[11] K. Nishida, Y. Taniguchi, K. Kawakami, Y. Homma, H. Mizutani, M. Miyazaki, H. Ikematsu, and N. Shinohara, "5.8 ghz high sensitivity rectenna array," in *Microwave Workshop Series on Innovative Wireless Power Transmission: Technologies, Systems, and Applications (IMWS), 2011 IEEE MTT-S International*, pp. 19 –22, may 2011. (Cited on page 9.)

[12] Z. Popovic, *Lunar Wireless Power Transfer Feasibility Study.* DOE/NV/25946–488, 2008. (Cited on page 9.)

[13] Y. Fuse, T. Saito, S. Mihara, K. Ijichi, K. Namura, Y. Honma, T. Sasaki, Y. Ozawa, E. Fujiwara, and T. Fujiwara, "Outline and progress of the japanese microwave energy transmission program for ssps," in *Microwave Workshop Series on Innovative Wireless Power Transmission: Technologies, Systems, and Applications (IMWS), 2011 IEEE MTT-S International*, pp. 47 –50, may 2011. (Cited on page 9.)

[14] E. Bou-Balust, E. Alarcon, A. Saenz-Otero, and C. Mandy, "Translayer optimized co-design of in-space microwave based wireless power transfer," *Proceedings of 2010 IEEE International Symposium on Circuits and Systems*, pp. 885–888, 30 May 2010. (Cited on pages 9 and 160.)

[15] A. Nagahama, T. Mitam, N. Shinohara, N. Tsuji, K. Fukuda, Y. Kanan, and K. Yonemoto, "Study on a microwave power transmitting system for mars observation airplane," in *Microwave Workshop Series on Innovative Wireless Power Transmission: Technologies, Systems, and Applications (IMWS), 2011 IEEE MTT-S International*, pp. 63 –66, may 2011. (Cited on page 9.)

[16] W. Brown and E. Eves, "Beamed microwave power transmission and its application to space," *Microwave Theory and Techniques, IEEE Transactions on*, vol. 40, pp. 1239 –1250, jun 1992. (Cited on page 9.)

[17] J. Shudder, H. Stephenson, and J. Townsend, "Energy transfer into a closed chest by means of stationary coupling coils and a portable high-power oscillator," *ASAIO*, vol. 7, pp. 327–331, april 1961. (Cited on page 9.)

[18] M. Ghovanloo and K. Najafi, "A wireless implantable multichannel microstimulatin system-on-a-chip with modular architecture," *IEEE Trans. Neural Syst. Rehab. Eng.*, vol. 15, pp. 449–457, September 2007. (Cited on page 9.)

[19] M. Schaldach, "Bioelectric energy sources for cardiac pacing," *Annals of the New York Academy of Sciences*, vol. 167, pp. 1016–1024, 1969. (Cited on page 9.)

[20] N. Mohan, T. Undeland, and W. Robbins, *Power Electronics: converters, applications and design.* Wiley, October 2002. (Cited on page 9.)

[21] A. Marincic, "Nikola tesla and the wireless transmission of energy," *IEEE Transacions on Power Apparatus and Systems*, vol. PAS101, October 1982. (Cited on page 9.)

[22] J. Rock and L. Schwappack, "Wireless power," March 2010. (Cited on page 9.)

[23] M. Schwan and P. Troyk, "High efficiency driver for transcutaneously coupled coils," *IEEE Engineering in Medicine and Biology Society. 11th Annual Intenrational Conference*, pp. 1403–1404, November 1989. (Cited on page 10.)

[24] P. Si, A. Hu, S. Malpas, and D. Budgett, "A frequency control method for regulating wireless power to implantable devices," *Biomedical Circuits and Systems, IEEE Transactions on*, vol. 2, pp. 22 –29, march 2008. (Cited on page 10.)

[25] K. Silay, C. Dehollain, and M. Declercq, "Improvement of power efficiency of inductive links for implantable devices," in *Research in Microelectronics and Electronics, 2008. PRIME 2008. Ph.D.*, pp. 229 –232, 22 2008-april 25 2008. (Cited on page 10.)

[26] A. Kurs, A. Karalis, R. Moffat, J. Joannopoulos, P. Fisher, and M. Soljacic, "Wireless power transfer via strongly coupled magnetic resonances," *Science*, vol. 6, pp. 83–86, June 2007. (Cited on pages 10, 11, 13, 18, 39, 46 and 72.)

[27] A. Kurs, J. Joannopoulos, and M. Soljacic, "Efficient wirless non-radiative mid-range energy transfer," *Annals of Physics*, vol. 323, pp. 34–48, 2008. (Cited on pages 10, 13, 18 and 39.)

[28] I. Corporation, "Intel cto says gap between humans and machines will close by 2050," 2009. (Cited on page 10.)

[29] A. J., M. Gasulla, T. Jager, and L. Reindl, "Wireless power transmission for autonomous sensors in removable vehicle seats," *IEEE Vehicular Technology Conference (VTC Fall)*, 2011. (Cited on page 10.)

[30] J. Villa, J. Sallan, Llombart, and J. Sanz, "Optimal design of icpt systems applied to electric vehicle battery charge," *IEEE Transactions on Industrial Electronics*, vol. 56, no. 6, 2009. (Cited on page 10.)

[31] U. Madawala and D. Thrimawithana, "A bidirectional inductive power interface for electric vehicles in v2g systems," *Industrial Electronics, IEEE Transactions on*, vol. 58, pp. 4789 –4796, oct. 2011. (Cited on page 10.)

[32] A. RamRakhyani, S. Mirabbasi, and M. Chiao, "Design and optimization of resonance-based efficient wireless power delivery systems for biomedical implants," *Biomedical Circuits and Systems, IEEE Transactions on*, vol. 5, pp. 48–63, Feb 2011. (Cited on pages 10, 11 and 122.)

[33] M. Cabrera, R. Trifonov, A. Castells, and K. Stoy, "Wireless communication and power transfer in modular robots," *IEEE RSJ International Conference on Intelligent Robots and Systems*, 2011. (Cited on page 10.)

[34] L. Z.S., L. D.J., and C. Y., "Design considerations for electromagnetic couplers in contactless power transmission systems for deep sea applications," *Journal of Zhejiang University Science*, vol. 11, 2010. (Cited on page 10.)

[35] M.-M. O., G. Fanti, Y. Feng, K. Omanakuttan, R. Ongie, A. Setjoadi, and N. Sharpe, "Wireless power transfer using weakly coupled magnetostatic resonators," *IEEE Energy Conversion Congress and Exposition*, 2010. (Cited on page 10.)

[36] A. K. Porter, D. J. Alinger, R. J. Sedwick, J. Merk, R. A. Opperman, A. Buck, G. Eslinger, P. Fisher, D. W. Miller, and E. Bou-Balust, "Demonstration of electromagnetic formation flight and wireless power transfer," *Journal of Spacecraft and Rockets*, vol. 51, no. 6, pp. 1914–1923, 2014. (Cited on pages 11 and 160.)

[37] E. Bou-Balust, R. Sedwick, P. Hu, and E. Alarcon, "Advances in non-radiative resonant inductive coupling wireless power transfer: a comparison of alternative circuit and system models driven by emergent applications," in *Circuits and Systems (ISCAS), 2014 IEEE International Symposium on*, pp. 2037–2040, IEEE, 2014. (Cited on pages 11, 34, 102 and 160.)

[38] M. Kiani and M. Ghovanloo, "The circuit theory behind coupled-mode magnetic resonance-based wireless power transmission," *Circuits and Systems I: Regular Papers, IEEE Transactions on*, vol. PP, no. 99, p. 1, 2012. (Cited on pages 11, 13, 18, 19, 20, 46, 112, 139 and 163.)

[39] R. J. Sedwick, "A fully analytic treatment of resonant inductive coupling in the far field," *Annals of Physics*, vol. 327, no. 2, pp. 407–420, 2012. (Cited on pages 11, 27, 112, 121, 130 and 139.)

[40] E. Bou, R. Sedwick, and E. Alarcon, "Maximizing efficiency through impedance matching from a circuit-centric model of non-radiative resonant wireless power transfer," in *Circuits and Systems (ISCAS), 2013 IEEE International Symposium on*, pp. 29–32, IEEE, 2013. (Cited on pages 11, 25, 26, 71, 107, 113, 129, 139, 144 and 160.)

[41] M. Chabalko, E. Alarcon, E. Bou-Balust, and D. S. Ricketts, "Optimization of wpt efficiency using a conjugate load in non-impedance matched systems.," in *Antennas and Propagation Society International Symposium (APSURSI), 2014 IEEE*, pp. 645–646, IEEE, 2014. (Cited on pages 11, 107, 141 and 160.)

[42] M. Pinuela, D. Yates, S. Lucyszyn, and P. Mitcheson, "Maximizing dc-to-load efficiency for inductive power transfer," *Power Electronics, IEEE Transactions on*, vol. 28, pp. 2437–2447, May 2013. (Cited on page 11.)

[43] T. Nagashima, K. Inoue, X. Wei, E. Bou-Balust, E. Alarcon, M. Kazimierczuk, and H. Sekiya, "Analytical design procedure for resonant inductively coupled wireless power transfer system with class-e2 dc-dc converter," in *Circuits and Systems (ISCAS), 2014 IEEE International Symposium on*, pp. 113–116, June 2014. (Cited on pages 11 and 160.)

[44] K.-G. Moti, F. Neri, S. Moon, P. Yeon, J. Yu, Y. Cheon, Y.-S. Roh, M. Ko, and B.-H. Park, "12.9 a fully integrated 6w wireless power receiver operating at 6.78mhz with magnetic resonance coupling," in *Solid- State Circuits Conference - (ISSCC), 2015 IEEE International*, pp. 1–3, Feb 2015. (Cited on page 11.)

[45] E. Bou-Balust, T. Nagashima, H. Sekiya, and E. Alarcon, "Class e2 resonant non-radiative wireless power transfer link: A design-oriented joint circuit-system co-characterization approach," in *Multi-Conference on Systems, Signals Devices (SSD), 2014 11th International*, pp. 1–4, Feb 2014. (Cited on pages 11 and 161.)

[46] G. Lee, B. Waters, C. Shi, W. S. Park, and J. Smith, "Design considerations for asymmetric magnetically coupled resonators used in wireless power transfer applications," in *Biomedical Wireless Technologies, Networks, and Sensing Systems (BioWireleSS), 2013 IEEE Topical Conference on*, pp. 151–153, Jan 2013. (Cited on page 11.)

[47] N. Egidos, E. Bou-Balust, R. Sedwick, E. J. Alarcón Cot, *et al.*, "On frequency optimization of assymetric resonant inductive coupling wireless power transfer links," *Progress in Electromagnetic Research Symposium*, vol. 3, no. 12, p. 6, 2014. (Cited on pages 11 and 160.)

[48] M.-L. Kung and K.-H. Lin, "Enhanced analysis and design method of dual-band coil module for near-field wireless power transfer systems," *Microwave Theory and Techniques, IEEE Transactions on*, vol. 63, pp. 821–832, March 2015. (Cited on page 11.)

[49] Q. Yuan, Q. Chen, and K. Sawaya, "Effect of nearby human body on wpt system," in *Antennas and Propagation (EUCAP), Proceedings of the 5th European Conference on*, pp. 3983–3986, IEEE, 2011. (Cited on page 11.)

[50] X. L. Chen, A. E. Umenei, D. W. Baarman, N. Chavannes, V. De Santis, J. R. Mosig, and N. Kuster, "Human exposure to close-range resonant wireless power transfer systems as a function of design parameters," *Electromagnetic Compatibility, IEEE Transactions on*, vol. 56, no. 5, pp. 1027–1034, 2014. (Cited on page 11.)

[51] W.-s. Lee, H.-S. Jang, K.-S. Oh, and J.-W. Yu, "Close proximity effects of metallic environments on the antiparallel resonant coil for near-field powering," *Antennas and Propagation, IEEE Transactions on*, vol. 61, no. 6, pp. 3400–3403, 2013. (Cited on page 11.)

[52] E. Bou-Balust, R. Sedwick, P. Fisher, and E. Alarcon, "Maximizing efficiency through impedance matching from a circuit-centric model of non-radiative resonant wireless power transfer," in *Circuits and Systems (ISCAS), 2013 IEEE*

International Symposium on, pp. 2783–2786, 2013. (Cited on pages 11, 30 and 151.)

[53] X. Zhang, S. Ho, and W. Fu, "Quantitative design and analysis of relay resonators in wireless power transfer system," *Magnetics, IEEE Transactions on*, vol. 48, pp. 4026–4029, Nov 2012. (Cited on page 11.)

[54] D. Ahn and S. Hong, "Effect of coupling between multiple transmitters or multiple receivers on wireless power transfer," *Industrial Electronics, IEEE Transactions on*, vol. 60, pp. 2602–2613, July 2013. (Cited on pages 11 and 12.)

[55] E. Bou-Balust, E. Alarcon, D. Vidal, and R. Sedwick, "Em characterization of interfering objects in resonant inductive coupling wireless power transfer"," in *Progress in Electromagnetic Research Symposium*, pp. 1–4, August 2014. (Cited on page 11.)

[56] D. Ahn and S. Hong, "A study on magnetic field repeater in wireless power transfer," *Industrial Electronics, IEEE Transactions on*, vol. 60, pp. 360–371, Jan 2013. (Cited on pages 11 and 71.)

[57] C. Stevens, "Magnetoinductive waves and wireless power transfer," *Power Electronics, IEEE Transactions on*, vol. 30, pp. 6182–6190, Nov 2015. (Cited on page 11.)

[58] A. Kurs, R. Moffatt, and M. Soljačić, "Simultaneous mid-range power transfer to multiple devices," *Applied Physics Letters*, vol. 96, no. 4, p. 044102, 2010. (Cited on pages 12 and 14.)

[59] J. Casanova, Z. N. Low, and J. Lin, "A loosely coupled planar wireless power system for multiple receivers," *Industrial Electronics, IEEE Transactions on*, vol. 56, pp. 3060–3068, Aug 2009. (Cited on page 12.)

[60] B. Cannon, J. Hoburg, D. Stancil, and S. Goldstein, "Magnetic resonant coupling as a potential means for wireless power transfer to multiple small receivers," *Power Electronics, IEEE Transactions on*, vol. 24, pp. 1819–1825, July 2009. (Cited on page 12.)

[61] D. Ricketts and M. Chabalko, "On the efficient wireless power transfer in resonant multi-receiver systems," in *Circuits and Systems (ISCAS), 2013 IEEE International Symposium on*, pp. 2779–2782, May 2013. (Cited on page 12.)

[62] M. Fu, T. Zhang, C. Ma, and X. Zhu, "Efficiency and optimal loads analysis for multiple-receiver wireless power transfer systems," *Microwave Theory and Techniques, IEEE Transactions on*, vol. 63, pp. 801–812, March 2015. (Cited on page 12.)

[63] M. R. V. Moghadam and R. Zhang, "Multiuser charging control in wireless power transfer via magnetic resonant coupling," *IEEE International Conference on Acoustics, Speech, and Signal Processing (ICASSP)*, 2015. (Cited on page 12.)

[64] K. Lee and D.-H. Cho, "Analysis of wireless power transfer for adjustable power distribution among multiple receivers," *Antennas and Wireless Propagation Letters, IEEE*, vol. 14, pp. 950–953, 2015. (Cited on page 12.)

[65] A. Bodrov and S.-K. Sul, *Analysis of Wireless Power Transfer by Coupled Mode Theory (CMT) and Practical Considerations to Increase Power Transfer Efficiency, Wireless Power Transfer - Principles and Engineering Explorations*. InTech, 2012. (Cited on pages 13 and 18.)

[66] Q. Yuan, Q. Cheng, L. Li, and J. Sawaya, "Numerical analysis on transmission efficiency of evanescent resonant coupling wireless power transfer system," *IEEE Transactions on antennas and propagation*, vol. 58, May 2010. (Cited on pages 13 and 18.)

[67] Y.-H. Kim, S.-Y. Kang, S. Cheon, M.-L. Lee, and J.-M. Lee, "Optimization of wireless power transmission through resonant coupling," *IEEE International Symposium on Power Electronics, Electrical Drives, Automation and Motion*, 2010. (Cited on pages 13 and 18.)

[68] S. Cheon, Y. Kim, S. Kang, M. Lee, J. Lee, and T. Zyung, "Circuit-model-based analysis of a wireless energy-transfer system via coupled magnetic resonances," *IEEE Transactions on Industrial Electronics*, vol. 58, 2011. (Cited on pages 13 and 18.)

[69] T. C. Beh, T. Imura, M. Kato, and Y. Hori, "Basic study of improving efficiency of wireless power transfer via magnetic resonance coupling based on impedance matching," in *Industrial Electronics (ISIE), 2010 IEEE International Symposium on*, pp. 2011 –2016, july 2010. (Cited on pages 13 and 18.)

[70] Y. Kim, S. Kang, S. Cheon, M. Lee, J. Lee, and T. Zyung, "Optimization of wireless power transmission through resonant coupling," *International Symposium on Power Electronics, Electrical Drives, Automation and Motion*, 2010. (Cited on page 13.)

[71] M. Kiani and M. Ghovanloo, "A figure-of-merit for designing high-performance inductive power transmission links," *IEEE Transactions on Industrial Electronics*, 2013. (Cited on page 18.)

[72] M. Kiani, U.-M. Jow, and M. Ghovanloo, "Design and optimization of a 3-coil inductive link for efficient wireless power transmission," *Biomedical Circuits and Systems, IEEE Transactions on*, vol. 5, pp. 579 –591, dec. 2011. (Cited on page 19.)

[73] G. Grandi, M. K. Kazimierczuk, A. Massarini, and R. U., "Stray capacitances of single-layer solenoid air-core inductors," *IEEE Transactions On Industry Applications*, vol. 35, September 1999. (Cited on pages 25, 26 and 27.)

[74] E. Bou, E. Alarcon, and J. Gutierrez, "A comparison of analytical models for resonant inductive coupling wireless power transfer," *Session 2P4 Near to Mid-range Wireless Power Transfer Technology: Principles and Applications 2*, p. 389, 2012. (Cited on pages 27, 46, 113, 141 and 160.)

[75] E. Bou-Balust, R. Sedwick, P. Fisher, and E. Alarcon, "Multipath relaying effects in multiple-node resonant inductive coupling wireless power transfer," *Wireless Power Transfer*, pp. 1–10, 2016. (Cited on pages 31 and 161.)

[76] A. P. Sample, B. Waters, S. Wisdom, and J. Smith, "Enabling seamless wireless power delivery in dynamic environments," *Proceedings of the IEEE*, June 2013. (Cited on pages 32 and 34.)

[77] E. M. Thomas, J. D. Heebl, C. Pfeiffer, and A. Grbic, "A power link study of wireless non-radiative power transfer systems using resonant shielded loops," *Circuits and Systems I: Regular Papers, IEEE Transactions on*, vol. PP, no. 99, p. 1, 2012. (Cited on pages 39 and 40.)

[78] E. Bou-Balust, A. Hu, and E. Alarcon, "Scalability analysis of simo non-radiative resonant wireless power transfer systems based on circuit models," *Circuits and Systems I: Regular Papers, IEEE Transactions on*, vol. 62, pp. 2574–2583, Oct 2015. (Cited on pages 71, 104 and 160.)

[79] Z. Zhihua and M. Weiming, "Ac impedance of an isolated flat conductor," *IEEE Transactions on Electromagnetic Compatibility*, vol. 44, 2003. (Cited on page 72.)

[80] A. Wheeler, "Formulas for the skin effect," *Proceedings of the IRE*, 1948. (Cited on page 72.)

[81] A. Porter, D. Aliger, R. Sedwick, J. Merk, R. Opperman, A. Buck, G. Eslinger, P. Fisher, D. Miller, and E. Bou-Balust, "Dual-purpose resonate actuators for electromagnetic formation flight and wireless power transfer," *Proceedings of the AIAA SciTech*, 2014. (Cited on pages 94, 95, 96, 161 and 165.)

[82] P. Almers, E. Bonek, A. Burr, N. Czink, M. Debbah, V. Degli-Esposti, H. Hofstetter, P. Kyösti, D. Laurenson, G. Matz, *et al.*, "Survey of channel and radio propagation models for wireless mimo systems," *EURASIP Journal on Wireless Communications and Networking*, vol. 2007, no. 1, pp. 56–56, 2007. (Cited on page 102.)

[83] D. Alinger, A. Porter, and R. Sedwick, "Performance optimization of resonant inductive wireless power transfer using multi-layer flat spiral coils," *Annals of Physics*, 2013. (Cited on page 108.)

[84] G. Kendir, W. Lui, G. Wang, M. Sivaprakasam, R. Bashirullah, M. Humayun, and J. Weiland, "An optimal design methodology for inductive power link with class-e amplifier," *IEEE Transactions on Circuits and Systems*, vol. 52, 2005. (Cited on page 122.)

[85] C. Sullivan, "Optimal choice for number of strands in a litz-wire transformer winding," in *Power Electronics Specialists Conference, 1997. PESC '97 Record., 28th Annual IEEE*, vol. 1, pp. 28 –35 vol.1, jun 1997. (Cited on page 122.)

[86] R. Sredojovic and S. Vladimir, "Optimization-based framework for simultaneous circuit-and-system design-space exploration: A high-speed link example," *IEEE/ACM International Conference on Computer-Aided Design*, 2008. (Cited on page 125.)

[87] G. S. Smith, "Proximity effect in systems of parallel conductors," *Journal of Applied Physics*, vol. 43, pp. 2196 –2203, may 1972. (Cited on page 130.)

[88] P. Gupta and P. R. Kumar, "The capacity of wireless networks," *IEEE Transactions on Information Theory*, 2000. (Cited on page 138.)

[89] O. Kremien, "Scalability in distributed systems, parallel systems and supercomputers," *Lecture Notes in Computer Science*, 1995. (Cited on page 138.)

[90] J. Zhou, R. Hu, and Y. Qian, "Scalable distributed communication architectures to support advanced metering infrastructure in smart grid," *Parallel and Distributed Systems, IEEE Transactions on*, vol. 23, pp. 1632–1642, Sept 2012. (Cited on page 138.)

[91] D. Estrin, R. Govindan, J. Heidemann, and S. Kumar, "Next century challenges: Scalable coordination in sensor networks," *Proceedings of the 5th annual ACM/IEEE international conference on Mobile computing and networking*, 2000. (Cited on page 138.)

[92] L. Duboc, D. Rosenblum, and T. Wicks, "A framework for characterization and analysis of software system scalability," *Proceedings of the 6th joint meeting of the European software engineering conference and the ACM SIGSOFT*, 2007. (Cited on page 138.)

[93] T. Nagashima, K. Inoue, X. Wei, E. Bou, E. Alarcon, and H. Sekiya, "Inductively coupled wireless power transfer with class-e 2 dc-dc converter," in *Circuit Theory and Design (ECCTD), 2013 European Conference on*, pp. 1–4, IEEE, 2013. (Cited on page 160.)

[94] E. Bou, E. Alarcon, R. Sedwick, and P. Fisher, "Interference analysis on resonant inductive coupled wireless power transfer links," in *Circuits and Systems (ISCAS), 2013 IEEE International Symposium on*, pp. 2783–2786, IEEE, 2013. (Cited on pages 160 and 161.)

[95] T. Nagashima, X. Wei, E. Bou, E. Alarcón, M. K. Kazimierczuk, and H. Sekiya, "Analysis and design of loosely inductive coupled wireless power transfer system based on class-e^2 dc-dc converter for efficiency enhancement," *IEEE Transactions on Circuits and Systems I: Regular Papers*, vol. 62, no. 11, pp. 2781–2791, 2015. (Cited on page 160.)

[96] T. Nagashima, X. Wei, E. Bou, E. Alarcón, and H. Sekiya, "Analytical design for resonant inductive coupling wireless power transfer system with class-e inverter and class-de rectifier," in *Circuits and Systems (ISCAS), 2015 IEEE International Symposium on*, pp. 686–689, IEEE, 2015. (Cited on page 160.)

[97] R. Jove-Casulleras, J. Ramos, H. Ccorimanya, A. Camps, E. Alarcon, A. Amezaga, and E. Bou, "Temperature gradient sensor from pulsed power supply duty cycle in ultra-low-power energy harvesting system," *Electronics Letters*, vol. 50, no. 11, pp. 826–828, 2014. (Cited on page 160.)

[98] T. Nagashima, X. Wei, E. Bou, E. Alarcon, M. K. Kazimierczuk, and H. Sekiya, "Steady-state analysis of isolated class-e2 converter outside nominal operation," *IEEE Transactions on Industrial Electronics*, 2016. (Cited on page 161.)

[99] M. Saad, N. Egidos, E. Bou-Balust, and E. Alarcón, "On tunable switch-mode reactive networks: A gyrator-based resonator emulation," in *Circuits and Systems (ISCAS), 2016 IEEE International Symposium on*, pp. 642–645, IEEE, 2016. (Cited on page 161.)

[100] E. Bou, R. Sedwick, and E. Alarcon, "Relay effects in multiple-node resonant inductive coupling wireless power transfer systems," in *Circuits and Systems (ISCAS), 2015 IEEE International Symposium on*, pp. 690–693, IEEE, 2015. (Cited on page 161.)

[101] E. Bou-Balust, A. El Aroudi, P. Fisher, and E. Alarcon, "Unveiling nonlinear dynamics in resonant inductively coupled wireless power transfer," in *Circuits and Systems (ISCAS), 2014 IEEE International Symposium on*, pp. 2612–2615, IEEE, 2014. (Cited on page 161.)

Wireless Power Transfer: Fueling the Dots

Abstract: Resonant Inductive Coupling Wireless Power Transfer (RIC-WPT) has been proven to provide very high power transfer efficiencies (above 80%) for moderate distances, and is hence foreseen as a key technology to enable wireless power transfer to a myriad of different devices and related applications. Due to the multidisciplinary nature of the WPT underlying principles, several approaches have been provided to analyze RIC-WPT systems from different perspectives (encompassing Electromagnetic fields, Circuit models and Optics), but they have failed to provide a unified model to understand and ultimately to design the behaviour of such systems. This thesis is therefore aimed to, first, provide a multi-modal RIC-WPT complete model oriented to the design and in turn optimisation of RIC-WPT systems and, secondly, to explore and characterize the fundamental challenges precluding the widespread deployment of RIC-WPT and thereby accordingly to yield a set of design guidelines to overcome them. Finally, and due to the fact that multi-node RIC-WPT systems are key to the adoption of this technology, this thesis models, characterizes and analyzes Multiple-Input Multiple-Output RIC WPT Systems, making special emphasis on their scalability.

Keywords: Wireless Power Transfer, Resonant Inductive Coupling, Electromagnetic Fields